Friedrich-Alexander-Universität
Naturwissenschaftliche Fakultät

Master's Thesis
in Physics

Characterization of a Grating-Based Dark-Field CT System

Luca Julius Fritsch

Supervisor: Prof. Dr. Stefan Funk

Erlangen Centre for Astroparticle Physics

Submission date: 23 April 2025

Contents

1 Motivation

Breast cancer remains the most common cancer in women worldwide, and early detection is essential to improving survival rates [Wor24]. One promising indicator for early-stage breast cancer are microcalcifications, especially in ductal carcinoma in situ. Conventional attenuation-based X-ray imaging often fails to detect small or weakly attenuating calcifications. To address these limitations, grating-based X-ray imaging can be employed to extract dark-field contrast. In particular, the dark-field signal is sensitive to small-angle X-ray scattering caused by microscopic structures below imaging resolution, such as microcalcifications.

Previous work at the Erlangen Centre for Astroparticle Physics (ECAP) has demonstrated the potential of dark-field imaging for breast diagnostics [Ant+13; Mic+13]. Anton et al. showed that the dark-field signal, which originates from micrometer-sized calcium phosphate grains, enables improved visualization of tumor regions and can be quantitatively linked to the underlying microstructure. More recently, Rauch et al. analyzed over 300 microcalcifications and showed that combining dark-field parameters with attenuation data improves lesion classification. Emons et al. demonstrated in a preclinical study that additional malignant lesions, some not even visible on mammography, can be detected using X-ray dark-field imaging [Rau+20; Emo+20].

The clinical relevance of such findings is emphasized by studies showing a prognostic role of calcifications beyond detection, particularly in association with HER2 expression and recurrence risk [OM18], underlining the need for imaging methods that go beyond mere visibility and provide microstructural information.

This thesis contributes to the advancement of grating-based dark-field computed tomography (DFCT) by experimentally characterizing a photon-counting detector and integrating it into a complete CT system. The setup was evaluated through measurements with and without gratings, including signal extraction, reconstruction, and three-dimensional visualization. Various samples were used to assess contrast sensitivity and imaging performance.

Although clinical use in screening is currently limited by system size, scan time, and dose, intraoperative application appears more feasible. DFCT could support margin assessment during tumor resection, helping to confirm complete removal and reduce the need for repeat surgery. By establishing a functional DFCT pipeline and demonstrating its feasibility on relevant samples, this work provides a basis for future investigations in medical imaging.

2 Theoretical Background

This chapter provides the theoretical background for the imaging methods applied in this work. It begins with a description of the fundamental properties of X-rays and their interactions with matter. Building upon this, the principles of grating-based X-ray imaging are presented, including the physical origin and interpretation of attenuation, phase-contrast, and dark-field signals. The chapter concludes with an overview of computed tomography (CT), focusing on data acquisition, image reconstruction techniques, and relevant artifacts.

2.1 Fundamentals of X-rays

X-rays are high-energy electromagnetic waves characterized by their short wavelengths and high photon energies. Their interaction with matter is governed by energy-dependent processes such as photoelectric absorption, Compton scattering, and elastic scattering. A comprehensive understanding of these fundamental properties is essential for interpreting signal formation in both attenuation-based and grating-based X-ray imaging, as applied in this work.

2.1.1 X-ray Generation and Properties

In X-ray tubes, photons are produced through high-energetic electron interactions with a metallic anode. Electrons are emitted from a heated cathode and accelerated by a high voltage U_B toward the anode, which is typically composed of tungsten. Upon deceleration in the Coulomb field of atomic nuclei and interaction with electron shells, two types of radiation are generated:

- **Bremsstrahlung**, forming a *continuous spectrum*, caused by the deflection and deceleration of electrons in the nuclear field.
- **Characteristic radiation**, consisting of *discrete emission lines* that result from electronic transitions between inner atomic shells following ionization.

Typical acceleration voltages U_B used in medical X-ray tubes range from 30 kV to 150 kV [SKJ18], setting the upper limit for the kinetic energy of the electrons and

thus for the maximum photon energy according to

$$E_{\max} = e \cdot U_{\mathrm{B}} \,, \tag{2.1}$$

where e denotes the elementary charge of the electron. The relation between photon energy and wavelength is given by Planck's law,

$$E_{\mathrm{Ph}} = h \cdot f = h \cdot \frac{c}{\lambda} \,, \tag{2.2}$$

with h being Planck's constant and c the speed of light in vacuum. For photon energies between 30 keV and 150 keV, the corresponding wavelengths λ range from approximately 41 pm down to 8 pm.

Bremsstrahlung. Only about 1 to 2 % of the electrons pass sufficiently close to the atomic nucleus to be significantly decelerated in its Coulomb field, thereby contributing to the generation of bremsstrahlung [Kri12]. The closer an electron approaches the nucleus, the greater the energy transfer to the emitted photon. The corresponding photon energy results from the energy difference between the incoming and outgoing electron,

$$E_{\mathrm{Ph}} = E_e - E'_e \,. \tag{2.3}$$

The remaining 98 to 99 % of the electron energy is converted into heat, causing the anode to heat up [SKJ18].
The bremsstrahlung spectrum theoretically follows a continuous distribution, decreasing linearly in intensity with increasing photon energy. In practice, low-energy photons are additionally attenuated within the anode material itself due to self-filtering [SKJ18]. While the maximum photon energy is determined by the acceleration voltage, the overall spectral intensity scales proportionally with the heating current of the filament I_{h}.

Characteristic radiation. In addition to bremsstrahlung, characteristic radiation arises when an incoming electron ionizes the anode material by ejecting an electron from an inner atomic shell. The resulting vacancy is subsequently filled by an electron from a higher shell, and the energy difference between the two levels is released in the form of a photon. These photon energies E_{Ph} are discrete and element-specific, depending solely on the energy difference between the involved atomic shells and not on the tube voltage U_{B}.
Although the relative contribution of characteristic radiation increases with higher acceleration voltage, it remains around 10 % for a tungsten anode at 250 keV [Dem16]. The emitted spectral lines are labeled according to the shell in which the vacancy occurred (e.g., K or L) and the transition path (e.g., α, β).
A schematic X-ray spectrum combining both bremsstrahlung and characteristic radiation for a tungsten anode is shown in Figure 2.1.

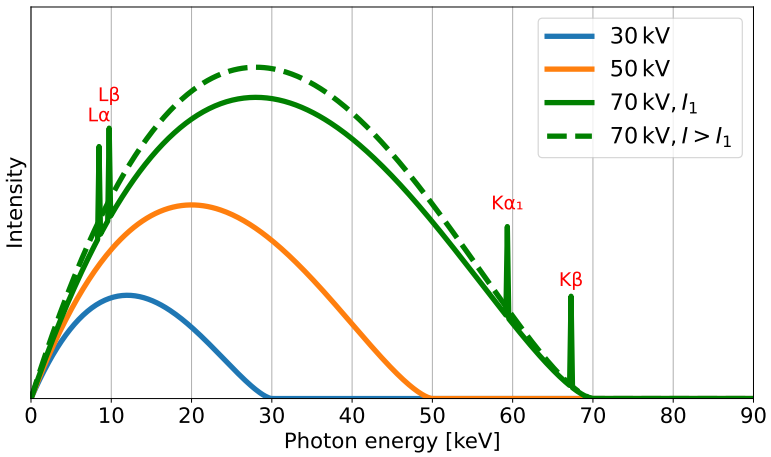

Figure 2.1: Schematic X-ray energy spectrum of a tungsten anode. The continuous bremsstrahlung component depends on the acceleration voltage U_B and the filament current I_h. Superimposed on the solid-green line are discrete characteristic radiation peaks, which are independent of U_B and result from electronic transitions between inner atomic shells. Plot inspired by [SKJ18].

2.1.2 Interaction of X-rays with Matter

The following physical descriptions of X-ray interaction mechanisms are based on standard literature, particularly the works of Demtröder [Dem16], Schlegel et al. [SKJ18], and Krieger [Kri12].
When X-rays propagate through matter, they interact with atoms in different ways depending on the photon energy and the atomic composition of the material. These interactions determine how much of the incident X-ray beam is transmitted, scattered, or absorbed. The total attenuation of an X-ray beam passing through a material of thickness z can be described by an exponential attenuation law, the Beer–Lambert law:

$$I(z) = I_0 \exp\big(-\mu(\lambda) \cdot z\big)\,, \tag{2.4}$$

where I_0 is the initial intensity, $I(z)$ the transmitted intensity, and $\mu(\lambda)$ the wavelength-dependent linear attenuation coefficient. This coefficient summarizes the contributions of all interaction processes at the given photon energy, including photoelectric absorption, Compton scattering, Rayleigh scattering, and pair production. In addition to the linear attenuation coefficient $\mu(\lambda)$, the mass attenuation coefficient μ_m (or: μ/ρ) is often used, which normalizes the attenuation to the material density ρ.

The relative importance of these processes strongly depends on the photon energy and the atomic number Z of the material. While photoelectric absorption dominates at low photon energies and for high-Z materials, Compton scattering becomes increasingly relevant at higher energies. Elastic Rayleigh scattering, although generally weak, plays a role at low energies and in low-Z materials. At even higher photon energies above 1.022 MeV electron–positron pair production may occur, but is not relevant in the energy range considered in this work [Dem16].
Figure 2.2 illustrates the energy dependence of the mass attenuation coefficient and its components for the example of water. It highlights the dominance regions of the different interaction processes over the relevant photon energy range, highlighting 50 keV, being in the range of the voltages used, and 511 keV, the rest energy of an electron. The following subsections describe the relevant interaction mechanisms in detail, highlighting their physical principles, dependencies, and relevance for X-ray imaging.

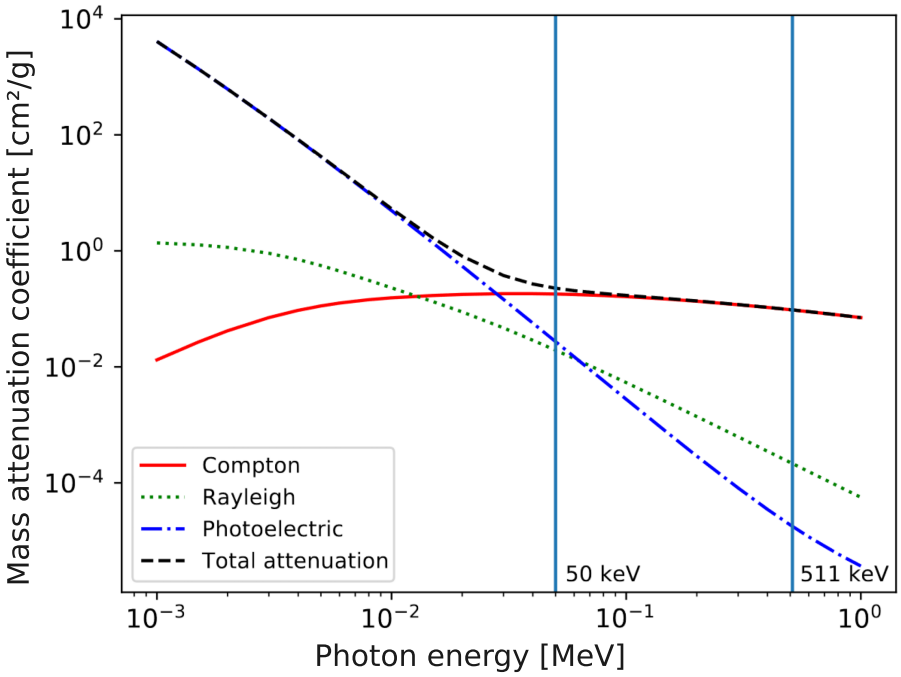

Figure 2.2: Mass attenuation coefficient and its components for photons in water as a function of photon energy. The contributions of photoelectric absorption, Compton scattering, and Rayleigh scattering are shown separately. The vertical blue lines indicate photon energies of 50 keV and 511 keV. Image adapted from: [BS22].

Total Linear Attenuation Coefficient

The total linear attenuation coefficient μ describes the overall reduction in the intensity of a photon beam as it propagates through a material, as expressed by the Beer–Lambert law in Equation 2.4. It accounts for all interaction processes that contribute to the attenuation of the primary beam, either through absorption or scattering. The following definitions are from [Eva55].
The total absorption coefficient μ_a is given by the sum of the attenuation coefficients for Compton absorption σ_a, photoelectric absorption τ, and pair production κ. When the Compton scattering coefficient σ_s is added to μ_a, the total attenuation coefficient μ is obtained:

$$\mu = \mu_a + \sigma_s = \tau + \sigma_a + \kappa + \sigma_s \,. \tag{2.5}$$

This coefficient quantifies the decrease in primary photon flux resulting from absorption and scattering events. In some elaborations, the Rayleigh scattering cross-section σ_R is not generally included in the total attenuation coefficient μ, as Rayleigh scattering is elastic, does not result in net energy loss, and is restricted to small angles.

Photoelectric Effect. When a photon with sufficient energy interacts with an electron in an inner shell of the target, the electron can be ejected from the atom. For this to happen, the photon energy must be at least equal to the binding energy of the electron E_B. Any energy exceeding the binding energy is transferred to the electron as kinetic energy $E_{e,\mathrm{kin}}$:

$$E_{e,\mathrm{kin}} = E_\mathrm{Ph} - E_\mathrm{B} = h \cdot f - E_\mathrm{B} \overset{!}{\geq} 0 \,. \tag{2.6}$$

The photoelectric effect preferably affects electrons from the K- or L-shell, especially when the photon energy equals or is only slightly above the binding energy. It is particularly relevant at low photon energies and in materials with a high atomic number Z. Therefore, its attenuation coefficient τ decreases strongly with E_Ph^{-3} and increases with approximately Z^3 to Z^5. [Kri12]
This strong dependence on atomic number allows for a good differentiation between bone-like material ($Z_\mathrm{Ca} = 20$) and the surrounding soft tissue ($Z \approx 7$) in X-ray imaging [SKJ18].

Rayleigh Scattering In Rayleigh scattering, the X-ray photon is scattered by the bound electrons of an atom without losing any energy. Therefore the photon only changes its direction but keeps the same energy - it is a so called elastic scattering process. The probability of Rayleigh scattering decreases as photon

energy increases, with its attenuation coefficient σ_R roughly following E^{-2} for photon energies above 10 keV [Kri12]. Since it also scales approximately with Z^2 to Z^3, Rayleigh scattering is more pronounced in high-Z materials like bone but much weaker in soft tissues and water.
Due to its minimal contribution to total attenuation outside of clinical X-ray imaging, Rayleigh scattering is often neglected in standard models. However, it is a form of coherent scattering, which also serves as the foundation for small-angle scattering (SAS) - a technique used in dark-field imaging, which will be discussed in a later chapter. At lower photon energies, the average scattering angle increases, potentially redirecting photons and contributing to image noise, which can reduce contrast.

Compton Scattering The Compton effect describes the inelastic scattering of an X-ray photon by a loosely bound or free electron. When the photon collides with the electron, part of its energy is transferred to the electron, causing it to be ejected from the atom. As a result, the scattered photon has a lower energy and a longer wavelength than before the interaction.

$$E'_\gamma = \frac{E_\gamma}{1 + \frac{E_\gamma}{m_e c^2}(1 - \cos\theta)} \tag{2.7}$$

describes the energy of the outgoing photon E'_γ as a function of the incoming photon energy E_γ and its scattering angle θ.
The Compton shift $\Delta\lambda$ describes the increase in photon wavelength due to scattering and depends solely on the scattering angle, not on the energy of the incoming photon [SKJ18]. The magnitude of this shift is determined by the Compton wavelength $\Delta\lambda_C$, which is associated with the rest energy of the electron. As a result, for a given scattering angle, the relative energy transfer to the electron increases with the photon's initial energy.
Considering the scattering angle θ, at small angles, the energy loss of the photon is minimal, whereas at larger angles (up to complete backward scattering: $\theta = 180°$) the photon loses significantly more energy. There is no exact mathematical or physical description of the dependence between the attenuation coefficient of the Compton effect, σ_C, and the photon energy E_γ [Kri12].
In the context of Compton interactions, the total linear attenuation coefficient for the Compton process, σ, can be decomposed into two distinct components: $\sigma = \sigma_a + \sigma_s$, where σ_a represents the Compton absorption coefficient, describing the fraction of the primary photon energy deposited in the medium through secondary electrons, while σ_s is the Compton scattering coefficient, which quantifies the removal of photons from the primary beam due to scattering events [Eva55]. Both components contribute to the total attenuation coefficient μ, as they describe different mechanisms reducing the intensity of the primary photon beam.

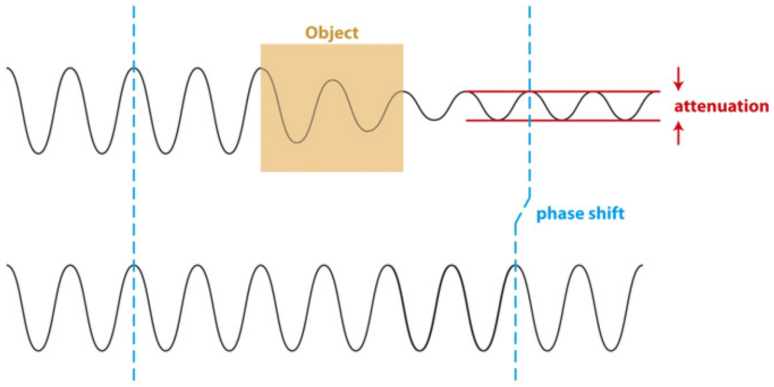

Figure 2.3: Illustration of the effect of a complex refractive index $n = 1 - \delta + i\beta$ on an X-ray wave. Absorption leads to attenuation (red), while refraction causes a phase shift (blue). The lower wave shows the unmodified reference. Image source: [Auw+14].

2.1.3 Complex Refractive Index of X-Rays

To further describe how X-rays interact with matter on a microscopic level, it is useful to introduce the complex refractive index. This quantity encapsulates both the phase shift and the attenuation experienced by X-rays as they propagate through a medium. It also provides a basis for deriving the exponential attenuation law (Equation 2.4) introduced in the previous section and forms the foundation for phase-sensitive imaging techniques discussed later in this work.

The propagation of X-rays through a medium is governed by the wave equation, which, in a dielectric material with refractive index n, takes the form:

$$\left(\frac{n^2}{c^2}\frac{\partial^2}{\partial t^2} - \nabla^2\right)\Psi = 0. \tag{2.8}$$

For X-rays, the refractive index n deviates only slightly from unity and is conventionally expressed as

$$n = 1 - \delta + i\beta. \tag{2.9}$$

Here, δ and β are small, energy- and material-dependent quantities related to the wave–matter interaction.

In the following, we will examine the physical meaning of these parameters and show how they relate to attenuation and phase effects, respectively. Their connection to the attenuation coefficient and their dependence on photon energy and material composition will also be discussed.

Wave Propagation in Matter

To solve the wave equation (Equation 2.14), we assume a plane wave solution in a medium with complex refractive index n. This approach allows us to examine how amplitude and phase are affected as the wave propagates through matter. Assuming a monochromatic wave with angular frequency ω, the plane wave ansatz at timespace position $(t, \vec{r})$ is given by:

$$\Psi(\vec{r}, t) = \Psi_0 \cdot e^{i(\vec{k}\cdot\vec{r}-\omega t)} \,. \tag{2.10}$$

The wave vector $\vec{k}$ is then modified according to:

$$\vec{k} = \vec{k_0} n = \vec{k_0}(1 - \delta + i\beta), \tag{2.11}$$

where $k_0 = |\vec{k_0}| = {}^{2\pi}/_{\lambda_0}$ is the vacuum wave number, and λ_0 the vacuum wavelength. Assuming wave propagation only in the z-direction, the wave vector simplifies to $\vec{k} = k_z \hat{\mathbf{z}}$, where the z-component is given by $k_z = k_0 n$. Therefore:

$$\vec{k} \cdot \vec{r} = k_0 n \, z = k_0 z(1 - \delta + i\beta) \,. \tag{2.12}$$

This leads to a modified wave equation:

$$\begin{aligned} \Psi(z, t) &= \Psi_0 \cdot \exp\left(i k_0 z(1 - \delta + i\beta) - i\omega t\right) && (2.13)\\ &= \underbrace{\Psi_0 \cdot \exp(i k_0 z - i\omega t)}_{\text{vacuum propagation}} \cdot \underbrace{\exp(-i\delta k_0 z)}_{\text{phase shift}} \cdot \underbrace{\exp(-\beta k_0 z)}_{\text{attenuation}} \,. && (2.14) \end{aligned}$$

From this expression, it is evident that δ causes a phase shift in the wave, while β leads to an exponential decay of intensity as the wave propagates through the medium. This effect is also illustrated schematically in Figure 2.3, where both the phase shift and the attenuation due to a complex refractive index are visualized.

Attenuation Term and Link to Attenuation Coefficient. The Beer–Lambert law with the linear attenuation coefficient μ can be derived from a wave-optical perspective. In this view, attenuation arises from the imaginary part β of the complex refractive index, which quantifies the material's effect on the amplitude of the propagating wave.
For an X-ray wave propagating through a homogeneous medium, the intensity $I(z)$ corresponds to the squared modulus of the wave function $\Psi(z, t)$, as shown in Equation 2.14:

$$I(z) = |\Psi(z, t)|^2 = \Psi_0^2 \cdot \exp(-2\beta k_0 z) \,. \tag{2.15}$$

Comparison with the Beer–Lambert law (Equation 2.4) yields the relationship:

$$\mu = 2\beta k_0 \,. \tag{2.16}$$

This expression links the microscopic wave-based quantity β to the macroscopic attenuation coefficient μ, which is commonly used in radiography and computed tomography.

Phase Shift Term. When propagating through a medium with the complex refractive index n and thickness d, the wave acquires a constant phase shift $\Delta\varphi$. Considering the wave equation (2.14) in the absence of attenuation,

$$\Psi_m(z,t) = \Psi_0 \cdot \exp\left[i(k_0 z - \delta k_0 d - \omega t)\right], \tag{2.17}$$

the resulting phase shift is given by

$$\Delta\varphi = -\delta k_0 d \; < 0 \,. \tag{2.18}$$

Due to its negative sign, the phase shift effectively advances the wavefront in the direction of propagation. Its magnitude depends on the refractive decrement δ and the thickness d of the medium. In inhomogeneous materials, spatial variations in δ can lead to locally varying phase shifts and wavefront inclinations, often illustrated using wedge-shaped media [Rut13; Sch20b].

Energy and Material Dependence of β and δ

The refractive index decrements δ and β exhibit a strong dependence on both photon energy and material composition. While δ typically scales with $1/E^2$, β follows a similar decreasing trend, reflecting the dominant absorption processes. These dependencies are particularly relevant for phase- and absorption-based contrast in X-ray imaging [Gur+09; Rut13].
Figure 2.4 illustrates the behavior of δ and β for water, fat, and cortical bone in the energy range from 10 keV to 30 keV, based on tabulated values by Henke et al. [HGD93], made available through the CXRO database.

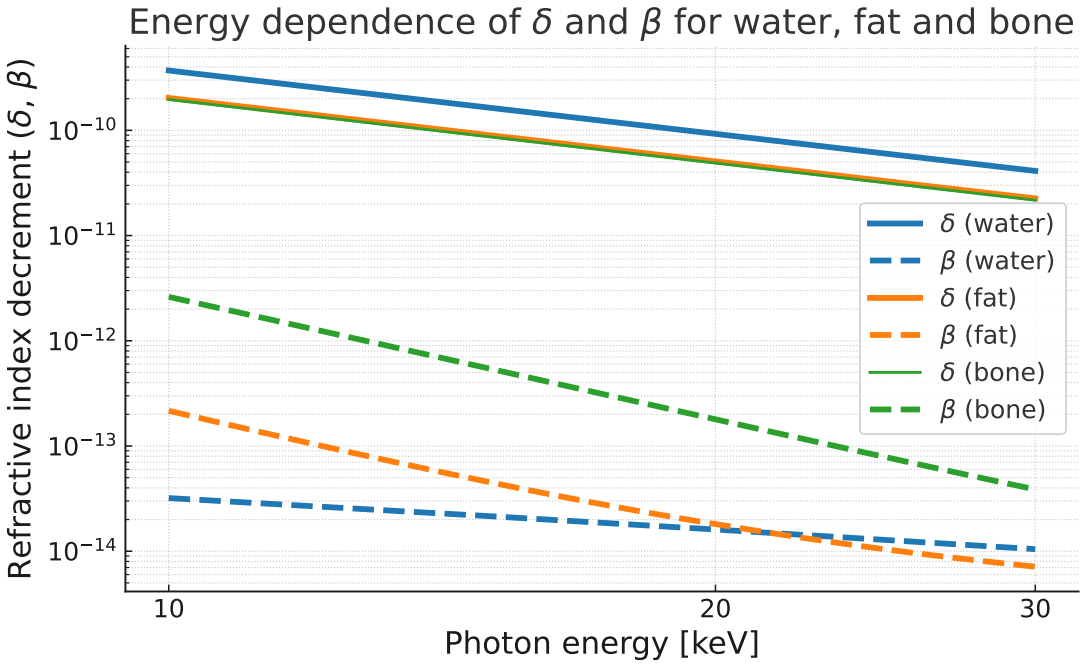

Figure 2.4: Refractive index decrements δ and β for water, fat, and cortical bone as a function of photon energy. Solid lines represent δ, dashed lines represent β. The data were computed using tabulated atomic scattering factors from Henke et al. [HGD93].
The following chemical compositions were used: H_2O for water, $C_{55}H_{74}O_6$ for fat, approximating a triglyceride with three saturated fatty acid chains, and $H_{14} \cdot 45\, C_6 \cdot 74\, N_1 \cdot 21\, O_4 \cdot 27\, Mg_0 \cdot 2\, P_1 \cdot 17\, S_0 \cdot 04\, Ca_1 \cdot 7$ for cortical bone, based on the elemental composition proposed by Woodard and White [WW86].

2.2 Grating-Based X-ray Imaging

Grating-based X-ray imaging extends conventional attenuation-based methods by exploiting the wave nature of X-rays. Through the use of a Talbot-Lau interferometer, it enables simultaneous acquisition of attenuation, differential phase-contrast, and dark-field signals from the same projection. These complementary contrast mechanisms provide additional diagnostic value, particularly in soft tissues or samples with fine microstructure.
This section introduces the working principle of grating interferometry, the phase-stepping method, and the formation of the respective image signals, with a particular emphasis on the dark-field modality, which forms the core of this work.

2.2.1 Grating-Based Talbot-Lau Interferometer

Grating-based interferometry enables phase-sensitive X-ray imaging with conventional, incoherent X-ray sources. This is achieved using a Talbot-Lau interferometer, which consists of three gratings: a source grating (G0), a phase grating (G1), and an analyzer grating (G2). Together, they form an interference pattern that is sensitive to both phase shifts and small-angle scattering in the sample.
The following subsections describe the underlying physical principles and the specific roles of each grating, with particular attention to their relevance for dark-field signal formation.

Talbot Effect and the Phase Grating

The Talbot effect describes the self-imaging of a periodic phase structure under coherent illumination [Tal36]. When a plane wave passes through a phase grating such as G1, it generates periodic intensity patterns at discrete propagation distances, known as Talbot distances z_T, due to near-field diffraction and interference. The first (full) Talbot distance is given by [Ray81]:

$$d_{T1} = \frac{2p^2}{\lambda}, \quad \lambda \ll p\,. \tag{2.19}$$

Here, d_{T1} is the Talbot distance, p is the grating period, and λ is the X-ray wavelength. The approximation $\lambda \ll p$ ensures that the formula holds in the small-angle (paraxial) approximation.
In practical imaging systems, G1 is a phase grating that imposes a spatially periodic phase shift onto the incoming wavefront without attenuating it. The phase shift depends on the grating height and the photon energy, and is typically optimized for a design energy E. Common designs include π- and $\pi/2$-shifting gratings.

The grating's duty cycle $D_c = w/p$, defined as the ratio of gap width w to period p, is typically set to 0.5 to maximize fringe contrast.
High-contrast interference fringes suitable for image signal extraction only form at specific fractional Talbot distances d_{fT}, which depend on the grating design. At full Talbot distances d_T, the self-image of the phase grating is laterally uniform and does not produce a measurable modulation in intensity. For a π-shifting grating, usable self-images appear at distances [YWL15]:

$$d_{fT} = \frac{2m-1}{16} \cdot d_{T1}\,, \quad m \in \mathbb{N}\,. \tag{2.20}$$

This configuration leads to a spatial frequency doubling of the fringe pattern and allows higher fringe resolution downstream. A simulated Talbot carpet illustrating this effect is shown in Figure 2.5.
To capture this fine interference pattern, the analyzer grating G2 is positioned exactly at such a fractional Talbot distance d_{fT} downstream of G1. G2 is an absorption grating that acts as a sampling mask and enables the indirect detection of the periodic intensity modulation. Its period p_2 is matched to the fringe period p_T at the chosen Talbot plane, allowing the fringe contrast to be measured via the phase-stepping procedure explained in the next subsection. Refraction within the sample leads to a lateral shift of the fringes, while small-angle scattering causes a local reduction in fringe visibility.
In real systems, several effects such as the finite source size and poly-chromaticity of the X-ray beam degrade fringe visibility. The resulting fringe pattern is a superposition of multiple overlapping Talbot carpets for different wavelengths, as illustrated in [Lud20]. Therefore, the exact placement of G2 is chosen to maximize fringe visibility.

Lau Effect and the Source Grating

Conventional X-ray tubes produce spatially incoherent radiation. To enable interference under such conditions, the so-called Lau effect is exploited [Lau48]: a source grating G0 subdivides the broad beam into an array of narrow, mutually coherent beamlets. Each of these beamlets can form its own Talbot pattern downstream. Without G0, the patterns from the extended source would superimpose incoherently, and the interference signal would vanish.
Constructive superposition requires the geometric condition [Pfe+06]:

$$\frac{p_0}{p_T} = \frac{d_{01}}{d_T}\,, \tag{2.21}$$

where p_0 is the period of G0, p_T the fringe period, d_{01} the G0–G1 distance, and d_T the Talbot distance. This ensures that the overlapping contributions of the many point-like sources align constructively.

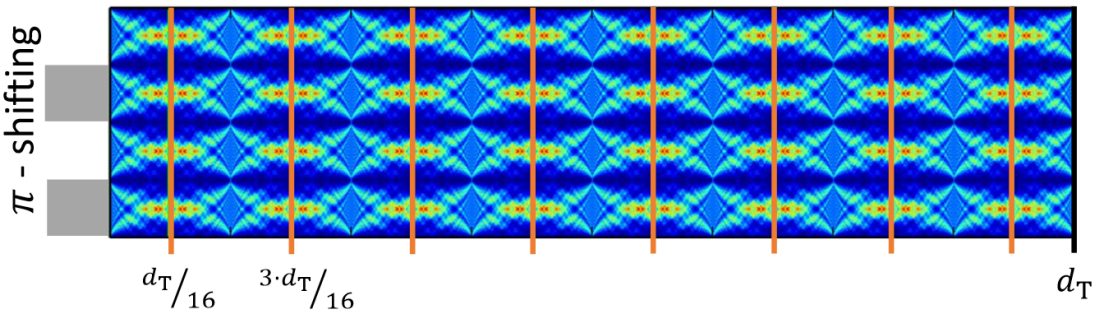

Figure 2.5: Simulated Talbot carpet for a π-shifting phase grating under monochromatic plane wave illumination. The image shows the intensity distribution along the propagation direction. At specific fractional Talbot distances, marked by orange lines, high-contrast lateral fringe patterns appear due to near-field interference. The frequency doubling effect, characteristic of π-shifting gratings, is also visible. Image adapted from [Sch20b; Wol16].

Moiré Pattern and Analyzer Grating

Since the Talbot fringes typically have sub-micron periods, their fine structure cannot be resolved by standard X-ray detectors. To overcome this limitation, a Moiré pattern with a significantly larger spatial period is generated by introducing a slight mismatch between the fringe pattern and the analyzer grating G2, which is placed at a fractional Talbot distance.
Mathematically, the Moiré period p_M can be approximated by [Ami09]:

$$p_M = \frac{p_2 \cdot p_T}{\sqrt{p_2^2 + p_T^2 - 2p_2 p_T \cos\alpha}}, \tag{2.22}$$

where p_2 is the period of G2, p_T the fringe period, and α the relative tilt angle. Moiré fringes typically have periods in the hundreds of microns and are thus easily detectable.
Rather than being a side effect, the Moiré pattern is deliberately introduced to enhance visibility. Slight tilts or mismatches are used to generate a symmetric, high-contrast pattern that carries both phase and scattering information. The visibility V, defined as [Pag06]

$$V = \frac{I_{\max} - I_{\min}}{I_{\max} + I_{\min}}, \tag{2.23}$$

quantifies the local fringe contrast and reflects the system's alignment and sensitivity. Figure 2.7 summarizes the full interferometer geometry.

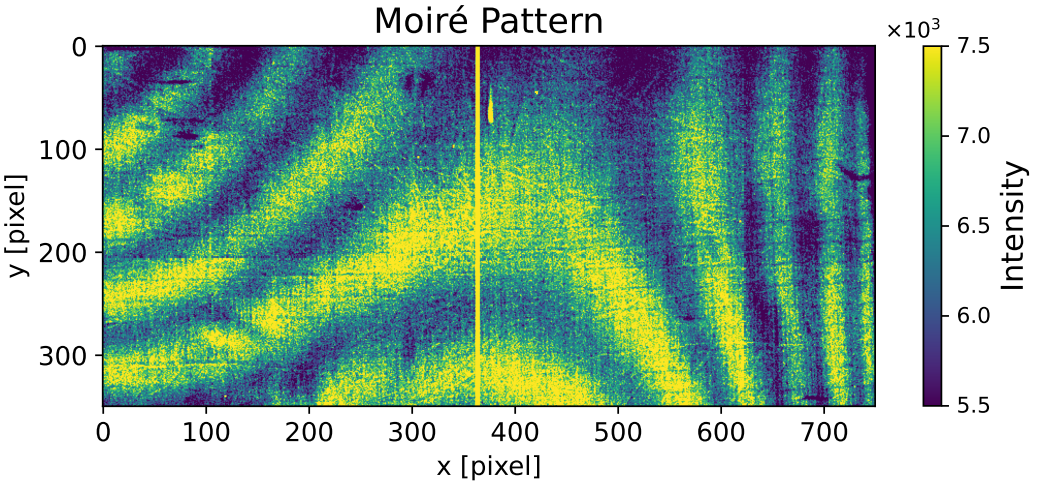

Figure 2.6: Example of a Moiré pattern used in this work. The gradual variation in fringe period is due to beam divergence; a dead detector column appears as a vertical line.

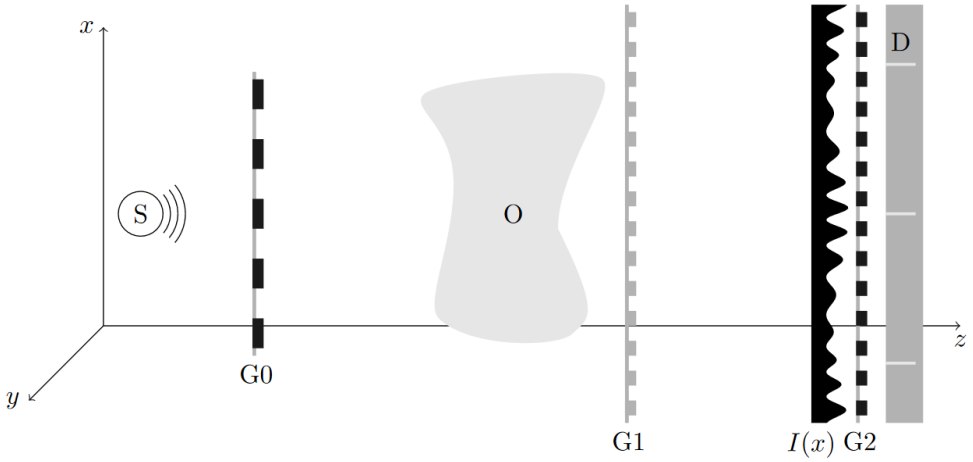

Figure 2.7: Schematic of a grating-based X-ray Talbot-Lau interferometer with source (S), gratings G0–G2, sample (O), and detector (D). Image adapted from [Rit+14].

2.2.2 Phase-Stepping Technique

To extract image information from the Talbot pattern, the G0 or G2 is moved step by step over at least one grating period $p_{0/2}$. This method is called *phase-stepping*, first described by [Wei+05]. For each step, an image is taken. The grating is shifted in small, equal intervals, and for every pixel, the intensity is recorded as a function of the grating position. In this work, the source grating G0 was moved, which is mathematically equivalent to stepping G2, as only the relative phase between the interference pattern and the analyzer grating is relevant.
If the setup were ideal, with a perfect rectangular grating and a monochromatic point source, the intensity curve would look like a triangle. However, in reality, the X-ray source is extended and emits different wavelengths. This causes the Talbot pattern to blur, and the intensity curve becomes more like a sine wave, compare Figure 2.8. It can be parametrized by the following sine function:

$$I(x) = \bar{I} + A \cdot \sin(2\pi x + \Phi)\,, \tag{2.24}$$

with x denoting the relative grating position in units of p_0, $\bar{I}$ the mean intensity, A the amplitude, and Φ the phase.
By comparing the object scan with a reference scan without the object (often referred to as a flat-field image), the following three signal modalities can be derived.

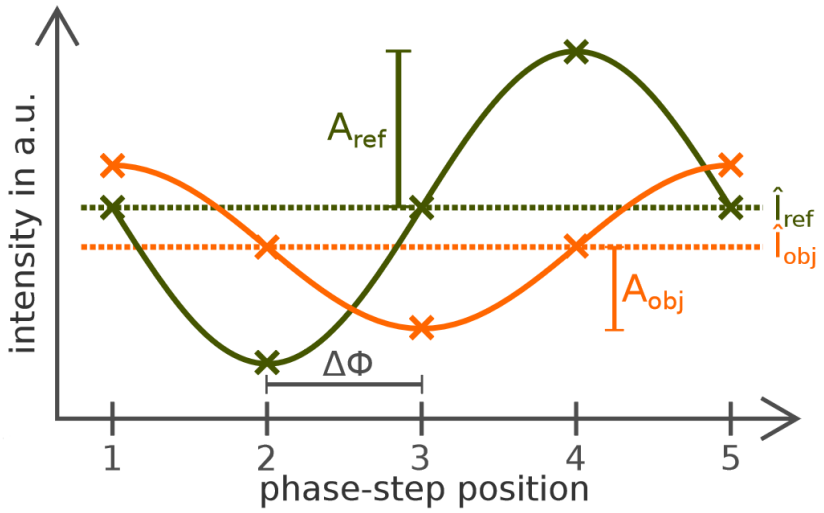

Figure 2.8: Example of phase-stepping curves for a reference scan (green) and an object scan (orange). The intensity is measured for different positions of the G2 grating. From the sinusoidal fit to the measured points (crosses), the mean intensity $\hat{I}$, the visibility (amplitude A), and the phase shift $\Delta\Phi$ can be extracted. Image source: [Lud20].

2.2.3 Signal Modalities: Attenuation, Phase, Dark-Field

Attenuation signal

The attenuation image is calculated from the mean intensity $\hat{I}$ of the phase-stepping curve. It is defined as the ratio of the mean intensity of the object scan to that of the reference scan:

$$\Gamma = -\ln\left(\frac{\bar{I}_{\text{obj}}}{\bar{I}_{\text{ref}}}\right) =: \mu\,. \tag{2.25}$$

This image reflects conventional absorption contrast, as known from standard X-ray imaging. It arises because the object attenuates the X-ray beam depending on its material and thickness, reducing the detected intensity. Attenuation contrast is particularly sensitive to dense structures like bone or calcifications but less effective for soft tissues with similar attenuation.

Differential phase signal

The differential phase-contrast image is obtained from the phase shift $\Delta\Phi$ between the object and reference phase-stepping curves:

$$\Delta\Phi = \Phi_{\text{ref}} - \Phi_{\text{obj}}\,. \tag{2.26}$$

This contrast arises due to refraction of X-rays at interfaces within the object, which causes a slight angular deflection of the wavefront and shifts the interference fringes recorded by the detector.
The differential phase $\Delta\Phi$ can also be expressed in terms of the refractive index decrement $\delta(z)$ as [Lud20]:

$$\Delta\Phi_{\text{abs}} \approx \frac{2\pi d_T}{p_T} \cdot \partial_x \int_0^s \delta(z)\,dz\,, \tag{2.27}$$

with s being the path length in matter and ∂_x the derivative in phase-stepping direction. Since δ is directly related to the electron density and more sensitive to small variations in low-Z materials than the attenuation coefficient β, the phase image provides additional structural information, especially at soft-tissue interfaces [Pag06]. The differential phase image is not further evaluated in this work.

Dark-Field signal

The dark-field image is derived from the relative reduction in visibility V of the interference fringes caused by small-angle scattering (see subsubsection 2.2.4)

within the sample. For a sinusoidal phase-stepping curve with $I_{\max} = \bar{I} + A$ and $I_{\min} = \bar{I} - A$, the visibility defined in Equation 2.23 simplifies to:

$$V = \frac{(\bar{I} + A) - (\bar{I} - A)}{(\bar{I} + A) + (\bar{I} - A)} = \frac{2A}{2\bar{I}} = \frac{A}{\bar{I}} \,. \tag{2.28}$$

The dark-field signal Σ is then defined as:

$$\Sigma = -\ln\left(\frac{V_{\text{obj}}}{V_{\text{ref}}}\right) = -\ln\left(\frac{A_{\text{obj}} \cdot \bar{I}_{\text{ref}}}{A_{\text{ref}} \cdot \bar{I}_{\text{obj}}}\right) \,. \tag{2.29}$$

By extracting the attenuation signal Γ,

$$\Sigma = -\ln\left(\frac{A_{\text{obj}}}{A_{\text{ref}}}\right) - \Gamma \,, \tag{2.30}$$

the dark-field image can be understood as the visibility loss due to small-angle scattering alone, corrected for the intensity reduction caused by attenuation. This formulation decouples the two effects and allows a clearer interpretation of the scattering signal as an independent contrast modality.
The specific mechanisms and limitations underlying the dark-field signal, as well as its sensitivity to particular sub-resolution structures, will be discussed in more detail in the following subsection.

2.2.4 Dark-Field Imaging

Dark-field imaging is particularly useful for identifying and quantifying sub-resolution structures such as alveoli in lung tissue, fibrous materials, or microcalcifications in breast tissue. It provides contrast in regions that appear homogeneous in attenuation and phase images.
To better understand the diagnostic potential of dark-field imaging, this subsection discusses the physical origin of the signal, its mathematical description, and common measurement artifacts such as beam hardening and dispersion effects.

Small-Angle Scattering

The dark-field signal originates from ultra-small-angle X-ray scattering (USAXS), where X-rays are deflected by microscopic structural variations - such as pores, fibers, or grain boundaries. These features are typically much smaller than the spatial resolution of the imaging system. Although they cause neither significant absorption nor refraction, they lead to slight angular deviations of the wavefront, which locally blur the interference fringes and reduce their visibility. This makes dark-field imaging particularly sensitive to microstructures that remain undetectable in conventional attenuation or phase-contrast images.

State of the Art in Dark-Field Breast Imaging

A key advantage of dark-field imaging lies in its sensitivity to structures far below the spatial resolution of the detector, often referred to as subpixel structures. Even such minute features can cause detectable visibility loss due to wavefront distortions on a very small angular scale.
A promising medical application under active investigation is breast imaging, particularly for the detection of microcalcifications. It also represents the targeted application of the imaging setup developed in this work. Anton et al. demonstrated that grating-based dark-field imaging can reveal fibrous structures and microcalcifications in human breast tissue that are not visible in conventional absorption mammography [Ant+13]. Michel et al. further showed that microcalcifications only a few micrometers in size produce a distinct dark-field signal due to their fine internal composition, thereby enhancing their detectability in mammographic imaging [Mic+13].
Emons et al. applied dark-field imaging in a preclinical setting and showed that tumor-associated microcalcifications, invisible in standard mammograms, can be revealed using dark-field contrast. As shown in Figure 2.9, the lesion marked by the white arrow is only visible in the dark-field image [Emo+20].
To enable further developments towards quantitative medical imaging and computed tomography, a mathematical description of the dark-field signal is essential. One such approach is discussed in the following subsection.

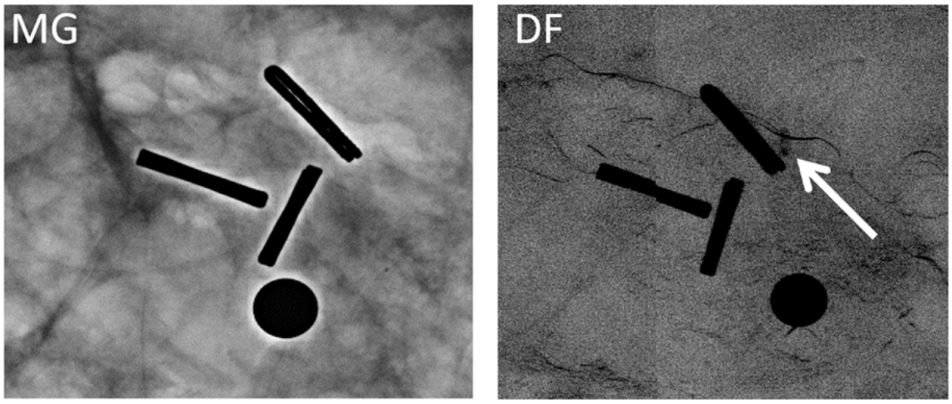

Figure 2.9: Comparison of conventional mammography (left, inverted image) and X-ray dark-field imaging (right) of a human breast specimen. The white arrow indicates a tumor-associated microcalcification that is clearly visible in the dark-field image but not detectable in the mammographic image. Adapted from Emons et al. [Emo+20].

Linear Diffusion Coefficient

To quantify the visibility loss due to scattering, the linear diffusion coefficient ϵ was introduced by Bech et al. [Bec+10]. This material-specific parameter describes the scattering strength per unit length and plays a role analogous to the linear attenuation coefficient μ in conventional X-ray imaging.
The coefficient ϵ is linked to the angular scattering distribution $A(\theta)$, which is typically characterized by its standard deviation σ. According to Rigon et al. [Rig+08], this width depends on the slice thickness Δz and the intrinsic scattering properties of the material. Bech defined the diffusion coefficient as

$$\epsilon \equiv \frac{\sigma^2}{\Delta z}\,, \tag{2.31}$$

which expresses the angular scattering power per unit path length.
Assuming a Gaussian scattering distribution, the dark-field visibility V decreases exponentially with the projected scattering power [Bec+10]:

$$V = \exp\left(-\frac{2\pi^2 d^2}{p_2^2}\int \epsilon(z)\,dz\right)\,, \tag{2.32}$$

where p_2 is the period of the analyzer grating and d the distance between G1 and G2. This relation forms the basis for tomographic reconstruction of spatially resolved diffusion coefficient maps.

Beam Hardening and Dispersion Artifacts

Although dark-field contrast ideally reflects only small-angle scattering, measurements with polychromatic X-ray spectra are affected by energy-dependent artifacts. Pelzer et al. [Pel+16] identified two dominant effects: Beam hardening results from the preferential absorption of low-energy photons, which alters the effective spectrum and can reduce fringe visibility even in the absence of scattering. Dispersion artifacts occur when fringe positions vary slightly with photon energy, leading to averaging effects and apparent visibility loss.
To address these effects, Pelzer et al. simulated the expected dark-field signal as a function of attenuation and phase shift. Based on this, they constructed a correction matrix $D_{\text{art}}(\Gamma, \Phi)$, which allows isolating the scattering component via

$$D_{\text{scatter}} = \frac{\Sigma}{D_{\text{art}}}\,. \tag{2.33}$$

Applied to dark-field mammography, this correction significantly reduced anatomical background and increased the visibility of microcalcifications by an average of 7% [Pel+16]. It thus improves the diagnostic reliability of dark-field imaging, particularly in soft-tissue applications.

2.3 Computed Tomography

Computed tomography (CT) reconstructs a three-dimensional representation of an object by acquiring multiple X-ray projections from different angles. This section provides an overview of the data acquisition process, reconstruction techniques, and the limitations of conventional absorption-based CT imaging.
CT has a long history, beginning with the mathematical foundations established by Johann Radon in 1917 [Rad17], followed by the first prototypes developed by Godfrey Hounsfield in 1969 [Hou73], and leading to advancements such as Spiral-CT, introduced by Willi A. Kalender in 1989 [Kal+90].
For simplicity, the fundamental principles of CT will first be described in the context of conventional, well-known, absorption-based imaging. Dark-field imaging, its advantages, and its integration into CT will be discussed later in subsection 2.3.4.

2.3.1 Acquisition Geometry and System Overview

In clinical computed tomography, the X-ray source and detector are mounted on a rotating gantry that moves around the patient to acquire projection images from multiple angles. This configuration enables rapid data acquisition and continuous scanning, as implemented in modern spiral CT systems [Kal+90]. For accurate tomographic reconstruction, the system must acquire projections over at least 180° to ensure full sampling of all object regions.
In experimental and preclinical setups - such as the one used in this work - the geometry is often reversed: instead of rotating the gantry, the sample is placed on a high-precision rotation stage, while the source and detector remain stationary. This setup is particularly advantageous for compact laboratory systems, as it simplifies mechanical design and allows for flexible integration of custom components.
The detector used in this work is a photon-counting detector, which combines high spatial resolution with energy sensitivity. A detailed description of its physical detection principle and performance characteristics is given in the following subsection.

2.3.2 Photon-Counting Detectors

Photon-counting detectors (PCDs) directly convert incident X-ray photons into electrical signals using semiconductor materials such as silicon or cadmium telluride (CdTe). When a photon interacts with the detector, it generates electron-hole pairs that are separated by an applied electric field, resulting in a current pulse. The amplitude of this pulse is proportional to the photon's energy, allowing for energy discrimination via adjustable threshold levels. In multi-threshold systems,

events are sorted into energy bins, enabling spectral imaging with simultaneous acquisition of multiple energy-resolved datasets.
Compared to conventional energy-integrating detectors, PCDs offer several advantages for medical imaging. Their ability to reject electronic noise and to perform energy discrimination enhances soft-tissue contrast and reduces anatomical background, as demonstrated in contrast-enhanced spectral mammography by Fredenberg et al. [Fre+10]. Techniques such as energy weighting or dual-energy subtraction further improve the signal-difference-to-noise ratio (SDNR), especially in dense tissue where conventional detectors are limited [Fre+10]. Additionally, PCDs provide high spatial resolution and intrinsic scatter rejection, making them particularly suitable for advanced applications like dark-field or spectral CT.

Charge Trapping in CdTe-based Photon-Counting Detectors

In CdTe-based photon-counting detectors, charge trapping occurs when electrons or holes are captured by defects or impurities in the crystal before reaching the electrodes. These defects - such as tellurium inclusions, dislocations, or grain boundaries - are often introduced during crystal growth and processing [Del+09]. Carriers that are trapped do not contribute to the output signal, resulting in a loss of measured charge.
This effect is particularly relevant in CdTe because the mobility and lifetime of holes are significantly lower than those of electrons. Consequently, hole trapping is the dominant mechanism leading to incomplete charge collection [TI13]. The amount of collected charge depends on the interaction depth, i.e., the distance between the interaction site and the readout electrode, which introduces depth-dependent signal variations.
Trapping reduces the amplitude of the detected pulse and causes the measured photon energy to appear lower than it actually is. This results in a shift of the energy spectrum toward lower energies and produces a characteristic low-energy tail, especially for high-energy photons [TI13].
To mitigate charge trapping, high bias voltages are applied to accelerate carrier transport and reduce the probability of trapping [TI13]. Further improvements include enhancing crystal quality through purification and defect reduction, as well as implementing correction algorithms that compensate for depth-dependent charge loss [Del+09].

2.3.3 CT Image Reconstruction and Artifacts

After the data has been recorded, it must be processed and used to reconstruct a three-dimensional image. In the following, the individual steps of this reconstruction process are examined, including the representation of the raw data, the mathematical principles behind tomographic image formation, and common artifacts in computed tomography.

Sinogram and Radon Transform

The raw projection data acquired in CT are commonly visualized in the form of a sinogram. A sinogram represents the signal recorded by a single detector row over a range of projection angles. Each row corresponds to a specific rotation angle of the X-ray source, while each column reflects a detector element. The resulting image shows how the intensity measured at each detector pixel changes as the system rotates, as illustrated in Figure 2.10.
If the measured intensities I have been normalized to a flat-field image I_0, the values correspond to the transmission $T = I/I_0$. A single point in the object produces a sinusoidal trace across the sinogram due to the changing projection angle, giving rise to the name "sinogram". High-attenuation structures such as bone appear as bright regions, while soft tissues appear darker. Artifacts like patient motion or detector defects manifest as distortions in the sinogram, which propagate into the reconstructed image.

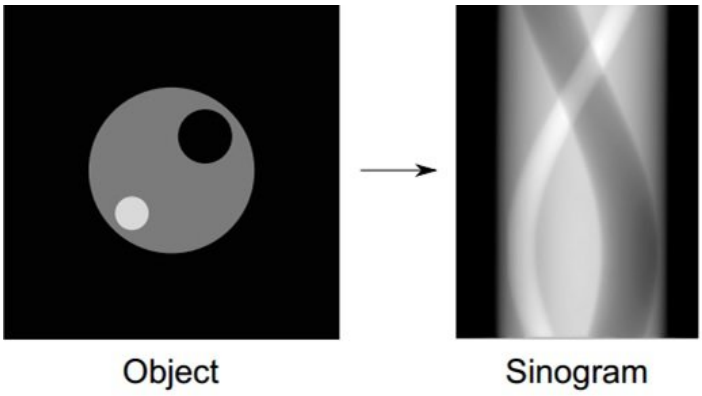

Figure 2.10: Illustration of how a simple object's projection data is represented in a sinogram. In some cases, the sinogram may be rotated by 90 degrees, which results in the horizontal and vertical axes being interchanged. Image source: [AME17]

The sinogram data mathematically correspond to the Radon transform of the object $f(x, y)$. Introduced by Johann Radon in 1917 [Rad17], the transform describes the

line integrals of a function along projection directions defined by angle θ and offset s. In CT, this models the total attenuation along each ray path:

$$\mathcal{R}f(\theta, s) = \int_{-\infty}^{\infty} f(s\cos\theta - t\sin\theta,\ s\sin\theta + t\cos\theta)\,\mathrm{d}t\,. \tag{2.34}$$

Filtered Backprojection (FBP)

While modern CT systems increasingly use iterative algorithms to improve image quality, this work relies on the classical filtered backprojection (FBP) method due to its simplicity and computational efficiency [KHP11].

Slice Theorem. The Fourier slice theorem provides the mathematical basis for FBP. It states that the one-dimensional Fourier transform of a projection at angle θ corresponds to a radial line through the two-dimensional Fourier transform of the object at the same angle [KHP11; SKJ18]:

$$\mathcal{F}_s\left\{\mathcal{R}f(\theta, s)\right\} = \mathcal{F}_{x,y}\left\{f(x, y)\right\}\,. \tag{2.35}$$

By collecting projections from multiple angles, the entire frequency space can be filled, allowing the reconstruction of the original image. Since low frequencies are inherently overrepresented in this process, filtering becomes necessary to restore a balanced frequency response.

Ram-Lak Filter. The FBP algorithm reconstructs $f(x, y)$ in two main steps: filtering of the projections and backprojection over the image space.
Each projection $p(\theta, s) = \mathcal{R}f(\theta, s)$ is first filtered in the frequency domain using a high-pass filter. A commonly used filter is the Ram-Lak filter, defined by $H(\omega) = |\omega|$, which amplifies high-frequency components to compensate for the smoothing effect of backprojection [SKJ18].
The filtered projection $p_{\text{filt}}(\theta, s)$ is obtained by applying the filter in the frequency domain and transforming back:

$$p_{\text{filt}}(\theta, s) = \mathcal{F}_s^{-1}\left\{H(\omega)\cdot\mathcal{F}_s\left\{p(\theta, s)\right\}\right\}\,. \tag{2.36}$$

Backprojection. In the second step, the filtered projections are backprojected across the image domain. For each angle θ, the filtered values are distributed ("smeared") along the corresponding X-ray paths in the image plane. The full reconstruction is obtained by integrating over all projection angles [SKJ18]:

$$f(x, y) = \int_0^{\pi} p_{\text{filt}}(\theta, x\cos\theta + y\sin\theta)\,\mathrm{d}\theta\,. \tag{2.37}$$

Figure 2.11 illustrates how the number of projections and the use of filtering affect image quality in backprojection.

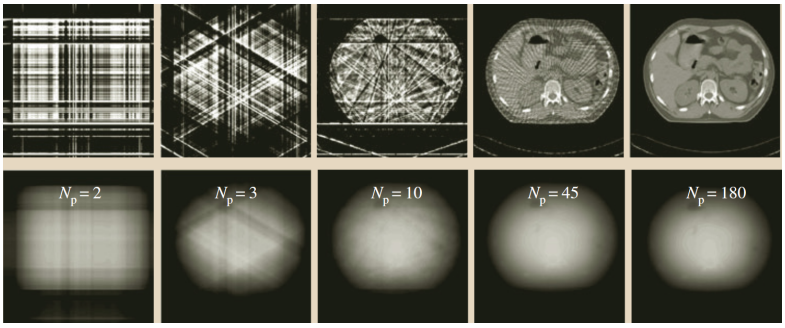

Figure 2.11: Accumulation of all backprojections of the high-pass filtered (top) and unfiltered (bottom) projection profiles for different numbers of projections N_p [KHP11]. From left to right: $N_p = 2, 3, 10, 45, 180$.

Gray Level Mapping

In computed tomography, image intensities are often represented on a standardized scale, such as Hounsfield Units (HU), which relate the attenuation coefficient μ to that of water [Hou73]:

$$\mathrm{HU} = 1000 \cdot \frac{\mu - \mu_{\mathrm{water}}}{\mu_{\mathrm{water}}} \,. \tag{2.38}$$

Water is defined as 0 HU, air as –1000 HU, and dense materials such as bone have positive values. In this work, reconstructed data are stored as 16-bit grayscale images with 65,536 levels. These `.tiff` files are used for visualization and further processing. While the human eye can distinguish only around 1024 gray levels [KT07], the extended bit depth ensures maximum data preservation and flexibility for windowing. *Windowing* is a technique used to define the visible gray value range by specifying a window level C and width W. Adjusting these parameters allows highlighting of different tissue types depending on the imaging task.

CT Artifacts

Computed tomography images can exhibit characteristic artifacts that degrade image quality and may impair diagnostic accuracy. Among the most common types are beam hardening and ring artifacts [KHP11]. Beam hardening manifests as dark streaks between dense objects or a cupping effect within homogeneous regions. It arises from the preferential absorption of low-energy photons, which shifts the effective energy spectrum toward higher energies as the beam traverses dense materials like bone or metal. Ring artifacts appear as concentric circles centered around the rotation axis and result from faulty or miscalibrated detector elements. Since each detector pixel contributes a circular trace during image formation, even minor inconsistencies can cause visible distortions.

2.3.4 Grating-Based Dark-Field CT Imaging

Grating-based dark-field computed tomography (DFCT) is an imaging modality that extends conventional CT by enabling tomographic reconstruction of small-angle X-ray scattering. It builds on the principles of grating interferometry and allows for the visualization of microstructural information that is not accessible via absorption contrast. This section discusses the current state of research on DFCT, including quantitative reconstruction strategies, the definition of standardized contrast scales, and known limitations of the method.

Advantages of DFCT

Although some advantages of dark-field CT have been mentioned earlier, it is important to highlight the key limitations of conventional absorption-based CT in soft-tissue imaging. First, the contrast between soft tissues is often limited, as many soft tissues exhibit similar attenuation properties and are therefore difficult to differentiate. Second, structures that fall below the spatial resolution of the system remain undetectable, even if they are clinically significant. Third, absorption-based CT lacks sensitivity to phase shifts and small-angle scattering, which can carry valuable information about microstructural features, particularly in fibrous or weakly absorbing tissues.

These limitations motivate the use of complementary techniques such as dark-field CT, which offers additional contrast by detecting scattering from structures that are not directly resolvable.

Quantitative Reconstruction: Inverse Radon Transform

Bech et al. [Bec+10] demonstrated that the dark-field signal can be reconstructed using a filtered backprojection (FBP) approach analogous to conventional CT. Assuming that the logarithmic visibility reduction is linearly additive along the X-ray path, the inverse Radon transform can be applied to the signal Σ.

Following the formalism of Equation 2.37, the linear diffusion coefficient $\epsilon(x, y)$ is reconstructed as:

$$\epsilon(x, y) = \int_0^{\pi} p_{\text{filt}}(\theta, x\cos\theta + y\sin\theta)\,\mathrm{d}\theta\,, \tag{2.39}$$

where $p_{\text{filt}}(\theta, s)$ denotes the filtered projection of $-\ln V(\theta)$. This formulation enables quantitative mapping of scattering contrast and allows for direct comparison with attenuation-based reconstructions.

HU Units in Dark-Field CT

To facilitate interpretation and standardization, Viermetz et al. [Vie+22] introduced a Hounsfield-like unit for dark-field CT, defined as:

$$\mathrm{DFHU} = 1000 \cdot \frac{\epsilon - \epsilon_{\mathrm{H_2O}}}{\epsilon_{\mathrm{H_2O}}}, \tag{2.40}$$

where ϵ is the reconstructed linear diffusion coefficient and $\epsilon_{\mathrm{H_2O}}$ that of water. This scaling allows for an intuitive representation of dark-field contrast and supports gray level mapping strategies similar to those used in classical CT. In this work, DFCT reconstructions are exported as 16-bit `.tiff` images with linearly mapped gray values, analogous to the attenuation-based reconstructions.

Artifacts in DFCT Reconstructions

DFCT introduces specific artifacts that are not present in classical absorption-based CT. As discussed by Graetz et al. [Gra+20], two major effects must be considered:
- *Distance-dependent signal variation*: In cone-beam setups, the correlation length ξ depends on the sample-to-detector distance d, which leads to angle-dependent variations in the measured scattering signal. Without correction or symmetric acquisition, this can result in blurring or geometric distortion in the reconstruction.
- *Orientation-dependent contrast*: The dark-field signal depends on the relative orientation between anisotropic microstructures in the sample and the sensitivity direction of the interferometer. As a result, directional artifacts may occur in the reconstructed volume if these effects are not accounted for.

Although no corrections are applied in this work, both effects are well documented and should be considered in future optimization and interpretation steps.

3 Detector Characterization

Before performing grating-based computed tomography experiments, a thorough characterization of the detector was carried out. This chapter presents a series of experiments designed to investigate the detector's basic performance and response characteristics. These include studies on linearity, noise behavior, stability, and spatial resolution. The goal of these measurements was to gain a detailed understanding of the detector's behavior under controlled conditions and to ensure reliable performance in subsequent imaging experiments. Only after completing this characterization was the detector integrated into the grating-based dark-field CT setup, which is described in the following chapters.

3.1 Technical Description of the Detector

The detector in use throughout this work is a DECTRIS EIGER2 R CdTe 1M hybrid photon-counting detector, shown in Figure 3.1. Designed for high-resolution X-ray imaging, this system employs a cadmium telluride (CdTe) sensor with energy thresholding functionality. Its architecture enables noise-free signal acquisition and supports high temporal resolution. An overview of the most relevant technical specifications is provided in Table 3.1, based on the official documentation from the manufacturer [DEC24b].

Sensor Design and Active Area The detector consists of two vertically stacked modules, each equipped with a CdTe sensor of 750 µm thickness. Together, they form a pixel matrix of 1028×1062 square pixels with a pitch of 75 µm, resulting in a total active area of $77.1\,\text{mm} \times 79.65\,\text{mm}$. This high granularity enables fine spatial resolution, which is essential for dark-field imaging and spatial frequency analysis.

Module Gaps and Pixel Layout A characteristic geometric feature of this detector is the presence of physical gaps in the pixel matrix. A horizontal inter-module gap of 38 pixels separates the two modules, while each module also includes a vertical intra-module gap of 2 pixels in the center. These inactive regions do not detect X-rays and must be accounted for during image correction and reconstruction.

Figure 3.1: Photograph of the DECTRIS EIGER2 R CdTe 1M detector in use for all measurements. Image source: [DEC25].

Photon Counting and Thresholding The hybrid photon-counting architecture allows for detection without readout noise or dark current. Each pixel includes logic to discriminate incoming photons based on their energy. Two independent thresholds can be defined within a range of 4–30 keV, enabling basic spectral imaging or suppression of low-energy background. The effective operating range during standard acquisition is typically between 8 and 25 keV.

Readout and Dynamic Range The detector supports continuous readout with a minimum dead time of 100 ns and achieves frame rates of up to 1100 Hz. Data can be exported in either 16-bit or 32-bit format, while the internal signal processing is performed at 16-bit depth. The 32-bit mode is useful when both thresholds are active or when a higher dynamic range is required. The specified maximum count rate of 9.8×10^8 photons/s/mm^2 is sufficient for both transmission and scattering measurements.

Environmental Conditions All measurements were performed at ambient pressure with active thermal stabilization at approximately 25 °C. A continuous flow of dry air prevented condensation and ensured thermally stable operating conditions throughout the experiments.

Practical Detector Control in Python

For all characterization measurements, the detector was controlled via a custom Python interface developed by Markus Schneider and Constantin Rauch. This setup provided a simple and robust framework for operating the EIGER2 system.

Each measurement was initiated using a Python function call of the form `data = acquisition(...)`, where acquisition parameters such as the following were passed as arguments:

- `nimages`: number of images to be recorded,
- `count_time`: exposure time per image (in seconds),
- `threshold_1` and `threshold_2`: energy thresholds for photon discrimination.

The resulting image stack was saved manually as an HDF5 file, which also included all relevant metadata such as X-ray tube settings, geometry, and additional acquisition parameters. This approach enabled fast and flexible data collection tailored to each specific experiment. Further technical information on detector operation can be found in the official user manual [DEC24a].

Detector Type	Hybrid Photon Counting (HPC)
Sensor Material	Cadmium Telluride (CdTe)
Sensor Thickness	750 µm
Pixel Size	75 µm × 75 µm
Pixel Array (W × H)	1028 × 1062 pixels
Active Area (W × H)	77.1 mm × 79.65 mm
Inter-Module Gap	38 pixel (horizontal)
Intra-Module Gap	2-pixel-wide vertical gap per module
Energy Range	8 keV – 25 keV
Adjustable Thresholds	2 (independent), 4 – 30 keV
Max. Frame Rate	1100 Hz
Point Spread Function (FWHM)	1 pixel
Readout Mode	Continuous (dead time: 100 ns)
Max. Count Rate	9.8×10^8 photons/s/mm^2
Image Bit Depth	16 or 32 bit
Readout Bit Depth	16 bit

Table 3.1: Key specifications of the EIGER2 R CdTe 1M detector. [DEC24b]

3.2 Transmission Measurements

As a first experiment with the new detector system, a set of energy-resolved transmission measurements was performed to explore its response behavior under realistic conditions. For this purpose, seven thin metal foils of known composition and thickness were prepared as test samples. Each foil was laminated in standard plastic film and had a minimum area of 1 cm × 1 cm. The following materials and thicknesses were used:

Copper, 50 µm	Copper, 15 µm	Aluminum, 10 µm	Aluminum, 20 µm
Titanium, 2 µm	Gold, 1 µm	Nickel, 12 µm	

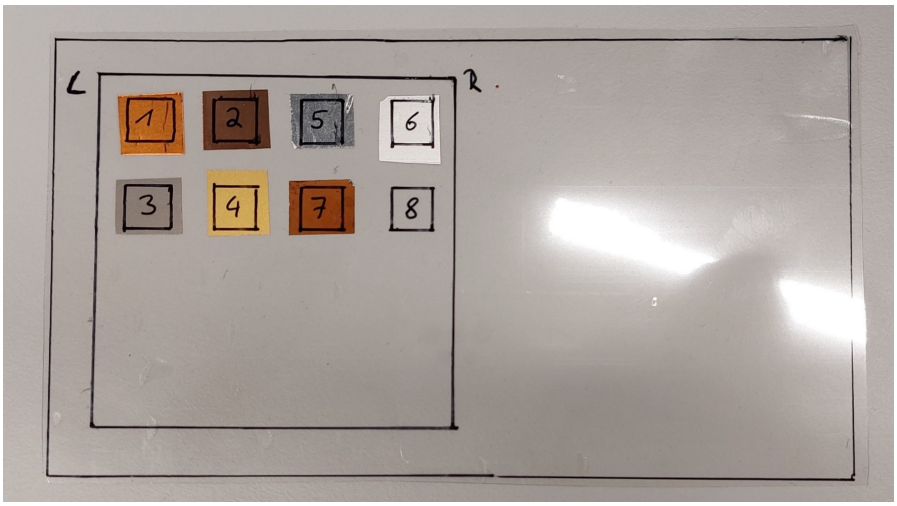

Figure 3.2: Photograph of the laminated metal foil sample used for the transmission measurements. Note: later acquired detector images are vertically mirrored, as those are shown from the detector's point of view.

A motorized linear stage is used to repeatedly position the sample into and out of the beam path. This setup allows for consistent switching between object and reference acquisitions without manual repositioning, ensuring reproducibility and minimizing alignment errors.
For each threshold setting between 4 keV and 40 keV (in 1 keV increments), 10 projections of 10 seconds exposure time each are acquired, yielding a total integration time of 100 s per threshold. The measurements are performed at 50 kV tube voltage and 500 µA tube current.
By subtracting successive threshold images (e.g., 4 keV − 5 keV), the number of photons within 1 keV-wide energy bins is estimated. Combined with corresponding flat-field images taken for each threshold - using only the plastic foil as a reference - the transmission of each metal foil is calculated for all energy bins.

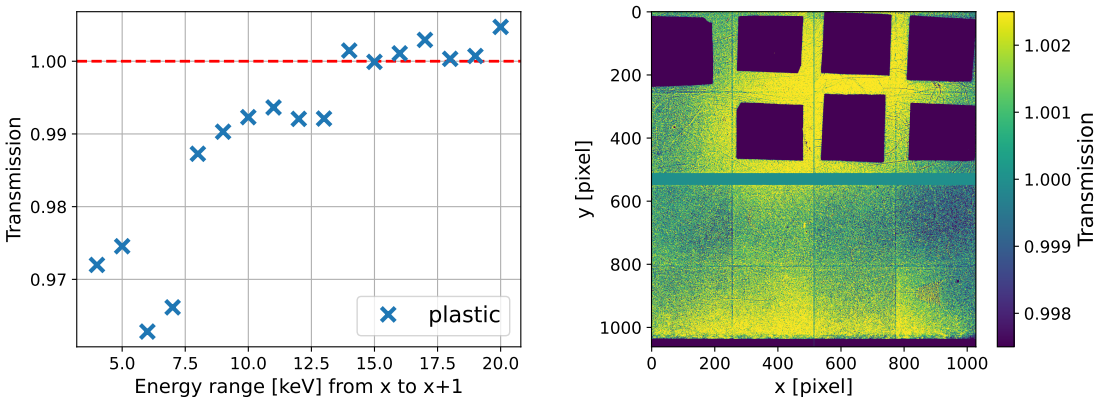

Figure 3.3: Left: Measured transmission of the plastic laminate as a function of energy. A non-physical transmission > 1 is observed above approximately 14 keV. Right: Transmission map of the plastic region with the metal foils for threshold set to 5+ keV. Increased intensity in the upper and lower parts of the image becomes clearly visible, most likely caused by beam geometry and scattering from the metal holder (dark-blue at the bottom).

Analysis

An initial analysis of the reference data reveals a non-physical effect: the transmission of the plastic (laminate) relative to air exceeds unity for energies above approximately 14 keV, see Figure 3.3 (left). This provides an early indication of potential systematic effects. One likely explanation is secondary radiation caused by the metal sample holder, which is located at the bottom of the setup on the side of the metal foils and contributes significantly to the detected intensity in the lower detector region. In addition, an increased signal in the upper detector region is observed, which is most likely caused by the beam orientation and the angular emission profile of the X-ray source. Figure 3.3 (right) shows the transmission map for detected photon energies of 5+ keV.

Since this parasitic signal is independent of the threshold energy, its effect becomes particularly evident when the transmission of the actual sample is low (i.e., at lower energies). At higher energies, where the plastic becomes more transparent, this additive contribution can artificially increase the measured transmission above 1.

Another possible source of error is temporal drift. The time between two consecutive threshold measurements is around six minutes, and the entire series takes approximately 3.5 hours to complete. The investigation of such time-dependent effects and potential detector instability is postponed to the next section.

Comparison with Theoretical Transmission

Figure 3.4 shows the calculated transmission values for all 7 metal foils and every energy bin. A consistent local minimum is observed between 7 and 9 keV for all materials, followed by a noticeable jump between 9 and 10 keV. These features suggest a systematic error in the acquisition, possibly caused by incorrect exposure settings, detector response, or slight misalignment during the repositioning of the sample.

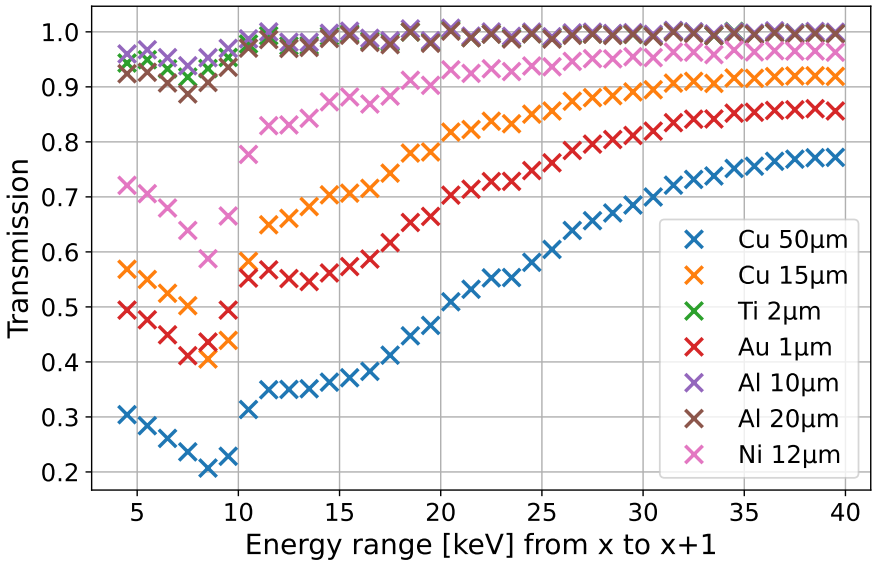

Figure 3.4: Measured transmission curves of all metal foils as a function of photon energy. Each curve corresponds to one material and thickness as listed in the legend. The energy bins are 1 keV wide and derived from successive threshold image differences.

Despite these limitations, the measured transmission curves for selected metal foils - namely Cu (50 µm), Al (20 µm), Au (1 µm), and Ti (2 µm) - are compared to theoretical predictions based on tabulated attenuation coefficients from the CXRO database [HGD93]. As shown in Figure 3.5, the general shape and energy dependence of the experimental curves agree reasonably well with the theoretical expectations, indicating that the energy-resolved transmission measurement method is fundamentally valid.
However, significant and systematic deviations in absolute transmission values are observed, particularly in the lower energy range. Across all materials, the measured transmission exceeds theoretical values by up to 20%–30%. This discrepancy is most likely caused by a combination of factors. First, scattered radiation reaching the detector may lead to artificially elevated intensity values, especially

in the presence of surrounding components such as the sample holder. Second, spectral non-idealities of the X-ray source, such as beam hardening or an inaccurate description of the actual photon flux, can affect the energy calibration and intensity normalization. Third, small uncertainties in the effective thickness or homogeneity of the foils may also contribute.
In all measured curves, consistent localized anomalies are observed that are not expected from the theoretical attenuation behavior. Notably, a distinct local minimum is present between 8 and 9 keV, followed by an abrupt increase in transmission between 9 and 10 keV for each material. One possible explanation for this pattern is charge trapping in the CdTe sensor material, an effect that was discussed in subsection 2.3.2.
Incomplete charge collection for low-energy photons can reduce the effective detection efficiency, especially near the threshold edge, which may cause the measured transmission to appear artificially elevated in specific energy bins. Additional factors such as detector nonlinearity, threshold miscalibration, incorrect exposure settings, or small mechanical misalignments during repeated measurements may also contribute to these systematic features.

Conclusion

These measurements were conducted as a first test to explore the detector's performance and to gain practical experience with energy-resolved acquisition. While the results qualitatively confirm the expected energy dependence of transmission and demonstrate the basic functionality of the method, noticeable systematic deviations are present. These include absolute offsets in the measured transmission values as well as reproducible anomalies in specific energy ranges, most prominently a local minimum between 8–9 keV and a sharp increase between 9–10 keV.
Such discrepancies are likely caused by a combination of scattered radiation, spectral non-idealities of the source, and suboptimal acquisition parameters - particularly since these were the very first measurements performed with the system. With improved understanding of detector behavior, calibration, and experimental workflow over the past year, now repeated measurements are expected to yield significantly better agreement with theory.
Additionally, a possible temporal drift of the detector response during the long measurement duration may have contributed to the observed deviations. This aspect will be investigated in more detail in the following section.

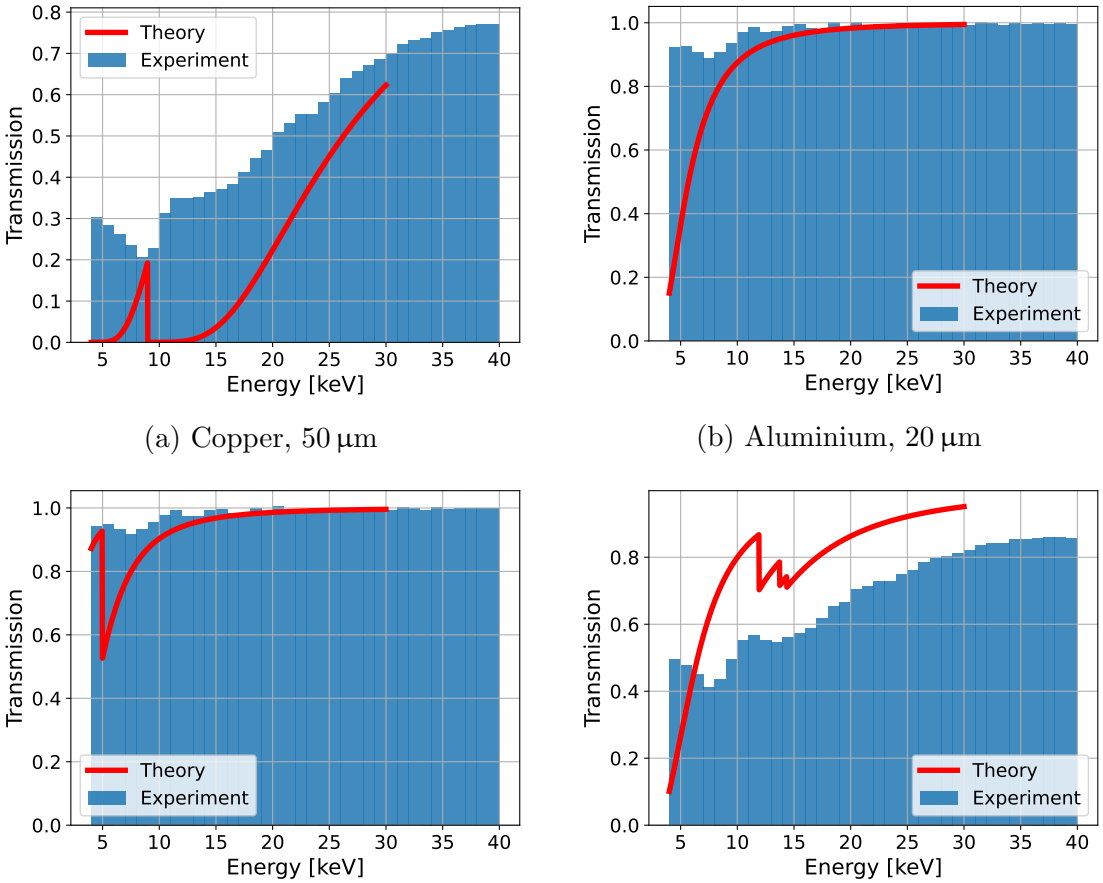

(a) Copper, 50 µm

(b) Aluminium, 20 µm

(c) Titanium, 2 µm

(d) Gold, 1 µm

Figure 3.5: Comparison of measured and theoretical transmission for selected metal foils laminated in plastic. Experimental values are derived from energy-resolved photon counts and normalized using flat-field measurements of the laminate only. Theoretical curves are based on tabulated attenuation coefficients from CXRO [HGD93].

3.3 Temporal Analysis

In the previous section, a potential time-dependence of the detector signal was observed based on projection images acquired over several hours. These acquisitions were performed with alternating energy threshold settings, but one threshold was kept constant at 4 keV throughout the measurement. This allows us to further investigate the effect of acquisition time on the measured intensity using the 4 keV threshold-channel of the same dataset.
The full measurement took approximately 3.5 hours and includes 37 acquisitions. Each scan consisted of both an object measurement (plastic phantom with metal foils) and a reference measurement (plastic only). The interval between two acquisitions was consistently just under six minutes. In the following, we analyze how the average number of counts per pixel evolves over time. For this purpose, we first plot the absolute development of the average count values per image and then calculate the relative percentage change between each pair of successive acquisitions.

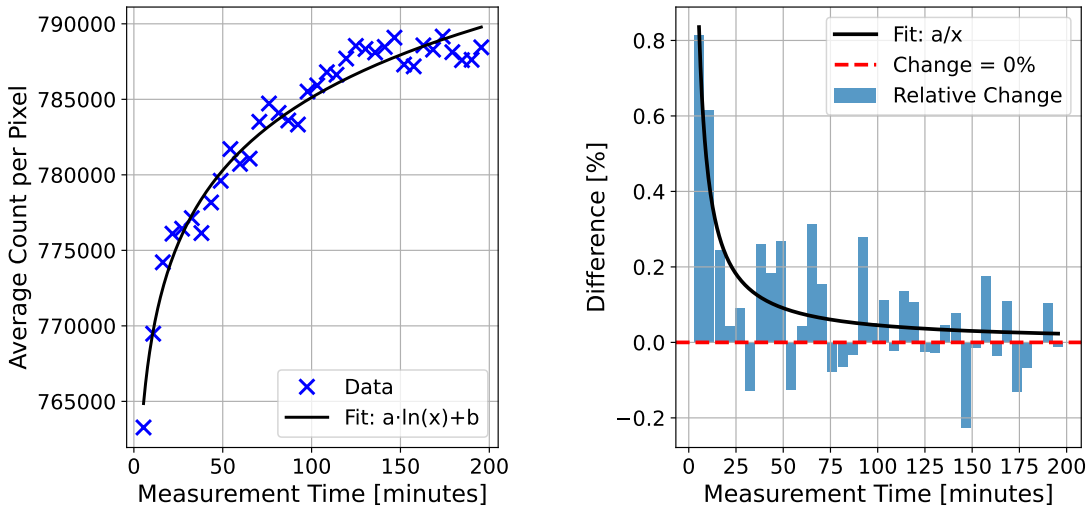

(a) Absolute average counts per pixel over time with an ln-Fit.

(b) Relative change in average counts between successive acquisitions.

Figure 3.6: Temporal evolution of the detector signal at 4 keV threshold over the course of 37 acquisitions, resp. 3.5 hours total and 6 minutes between 2 acquisitions.

From these plots, a clear trend can be observed: the average count rate increases significantly during the initial phase and begins to saturate after approximately two hours (120 minutes). This behavior likely reflects thermal or electronic stabilization processes in the detector or X-ray tube.

To assess how this temporal variation affects spatial image properties, we compare the first and last acquisitions of the series. Figure 3.7 shows the pixel-wise relative difference in photon count between object scan 1 and 37, normalized to the values of scan 1. The two scans were acquired 3.5 hours apart.

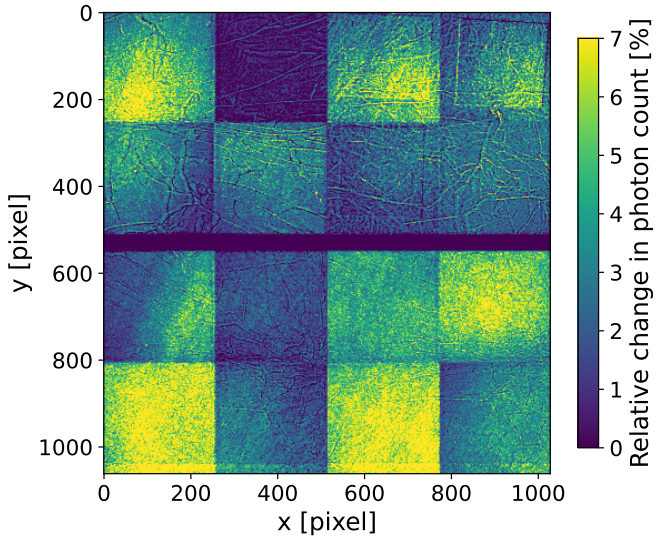

Figure 3.7: Pixel-wise relative difference in photon count between object scan 1 and 37, normalized to scan 1: $(\mathrm{Obj}_{37} - \mathrm{Obj}_1)/\mathrm{Obj}_1$. The two scans were acquired 3.5 hours apart. The image reveals a spatially inhomogeneous temporal response of the detector, with clear module borders and stripe-like structures likely caused by charge trapping and sharing effects.

The comparison reveals several notable effects. The modular structure of the detector becomes clearly visible, with individual modules responding differently to temporal changes. Further, stripe-like patterns emerge across the detector, which are most likely caused by charge trapping or charge sharing effects. The visible edges of the metal foils, despite being a difference image over time, suggest a slight shift in the focal spot of the X-ray source during the measurement period. This leads to a small lateral displacement of the projected structures and causes contrast features, such as the edges of strongly absorbing metal foils, to appear asymmetrically in the difference image: one side of each edge appears darker, while the opposite side appears brighter.
The observed spatial non-uniformities and varying responses of neighbouring pixels or modules highlight the need for appropriate correction methods. These effects will be discussed in more detail in section 3.6 and 4.1, where the quality of individual pixels are further examined, and flat-field correction strategies and their impact on image quality are presented.

3.4 Tube Current and Intensity

In this section, the relationship between the tube current setting and the detected photon count is investigated. The primary aim of this measurement was to verify the stability of the X-ray source, both on its own and in conjunction with the detector system. By assessing the linearity between tube current and signal intensity, potential fluctuations or instabilities of the tube output, as well as non-linearities in the combined source-detector response, can be excluded.
Measurements were performed for tube currents of 4.5, 10, 20, 30, 40, and 45 mA, while keeping all other acquisition parameters constant. For each setting, the average number of detected photons per pixel was calculated. The standard deviation across the detector area was used as a measure of uncertainty.
As shown in Figure 3.8, the resulting data exhibit a perfectly linear relationship. All measured data points lie exactly on the fitted line, confirming the expected proportionality between tube current and detected signal. This demonstrates that the X-ray tube operates in a stable and reproducible manner across the tested range and that no detectable deviations or instabilities occur in the overall acquisition chain.

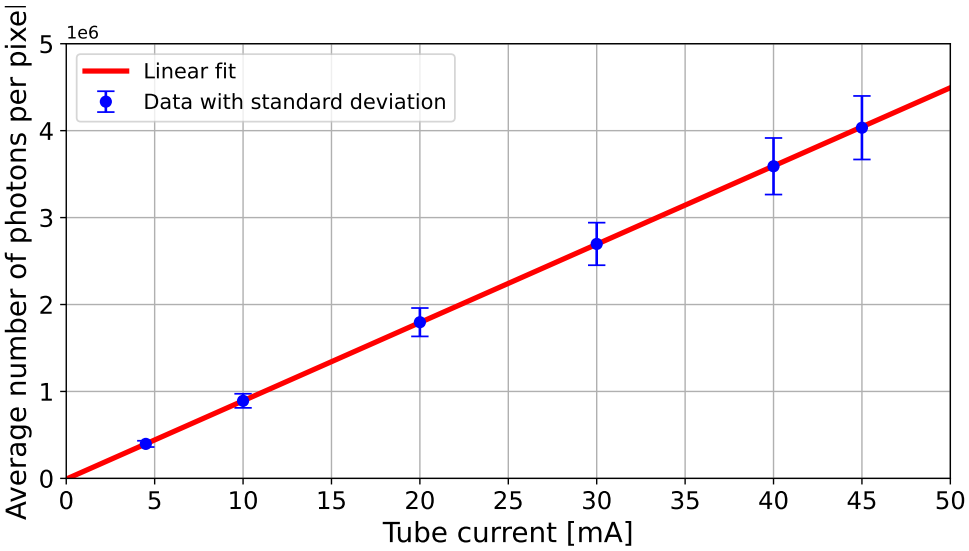

Figure 3.8: Average number of photons per pixel as a function of tube current. A linear fit confirms the expected proportionality. All data points lie on the fitted line. Error bars represent the standard deviation across the detector area.

3.5 Spatial Resolution

A key performance characteristic of any X-ray imaging system is its spatial resolution, which defines the smallest structures that can be reliably distinguished in an image. This section evaluates the spatial resolution in the current setup. A central tool for this purpose is the Modulation Transfer Function (MTF), which provides a frequency-dependent description of contrast preservation.

Modulation Transfer Function

The Modulation Transfer Function (MTF) offers a quantitative description of how an imaging system transmits contrast as a function of spatial frequency. Higher spatial frequencies correspond to finer structures ($s \propto f^{-1}$) and are typically expressed in *line pairs per millimeter* (lp/mm). Intuitively, the MTF describes how close two point sources can be brought together before their signals begin to overlap to such an extent that they are no longer distinguishable in the image. The higher the MTF at a given spatial frequency, the better the system's ability to resolve fine structural detail.
In this work, the MTF was determined using the *Slanted-Edge Method*, a widely used technique in which the sharp edge of a high-attenuation object is imaged at a slight angle relative to the detector grid [Sta]. From the resulting edge-spread function (ESF), the line spread function (LSF) is derived [Rei91], and its Fourier transform yields the MTF [EM04]:

$$\mathrm{MTF}(f) = \frac{M_{\mathrm{image}}(f)}{M_{\mathrm{object}}(f)}\,, \tag{3.1}$$

with $M(f)$ denoting the modulation (i.e., relative contrast) at a given spatial frequency f. In ideal systems, all spatial frequencies would be transmitted equally (MTF = 1), but real systems exhibit a decline in MTF with increasing frequency due to factors such as detector blur, focal spot size, and system geometry.
The frequency at which the MTF drops to a certain threshold (e.g., 10%) is often used to define the effective resolution limit. In the present study, the MTF is used to characterize resolution anisotropy and to compare performance in horizontal and vertical directions of the imaging system.

Experimental Evaluation

To experimentally evaluate the spatial resolution of the imaging setup, a tungsten plate with a sharp edge was positioned in the beam path at a slight angle. Prior to acquisition, the plate was carefully aligned parallel to the source-detector axis to minimize the influence of its thickness on the resulting edge profile.

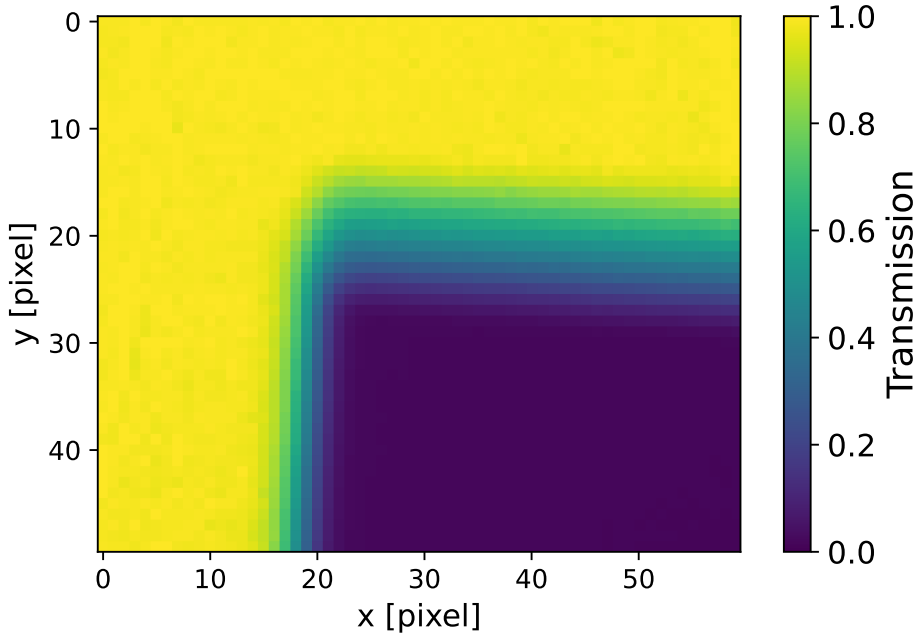

Figure 3.9: Transmission image of the slightly tilted tungsten plate. The edge appears significantly sharper in the horizontal direction due to the anisotropic focal spot geometry. Acquisition parameters: 50 keV, 12 mA, 1000 s exposure time.

The measurement was performed at 50 keV and 12 mA over a total acquisition time of 1000 seconds. The resulting projection image clearly revealed a difference in edge sharpness: the edge appears significantly sharper in the horizontal direction compared to the vertical direction (see Figure 3.9). This anisotropy is caused by the orientation of the X-ray tube's focal spot, which is elongated in the vertical direction.
A further illustrative example of this effect is provided by a test sample featuring an array of circular holes. When imaged, these holes appear elliptical rather than round, with elongation along the vertical axis (see Figure 3.10).
The MTF curves of the detector were determined in both the vertical and horizontal directions using a custom evaluation script based on the Slanted-Edge Method provided by Constantin Rauch [Rau22]. The results are shown in Figure 3.11 and clearly illustrate the directional dependence of the system's spatial resolution. As expected, the horizontal MTF shows a significantly higher cutoff frequency, confirming the superior resolving power in that direction.

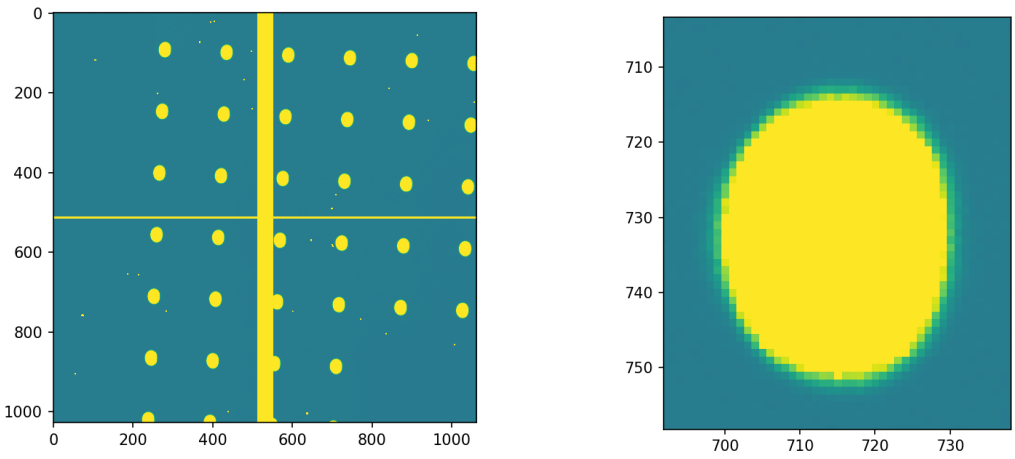

(a) Full view of the hole array

(b) Zoom into a single hole

Figure 3.10: Projection image of a regular hole pattern. The elongation of the holes in vertical direction indicates a resolution limitation due to the focal spot geometry.

Table 3.2 provides a quantitative comparison with established imaging systems. The MTF value of the used source-detector system at 1 lp/mm reaches 0.65 in the horizontal direction, while the vertical direction only achieves 0.11. In contrast, clinical CT systems show a wide range: older systems report values between 0.1 and 0.3 [Tak+15], while more modern systems reach up to 0.95 [Kho+19]. Newer mammography detectors achieve values above 0.8 at 1 lp/mm [Wig+21].
The limiting resolution defined by the 10% MTF threshold is 2.3 lp/mm in the horizontal and 1.1 lp/mm in the vertical direction. This is substantially higher than values from older CT systems (0.7–0.9 lp/mm) [Tak+15] but lower than those from current high-performance CTs (6–8 lp/mm) [Kho+19] and mammography systems (up to 15 lp/mm) [Wig+21].
These results highlight a substantial resolution deficit in the vertical direction, mainly caused by the vertically elongated X-ray focal spot. While the horizontal resolution of the current system approaches older clinical standards at low spatial frequencies, it still falls short of modern high-resolution systems. This anisotropy must be considered in system design and optimization, particularly for applications requiring isotropic spatial resolution, such as the detection of small-scale structures in breast tissue.

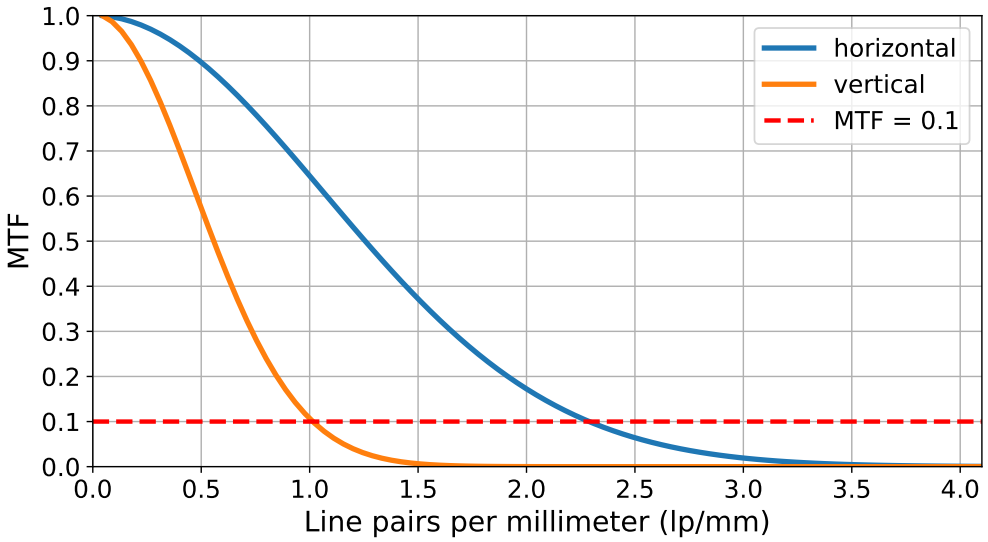

Figure 3.11: Modulation Transfer Function (MTF) in horizontal and vertical direction, derived from the edge response. The horizontal direction shows a significantly higher resolution due to the smaller effective focal spot size. The vertical MTF drops faster, indicating stronger blurring in that direction. The spatial frequency at which the MTF drops to 0.1 is approximately 1 lp/mm for the vertical and 2.3 lp/mm for the horizontal direction.

System	$\mathbf{MTF_{1\,lp/mm}}$	$f_{\mathbf{MFT}0.1}$ (lp/mm)
Clinical CT 2015	0.1 – 0.3	0.7 – 0.9
Clinical CT 2019	0.8 – 0.95	6 – 8
Mammography 2021	0.8 – 0.95	8 – 15
Vertical (this work)	0.11	1.1
Horizontal (this work)	0.65	2.3

Table 3.2: Comparison of MTF values at 1 lp/mm and spatial frequencies at which the MTF drops to 0.1 for various imaging systems. The bottom two rows present the results obtained in this work. Values adapted from: [Tak+15; Kho+19; Wig+21].

3.6 Filter Effects and Quality Maps

To evaluate the influence of an additional spectral filter on the measurement quality, image series were acquired under different conditions. Each dataset consisted of 1000 individual exposures (hereafter referred to as frames), each with an exposure time of 1 second. The X-ray tube was operated at 30 kV and 12 mA and the time between the first and the last frame is approximately 40 minutes.
This acquisition was repeated for threshold settings of 4, 6, 8, and 10 keV, both with and without an H-30 filter (0.5 mm aluminum).
Figure 3.12 illustrates the spectral effect of the H-30 filter. It becomes clear that this filter substantially attenuates low-energy photons, thereby hardening the X-ray spectrum and reducing the overall photon flux, especially below approximately 20 keV. Virtually no photons remain below 9 keV, and the spectral distribution reaches its maximum around 20 keV.
Initially, the influence of changes in the spectrum and intensity of the incident radiation on the detector signal formation is investigated. Subsequently, an approach for quantifying the quality of individual pixels and regions of the detector is developed.

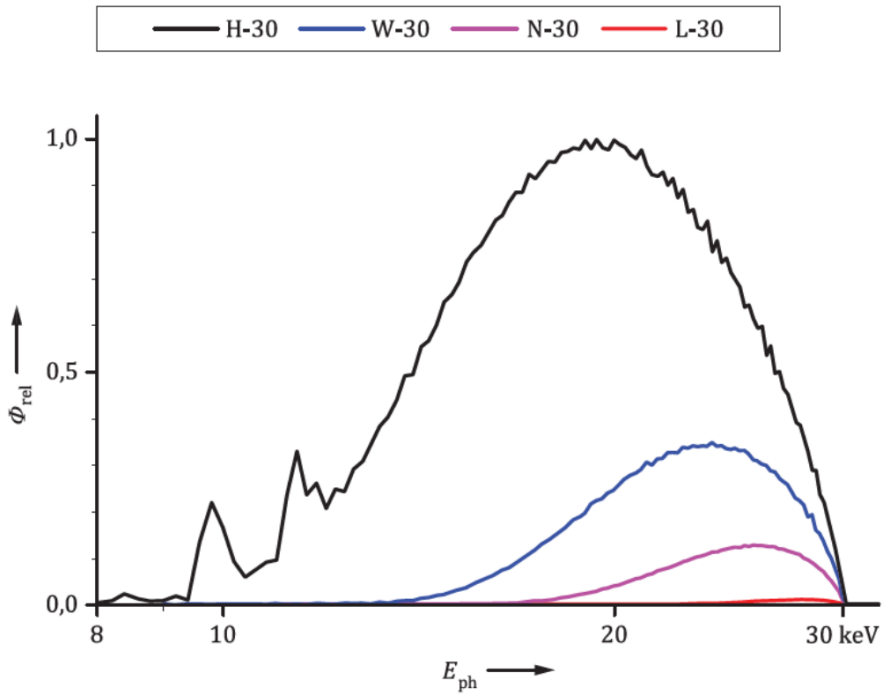

Figure 3.12: Relative spectral distribution ϕ_{rel} of different filters at 30 kV tube voltage. The H-30 filter (black line) significantly reduces the number of low-energy photons. Image source: [Bar+20].

Filter Effects

Considering the absolute number of detected photons for a single pixel across the 1000 frames, it was observed that the standard deviations for all thresholds were smaller when the filter was applied. This is mainly due to the overall reduction in detected photon counts caused by the spectral filtering. The following table summarizes the mean and standard deviation of photon counts for one exemplary pixel (200x200) across the different threshold values:

Th.	**Mean ± Std (n.f.)**	**Mean ± Std (H-30)**
4 keV	43756.97 ± 226.23	14139.56 ± 125.26
6 keV	32213.80 ± 188.32	11074.36 ± 105.26
8 keV	24771.48 ± 177.56	10001.71 ± 106.82
10 keV	13508.18 ± 116.75	7064.63 ± 86.54

Table 3.3: Mean and standard deviation of photon counts for pixel 200x200 across the 1000 frames.

The observed standard deviations are very close to (just always slightly above) the values expected from Poisson statistics, which predict a standard deviation of $\sqrt{\text{Mean}}$ for purely photon-limited signals. To enable a more quantitative comparison, signal-to-noise ratios (SNR) were calculated: $\mathbf{SNR} = \frac{\text{Mean}}{\text{Std}}$. These clearly indicate that the SNR values are significantly higher in the case without filter, suggesting better image quality under unfiltered conditions:

Th.	**SNR (n.f.)**	**SNR (H-30)**
4 keV	193.47	112.87
6 keV	171.02	105.22
8 keV	139.51	93.63
10 keV	115.74	81.65

Table 3.4: Signal-to-noise ratios (SNR) for pixel 200x200 across 1000 frames.

Each image in the 1000-frame series was compared to the first one to illustrate the temporal behavior of signal uniformity across frames. Figure 3.13 shows the resulting normalized difference image $(\text{Frame}_{1000} - \text{Frame}_1)/\text{Frame}_1$ for the 4 keV threshold condition, with and without filter. In the unfiltered image, clear structural patterns and detector inhomogeneities become clearly visible, including various streaks likely related to charge trapping or readout effects. In contrast, the filtered image appears overall noisier due to the approximately 40% lower signal-to-noise ratio (SNR), compare Table 3.4. While the general structure of the detector is still visible, fine details and artifacts are less pronounced, likely due to the lower photon count (Table 3.3) and resulting higher statistical noise.

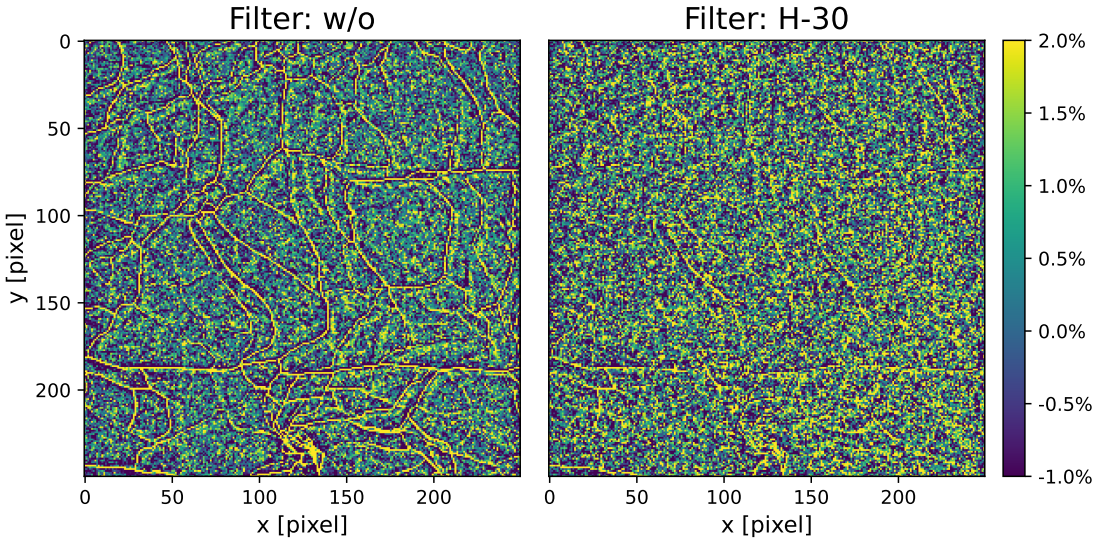

Figure 3.13: Relative change in intensity over time for a zoomed detector region at a threshold of 4 keV. Shown is the normalized difference $(\text{Frame}_{1000} - \text{Frame}_1)/\text{Frame}_1$ in percent, without and with H-30 filter. The visualization highlights local signal changes and defective pixel evolution over approximately 40 minutes.

However, the dynamic appearance of defective pixels (such as detector voids or regions affected by charge trapping) can only be properly observed in the full sequence. In the filtered case, these structures appear much later. This delay is primarily caused by the reduced photon flux due to the filter, which preferentially attenuates low-energy photons (Figure 3.12) and thereby hardens the beam. These low-energy photons are particularly effective at populating charge traps and activating charge-sharing mechanisms, both of which contribute to the development of the observable "streaks" and inhomogeneities over time. With fewer such photons reaching the detector, these effects accumulate more slowly.

Quality Plots

To analyze photon count fluctuations and temporal detector stability, the acquired series of $n = 1000$ frames was evaluated using a method suggested by Prof. Gisela Anton. The concept focuses on assessing whether the statistical variation in the signal of a single pixel is consistent with Poisson expectations, or if additional instability is present. The full dataset is divided into $k = 100$ consecutive subgroups of $m = n/k = 10$ frames each. For each pixel, the signal N_{ij} is the number of counts in frame i of subset j.

The following provides a formal definition of the analysis method using consistent mathematical notation, covering both the subdivision of the dataset and the computation of all relevant statistical quantities:

Subdivision and index mapping: Let $i = 1, \ldots, n$ denote the frame index and $j = 1, \ldots, k$ the index of the subset. The mapping for the i-th frame in the j-th subset is:

$$N_{ij} = N\left(i + m(j-1)\right), \quad i = 1, \ldots, m$$

Subset statistics: For each subset j, three statistical values are computed based on the m individual measurements N_{ij} within that subset:

- **Mean value of subset j:**

$$N_j = \frac{1}{m} \sum_{i=1}^{m} N_{ij} \tag{3.2}$$

  This represents the average photon count of the subset and serves as the basic signal indicator. It is used to assess the temporal evolution of the detector response from one subset to another.

- **Standard deviation within subset j:**

$$\sigma_j = \left(\frac{1}{m-1} \sum_{i=1}^{m} \left(N_{ij} - N_j\right)^2 \right)^{1/2} \tag{3.3}$$

  This quantifies how strongly the individual frames within subset j deviate from their own subset mean. It reflects the local variability or "frame-to-frame" noise within a short time segment.

- **Standard error of the mean for subset j:**

$$\Delta N_j = \frac{\sigma_j}{\sqrt{m}} \tag{3.4}$$

  This expresses the expected uncertainty in the subset mean N_j, assuming purely statistical (Poissonian) fluctuations. It is used as a reference to assess how much the subset means fluctuate beyond what is expected from counting statistics.

Overall metrics: From the k subset means N_j, the overall mean and two derived standard deviations are computed:

$$\overline{N} = \frac{1}{k} \sum_{j=1}^{k} N_j \tag{3.5}$$

$$\sigma_{\text{meas}} = \left(\frac{1}{k-1} \sum_{j=1}^{k} \left(\overline{N} - N_j \right)^2 \right)^{1/2} \tag{3.6}$$

$$\sigma_{\text{exp}} = \frac{1}{k} \sum_{j=1}^{k} \Delta N_j \tag{3.7}$$

Here, σ_{meas} quantifies the measured spread of subset means across the full acquisition, while σ_{exp} represents the average statistical uncertainty expected from photon-counting statistics.

Interpretation and quality metric: The final quality indicator for each pixel is given by the ratio:

$$Q = \frac{\sigma_{\text{meas}}}{\sigma_{\text{exp}}} \tag{3.8}$$

- $Q \approx 1$: the measured fluctuations are consistent with the statistical expectation
- $Q > 1$: the signal varies more strongly than expected $\rightarrow$ potential detector instability or excess noise
- $Q < 1$: the signal is more stable than expected or statistical uncertainty is overestimated

This analysis is performed for each pixel individually, resulting in a so-called "quality map". An example of such a result is shown in Figure 3.14, for both unfiltered and filtered measurements at 4 keV threshold.

Choice of parameters: The number of subsets k should be chosen such that each subset is large enough for stable statistics (i.e., $m = n/k$ not too small), but small enough to allow a meaningful temporal resolution. In our case, $k = 100$ and $m = 10$ were found to provide a good balance.

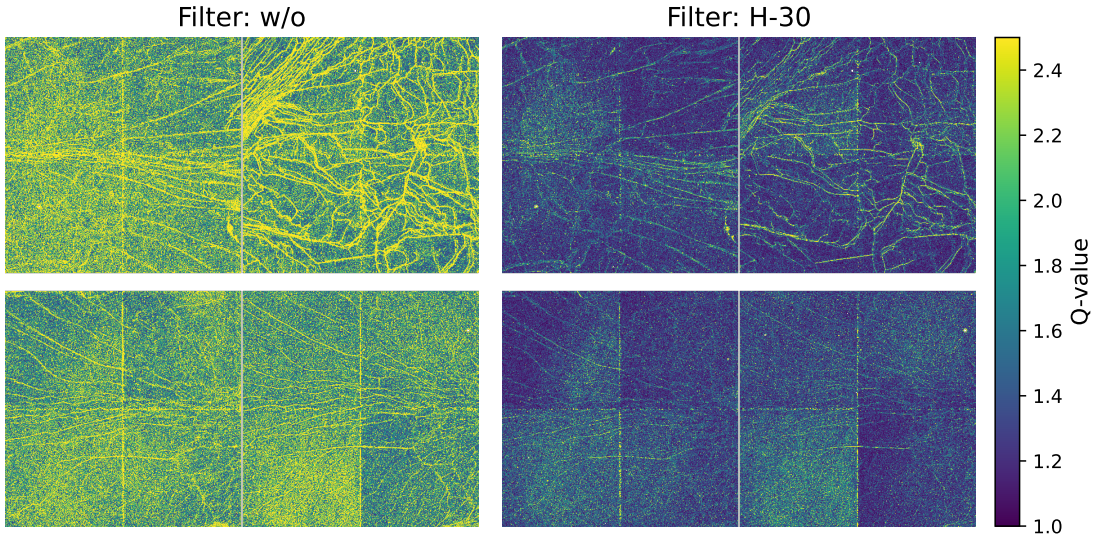

Figure 3.14: Detector-wide maps of the quality metric $Q = \sigma_{\text{meas}}/\sigma_{\text{exp}}$ at a threshold of 4 keV. Left: without filter. Right: with H-30 filter. Pixel values close to 1 indicate purely statistical fluctuations, while larger values highlight unstable or noisy regions.

Analysis of the full-series quality maps

As shown in Figure 3.14, the pixel-wise quality metric $Q = \sigma_{\text{meas}}/\sigma_{\text{exp}}$ was evaluated across the full detector area for the complete 1000-frame acquisition at 4 keV, both with and without H-30 filter. A clear difference in overall levels and spatial distribution is observed.
With filter applied, the Q-values of most pixels remain close to 1, indicating consistency between the measured and expected fluctuations. Only a few structured regions (corresponding to the previously discussed detector streaks and inhomogeneities) exhibit higher values, suggesting localized excess noise or instability.
In contrast, the unfiltered dataset shows significantly elevated Q-values across the entire detector. Most pixels approach values near 2, and those affected by systematic artifacts exceed values of 2. This implies that temporal signal variations are much larger than expected from photon statistics alone, most likely due to detector instabilities and signal buildup effects in the absence of spectral filtering.

Temporal comparison of early and late frames

To further investigate time-dependent effects, the quality maps were computed separately for the first and second halves of the acquisition (frames 1–500 and 501–1000). The corresponding comparison is displayed in Figure 3.15.

For the filtered dataset, both time segments yield almost identical Q-maps, again showing values near 1 except in localized defective areas. This suggests stable and statistically consistent signal quality throughout the measurement.
In contrast, the unfiltered dataset shows a clear temporal evolution. The first 500 frames result in considerably higher Q-values than the second half. This observation indicates an improvement in temporal signal stability over time, with pixel fluctuations decreasing as the measurement progresses. This trend supports the findings discussed in section 3.3, where it was shown that the difference between successive measurements diminishes over time, suggesting that the detector behavior stabilizes.

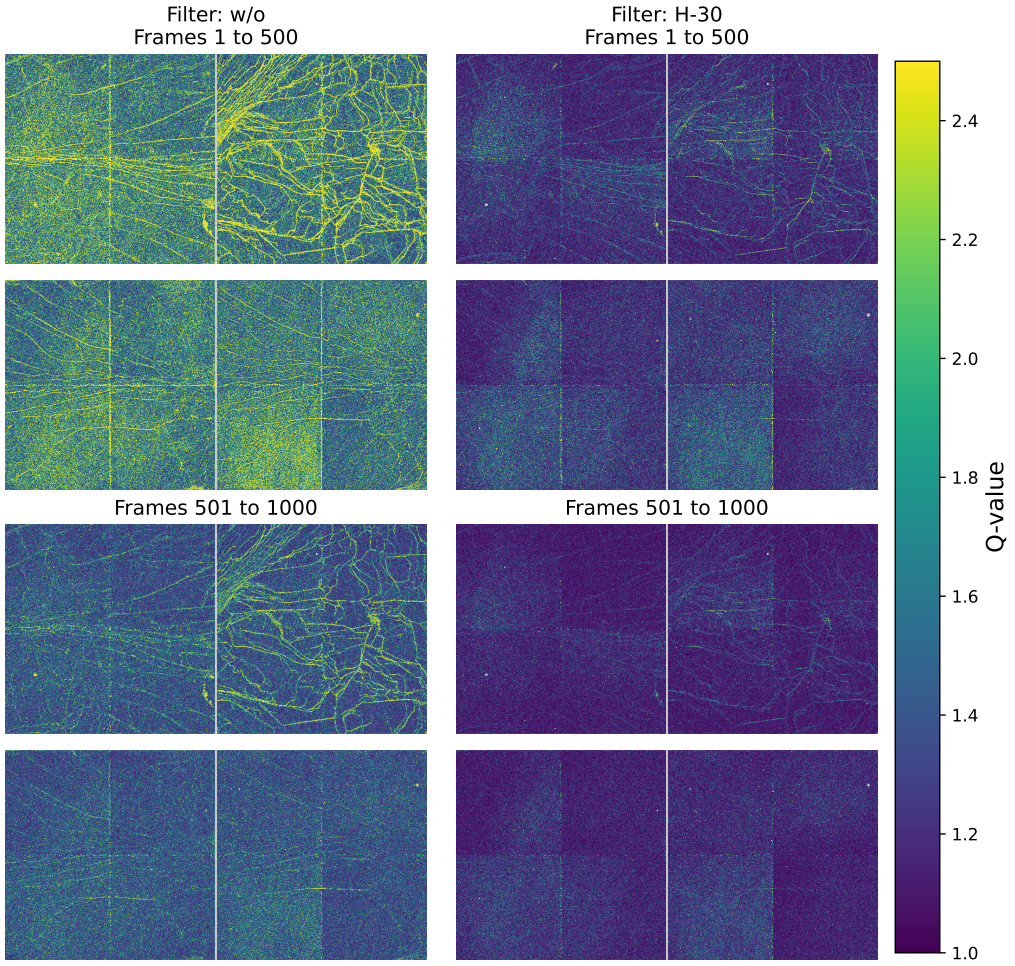

Figure 3.15: Quality maps for early (frames 1 to 500; Top) and late (frames 501 to 1000; Bottom) data. Left: without filter. Right: with H-30 filter. In both settings, the later measurements yield higher Q-values, with a more pronounced improvement observed in the unfiltered configuration.

4 CT Imaging

This chapter presents the preparatory steps and initial results leading up to the implementation of grating-based computed tomography. To ensure high-quality reconstructions, particular attention was first given to detector-related corrections and precise geometric alignment. As described in the previous section, a temporal drift in the detector response was observed; to minimize its impact on image quality, a suitable flat-field correction strategy was developed and applied. In addition, accurate alignment of the X-ray beam with the detector - by centering the rotation axis - was essential for achieving a consistent and symmetric acquisition geometry. These measures established the basis for acquiring the first tomographic datasets using conventional attenuation contrast. While these initial reconstructions did not yet involve gratings, they served as an important benchmark to verify system stability, validate acquisition protocols, and prepare for subsequent dark-field CT measurements.

4.1 Flat-Field Correction Methods

To ensure accurate quantitative imaging in computed tomography, flat-field correction plays a crucial role in compensating for both global and local detector inhomogeneities as well as temporal instabilities of the X-ray source. In this section, we investigate various correction strategies by applying them to a specific dataset and evaluating their effects on the resulting sinograms and reconstructed slices.

Initial Measurement and Observations

The starting point for this evaluation is a CT scan of a test object acquired with the following parameters:

- Full 360° acquisition in 0.25° steps (1440 projections)
- Tube voltage: 45 kV, tube current: 40 mA
- Exposure time: 2 s per projection
- Flat-field acquisition: one before and one after the object scan (each consisting of 10 frames with 2 s exposure)

The scanned object was a single gummy bear, which had been sliced in half along the frontal plane and mounted on a thin plastic film. A small metallic chip was attached behind one of its ears to introduce a high-contrast structure. This setup provided a combination of soft tissue-like material, a thin support, and a sharp high-attenuation feature.
Figure 4.1 shows a representative projection of the object at 0° (left) alongside the extracted sinogram of detector row 300 (right). The gummy bear is clearly visible in the projection (blue), and even the supporting plastic film can be identified as a faint green layer.

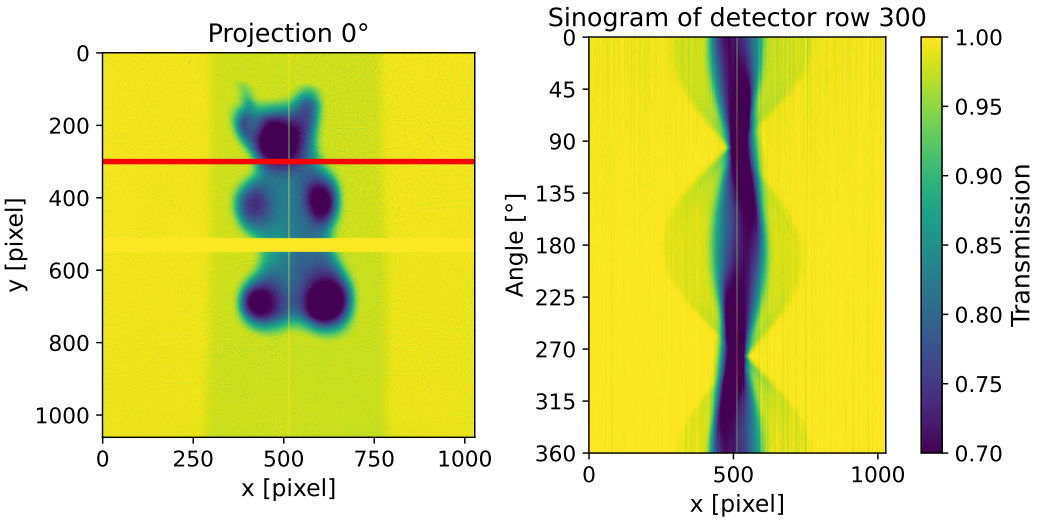

Figure 4.1: Left: projection at 0° showing the frontal-sliced gummy bear (blue) and the supporting plastic film (light green). The metallic chip attached to the gummy bear is visible behind the left ear. Right: sinogram of detector row 300 used throughout this section. The gummy bear and the plastic film appear as sinusoidal patterns.

The flat-field image used for the correction was computed as the mean of the two flat-field stacks (acquired before and after the scan). Transmission images were obtained by dividing each projection by this averaged flat-field image.
To investigate detector-specific effects in more detail, a single detector row (pixel height 300) was extracted from all 1440 projections and used to reconstruct a 2D slice using filtered backprojection. While the exact reconstruction method will be discussed later in section 4.3, this preliminary reconstruction serves to highlight artifact propagation from the sinogram to the image domain.
Figure 4.2 shows the sinogram of detector row 300 (right) with adjusted windowing to emphasize the vertical stripes and global gradient. The left panel shows the

corresponding CT reconstruction, which reveals ring artifacts resulting from the pixel-wise intensity variations visible in the sinogram. This image does not include a colorbar, as it is solely intended to visualize the qualitative appearance of the artifacts.

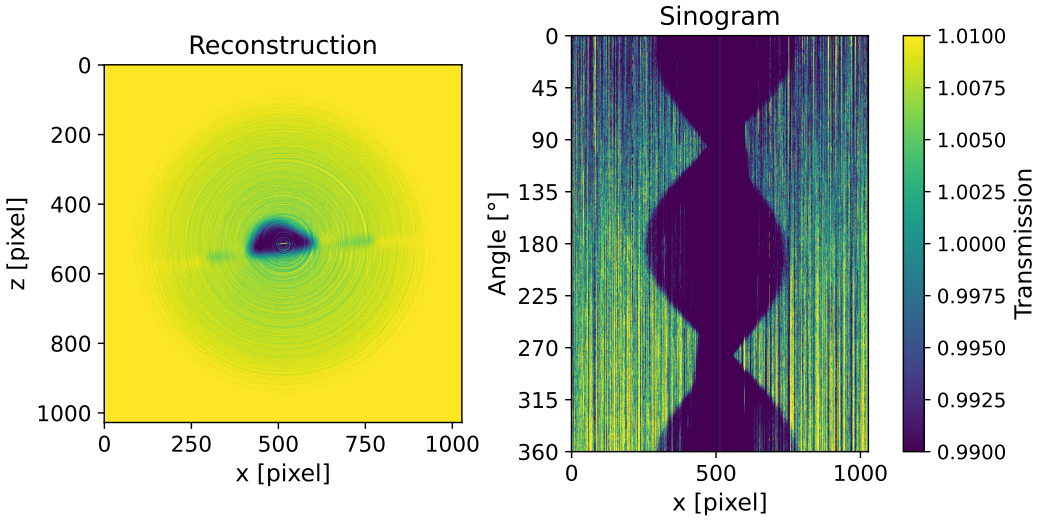

Figure 4.2: Left: Reconstruction from detector row 300. Ring artifacts caused by vertical intensity variations in the sinogram are visible. Right: Sinogram of the same row with adjusted windowing to highlight both the vertical stripes and the global gradient.

Two main artifacts are immediately visible in the sinogram:

1. A global intensity gradient along the projection angle (i.e., time), with increasing transmission values up to values exceeding 1.

2. Vertical stripes indicating pixel-wise differences in detector sensitivity.

The observed global gradient can be attributed to a temporal drift in the detected X-ray intensity, which increases over time. As previously discussed, the mean detector counts show a logarithmic increase as a function of time (cf. Figure 3.6a). This effect directly propagates into the transmission images and leads to angle-dependent overcorrection when using a single static flat-field reference.
The vertical stripes in the sinogram are most likely caused by detector-intrinsic effects such as charge sharing and charge trapping. These effects lead to slight pixel-to-pixel variations in the effective sensitivity, resulting in consistent vertical patterns across all projection angles.

These effects persist in the reconstructed slice, resulting in artificial gradients and ring artifacts that compromise the interpretability and quantitative accuracy of the CT image. In the following subsections, we explore different flat-field correction approaches aimed at mitigating these issues.
In addition to the general artifacts, a prominent vertical line is visible near the centre of the sinogram. This stripe is caused by two dead detector pixels in the central region, the Intra-Module Gap (compare Table 3.1). As a result, a bright spot appears in the corresponding area of the reconstruction. In the more advanced reconstruction pipeline introduced later, these dead pixel columns are interpolated during preprocessing to avoid this artifact.

Averaging Over Multiple Detector Rows

As a first correction strategy, instead of using only detector row 300, a stack of 10 adjacent rows (rows 300 to 309) was averaged. This averaging was applied consistently to both the object projections and the two flat-field stacks, which were subsequently averaged as before to form the reference image.
The effect of this approach is shown in the right panel of Figure 4.3, where the resulting sinogram is displayed as relative deviation from 1 in percent. For comparison, the left panel shows the sinogram based on a single detector row (row 300), using the same visualization settings. While the global intensity gradient along the projection angle remains clearly visible in both cases — highlighting its temporal origin — the vertical stripe pattern is noticeably diminished when averaging over multiple rows. Most of the stripes appear blurred or have vanished completely, and the overall appearance of the sinogram is smoother.
This outcome is in line with expectations: averaging over multiple detector rows reduces the impact of random and small-scale row-specific variations, but does not address time-dependent effects or systematic pixel-level inconsistencies.

Interpolated Flat-Fields

In this approach, instead of using a single averaged flat-field image, a separate virtual flat-field was calculated for each projection. To this end, the two flat-field stacks acquired before and after the object scan were linearly interpolated on a per-pixel basis, resulting in 1440 synthetic flat-field images. Each projection was then normalized by its corresponding interpolated flat-field to calculate the transmission image.
Figure 4.4 shows the resulting sinograms using this method. The left panel corresponds to the case where only detector row 300 was used, while the right panel shows the result after averaging over rows 300 to 309. In both cases, the global gradient that was previously observed has effectively disappeared, confirming that

the temporal evolution of the X-ray intensity can be compensated by interpolation. This highlights the strength of time-resolved reference adaptation.
However, vertical stripes caused by pixel-wise detector inhomogeneities remain clearly visible in the single-row case. These artifacts are again reduced when spatial averaging is applied across multiple rows.
Overall, this result demonstrates that linear interpolation between pre- and post-scan flat-fields can approximate the real temporal evolution of the flat-field quite well. While the underlying intensity drift follows a logarithmic rather than a linear trend, the linear interpolation already provides a reasonable and effective correction in practice.

ROI-Based Gain Correction

In this method, each of the 1440 object projections was divided by the flat-field image acquired before the object scan. To account for temporal changes in intensity, a global correction factor was applied per projection. This factor was computed as the ratio of the mean photon counts within a fixed region of interest (ROI) of 200×200 pixels in the flat-field image to the corresponding ROI in each object projection. The ROI was chosen such that it contained only air in all projections to avoid object influence.
Figure 4.5 shows the resulting sinograms for the correction applied to a single detector row (left) and to the average of rows 300 to 309 (right). As with the interpolation-based approach, the global gradient is effectively removed. The vertical stripe pattern remains in the single-row version and is again reduced through spatial averaging.
A notable difference compared to the linear interpolation method is a generally darker appearance of the sinogram. The transmission values in object-free regions are slightly lower across all 1440 projections. This effect likely stems from minor inconsistencies in the ROI gain normalization but is uniform in nature and does not reintroduce angular/ temporal dependence.

Time-Resolved Flat-Field Acquisition

In this final approach, a new scan was performed in which flat-field images were acquired repeatedly during the measurement. Specifically, after every 20° of object rotation, a flat-field projection without the object was recorded. The full scan covered 360° in steps of 0.5°, resulting in 720 object projections and 18 interleaved flat-field measurements.
Each object projection was then divided by the flat-field image that was acquired closest in time. The resulting sinograms are shown in Figure 4.6, comparing the single-row case (left) to the average over 10 rows (right).

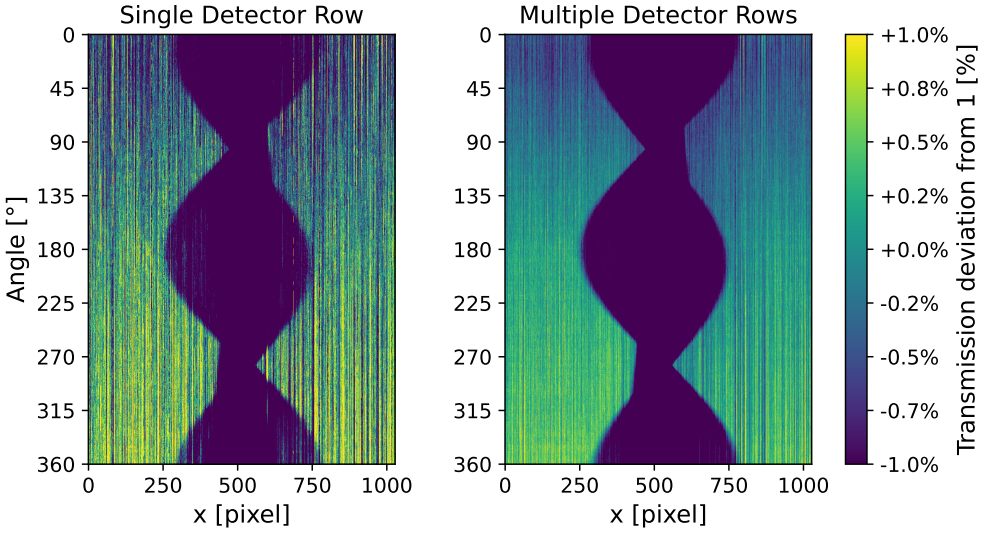

Figure 4.3: Comparison of flat-field correction using a single detector row (left) versus averaging over rows 300 to 309 (right). Both sinograms are displayed as relative deviation from 1 in percent. The global gradient remains clearly visible in both cases, but the vertical artifacts appear smoother and less pronounced after row averaging.

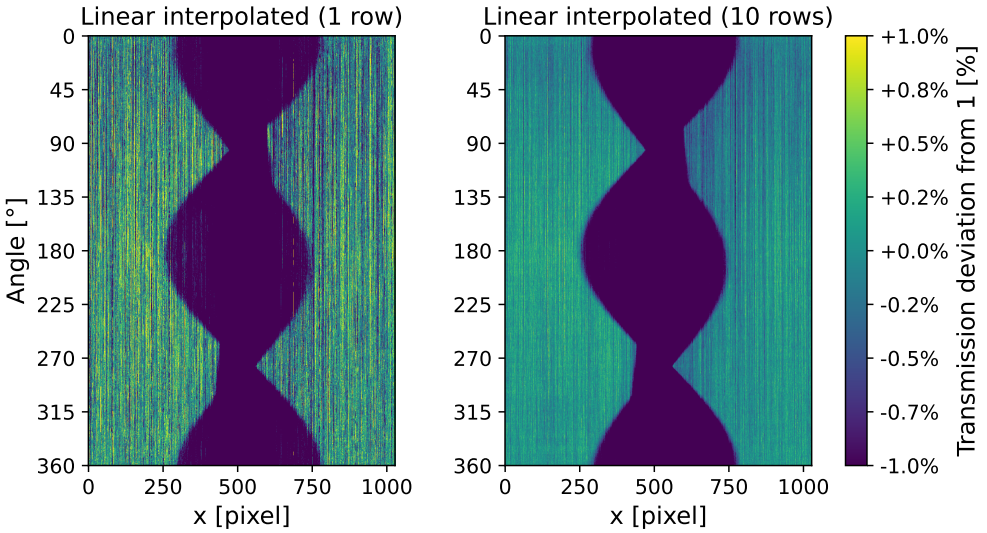

Figure 4.4: Comparison of linearly interpolated flat-field correction applied to a single detector row (left) versus averaging over rows 300 to 309 (right). Both sinograms are displayed as relative deviation from 1 in percent. The temporal gradient is successfully removed in both cases, while vertical artifacts are reduced by row averaging.

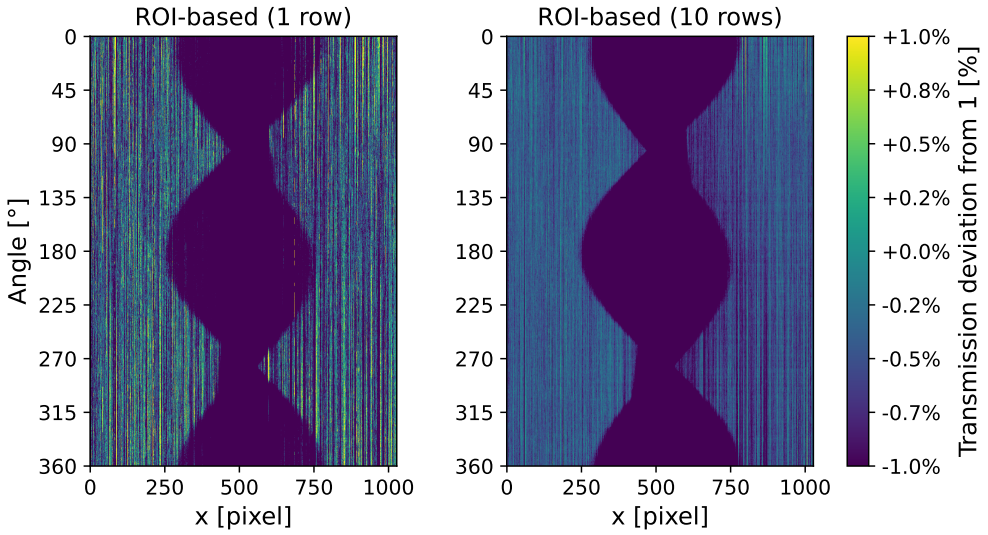

Figure 4.5: Comparison of ROI-based gain correction applied to a single detector row (left) versus averaging over rows 300 to 309 (right). Both sinograms are displayed as relative deviation from 1 in percent. The temporal gradient is removed, and a generally darker baseline is visible in both cases.

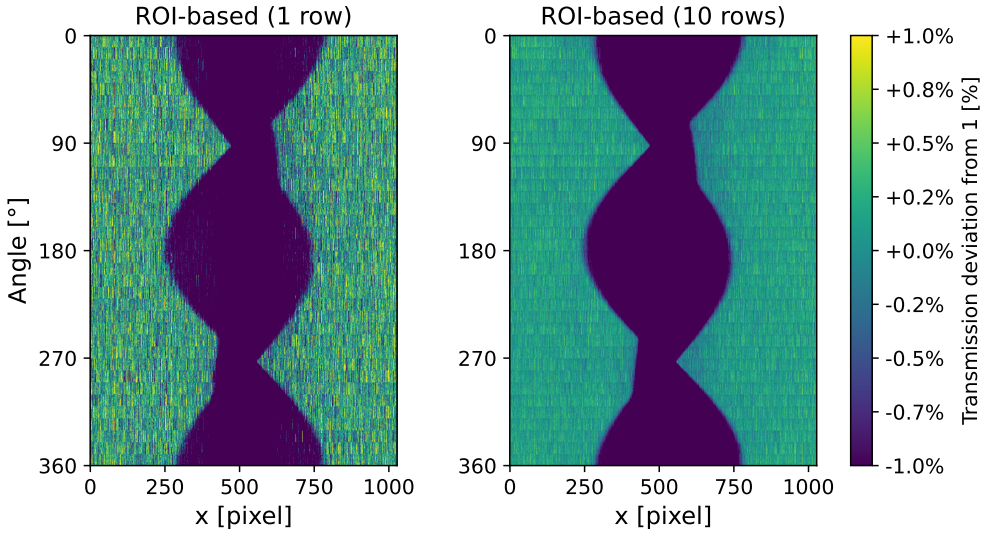

Figure 4.6: Sinograms for time-resolved flat-field acquisition with 18 flat-fields acquired at 20° intervals. Left: single detector row; right: average over rows 300 to 309. The temporal gradient is completely removed, and the background is uniform. Horizontal banding patterns reflect the update intervals of the flat-fields.

In contrast to previous methods, no global temporal gradient is visible, and the background appears uniformly around 1 with minimal deviation. This confirms the effectiveness of frequent flat-field updates in compensating for time-dependent variations.
Interestingly, this method introduces a new type of artifact: distinct horizontal bands are visible in the sinograms, corresponding to the 18 flat-field segments. Within each band, the same vertical stripe patterns appear as before. However, these patterns vary between bands, supporting the hypothesis that they originate from detector-related effects such as charge sharing and charge trapping. Whenever a new flat-field image is used, a slightly different vertical structure emerges.

Summary and Conclusion

Among the investigated correction strategies, the time-resolved flat-field acquisition yields results that most closely represent the true temporal behavior of the system. By interleaving dedicated flat-field projections throughout the scan and applying them locally to the nearest object projections, the temporal intensity drift was fully compensated. The resulting sinograms exhibit a homogeneous background centered around a transmission of 1, with minimal fluctuation.
A consistent observation across all methods is the presence of vertical stripe artifacts, which could not be fully eliminated. These originate from intrinsic detector effects such as charge sharing and charge trapping, which cause pixel-wise fluctuations in the measured signal on short timescales. Since these effects vary from pixel to pixel and are not strictly time-dependent, they persist even under optimized correction schemes. However, when using time-resolved flat-fields, their magnitude is sufficiently small to be considered acceptable, especially in light of the fact that no more effective compensation strategy is currently available.
The averaging over multiple detector rows, while useful in this section to better visualize the suppression of pixel-level noise, will not be used in subsequent analysis. This form of spatial smoothing does not reflect the actual imaging scenario and would artificially reduce spatial resolution in the final reconstructions.

4.2 Axis of Rotation Center Alignment

To ensure a precise rotational geometry in our CT setup, we implemented an alignment procedure for the rotation axis relative to the detector plane. For this purpose, three small metallic spheres were attached to a thin plastic rod using a small amount of glue. The spheres were positioned at different vertical heights along the rod. This rod was then fixed into the sample holder, which rotates during scanning, at an angle of approximately 20° from the vertical.
The scans were performed with an X-ray tube voltage of 40 kV and a current of 16 mA. For each alignment measurement, a total of 72 projection images were acquired, each taken after a 5° rotation step. From the acquired projection images, the positions of the spheres were detected using the `center_of_mass` function from the `scipy.ndimage` package, which provided the (x, y) pixel coordinates of the sphere centers for each angle.
To analyze the alignment quality, the detected positions were visualized across all 72 projections. For each sphere, the mean and standard deviation of the vertical position (y) were computed. The horizontal (x) positions were analyzed in a slightly different manner: instead of using absolute values, the mean x position was determined by averaging pairs of opposing projections, such as scan 1 and scan 37 (i.e., 180° apart). This approach reduces the influence of projection distortion and provides a more robust estimate of the axis of rotation's horizontal position in the detector plane. The plotted trajectories (cf. Figure 4.7) illustrate the circular paths of the beads and allow visual assessment of both symmetry and vertical variation. Ideally, if the rotation axis is perfectly aligned perpendicular to the detector plane, all three spheres should yield the same mean x position. Deviations between these values indicate a tilt or misalignment of the rotation axis relative to the detector. The standard deviation of the y values gives insight into the position of the X-ray beam center. A sphere located exactly at the height of the iso-ray (the central ray that hits the detector orthogonally) will exhibit minimal vertical variation during rotation. In contrast, spheres positioned above or below this central beam will show sinusoidal variations in y due to the cone-beam geometry.

Iterative alignment process

This alignment procedure was repeated in four iterations, each time slightly adjusting the detector angle relative to the ground or the distance of object and detector. In each iteration, the mean x positions and their standard deviations for the three spheres were evaluated. When the mean x positions converged for all three spheres, we concluded that the detector was properly aligned with the rotation axis. Table 4.1 summarizes the measured values for all four alignment attempts.

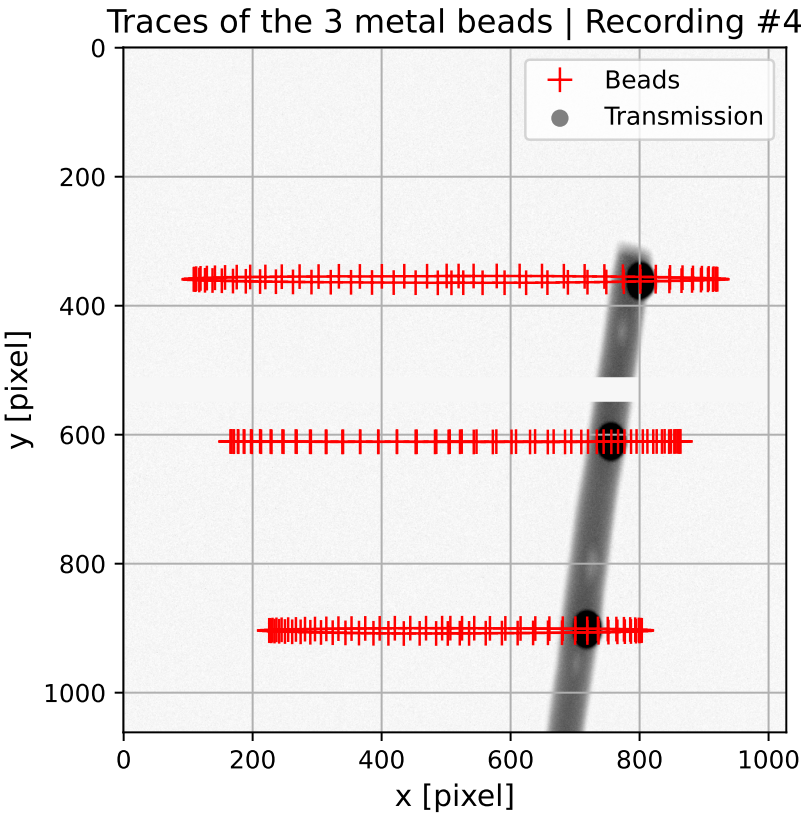

Figure 4.7: Detected trajectories of the three metal beads over 72 projections (Iteration #4). The trace shape provides visual feedback on vertical variation and symmetry, with minimal vertical deviation indicating proximity to the iso-ray.

Iteration	Sphere 1 (top)			Sphere 2 (middle)			Sphere 3 (bottom)		
	μ_x	σ_x	σ_y	μ_x	σ_x	σ_y	μ_x	σ_x	σ_y
1	483.5	5.1	4.1	483.4	3.6	0.96	484.2	2.6	3.9
2	483.8	5.2	4.2	483.5	3.6	0.98	484.2	2.6	3.9
3	485.7	0.7	1.8	485.6	0.5	0.18	485.6	0.4	1.2
4	514.5	2.9	3.6	514.4	2.2	0.28	514.4	1.6	2.8

Table 4.1: Mean x values and standard deviations for the three spheres over four alignment iterations. Values are given in pixels.

Interpretation of results

In the final two iterations, the mean x positions were already well aligned across all three spheres, with only minor deviations on the order of 0.1 pixels. This indicates a successful alignment of the detector with the rotation axis. Notably, the σ_x values in iteration 3 were significantly lower than in iteration 4. This is attributed to a reduced tilt angle of the plastic rod, which caused the projected bead positions to vary less horizontally.
While iteration 3 benefited from this geometrical constraint, the detector angle itself was no longer changed between iterations 3 and 4. Instead, only the sample-to-detector distance was modified. Consequently, both iterations are expected to yield equivalent results in terms of alignment quality for the subsequent CT measurements, as the detector angle remained unchanged. Only the tilt of the rod and the sample-to-detector distance were varied, which do not affect the actual alignment between the rotation axis and the detector.
At the same time, the standard deviation of the vertical position (σ_y) for the middle sphere reached a minimum in iteration 3, indicating that this sphere was located closest to the iso-ray (the central ray orthogonal to the detector plane). This suggests that the iso-center intersects the object plane roughly in the upper third of the detector height. This information is particularly relevant for the grating-based imaging setup, as the G1 grating used in the system has a limited vertical extent. Knowing the iso-center position therefore facilitates optimal placement of both the object and the gratings to ensure high image quality and minimal artifacts.

4.3 Reconstruction Workflow and Visualization

This section introduces the general CT imaging workflow, including data acquisition, attenuation image formation, slice-wise reconstruction, and 3D visualization. To establish and verify this workflow, a simplified setup without interferometric gratings was used. The focus lies on attenuation-based imaging as a baseline reference before introducing the grating-based interferometric setup, adding the dark-field signal in the following chapter.
To perform this preliminary CT scan, the X-ray tube operated at 40 kV and 15 mA, filtered with an H-30 filter. Images were acquired with two energy thresholds: Th1 = 4+ keV and Th2 = 10+ keV, with an exposure time of 1 second per projection. A total of 720 projections were acquired over a full rotation of 360°, corresponding to angular steps of 0.5°. Flat-field images were taken every 10° for correction purposes. The source-to-object-axis distance was 45 cm, and the object-axis-to-detector distance was 90 cm.
The object under investigation was a halved gummy bear, fixed in the frontal plane on a plastic foil. Behind its right ear, a curved metal chip was inserted, and a thin wooden chip was placed behind its right foot to test the detectability of different materials with varying attenuation properties.

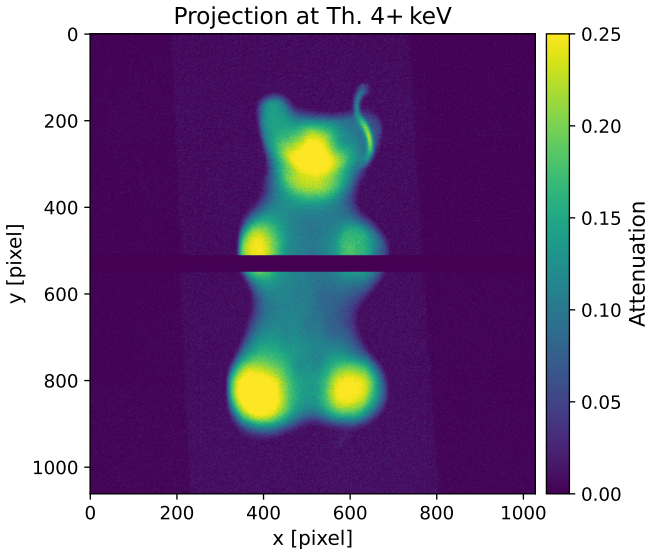

Figure 4.8: Attenuation image of the gummy bear acquired at Th1 = 4+ keV. The structural features of the gummy bear such as head, hands, and feet appear with higher attenuation due to increased thickness. The curved metal chip behind the right ear is distinctly visible.

Projection Image Formation and Corrections

Projection images were converted into attenuation images using the standard logarithmic relation $-\ln(I/I_0)$, where I is the object image and I_0 the closest flat-field image in time. The vertical intra-module gaps (2 pixels wide) were interpolated horizontally using adjacent pixels in each detector row. The large horizontal inter-module gap of 38 pixels in vertical width in the detector center was neither interpolated nor cropped, in order to preserve spatial accuracy.
Figure 4.8 shows a sample attenuation image at Th1 = 4+ keV. The gummy bear's structure is clearly visible, with higher attenuation at thicker regions such as its hands, feet, and facial features. The curved metal chip behind the ear is distinctly recognizable. With careful windowing and zooming, even the mouth and eyes can be distinguished, as well as hints of the wooden chip behind the foot.
A comparison with the projection acquired at Th2 = 10+ keV is shown in Figure 4.9. While the visual differences are minor, the subtraction image reveals relative attenuation differences of up to 2%, depending on the object thickness and material (e.g., metal chip). This is partly due to the spectral shaping by the H-30 filter, which significantly suppresses low-energy photons below 10 keV and thus reduces the effective difference between the two thresholds (Figure 3.12). Only minor attenuation differences are observed between the two thresholds in soft materials, with increased contrast appearing mainly in thicker regions and in high-Z inclusions such as the metal chip.

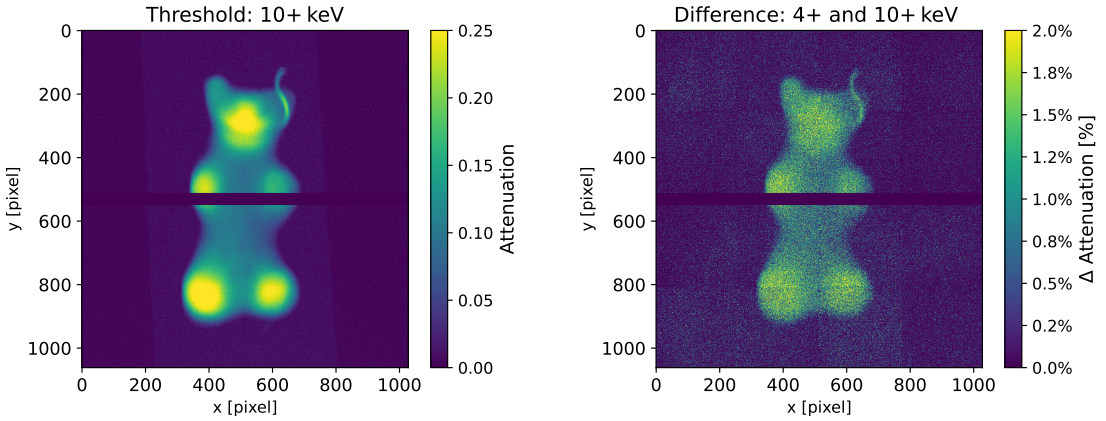

Figure 4.9: Left: Attenuation image of the gummy bear acquired at Th2 = 10+ keV, showing similar overall contrast as in the 4+ keV image. Right: Pixel-wise difference between the attenuation images at 4+ keV and 10+ keV. The relative differences reach up to 2% and correlate with material thickness and composition, particularly in regions with the metal chip.

CT Reconstruction Procedure

CT reconstruction was performed using the attenuation images at 4+ keV. For each detector row, a sinogram was created across all 720 projection angles, covering a full 360° rotation, and subsequently reconstructed into a single CT slice.
The reconstruction was carried out using the ASTRA Toolbox, a flexible and GPU-accelerated software package for tomographic reconstruction [Aar+16; Aar+15; PBS11]. To simplify the setup, a parallel-beam geometry was assumed. The projection geometry was defined by specifying the number of detector pixels per row, the number of projections, and the angular spacing between them. In addition, the volume geometry - defining the spatial extent and resolution of the reconstruction volume - was set accordingly to match the detector configuration and field of view.
The GPU-based algorithm `FBP_CUDA`, a CUDA-accelerated implementation of filtered backprojection, was selected for the reconstruction. As a filter, a Ram-Lak filter was used, as previously described in the theoretical section. This combination allows efficient and accurate slice-wise reconstruction by leveraging the computing power of modern graphics processors.
Figure 4.10 shows a representative example of a reconstructed slice for detector row 250. The corresponding sinogram (left) exhibits the curved sinusoidal pattern of the metal chip near the gummy bear's head. In the reconstructed slice (right), the metal structure appears with strong contrast and spatial separation from the surrounding soft material.

Image Conversion and 3D Rendering

The reconstructed slices were normalized from a Γ window range of 0 to 0.005, mapped to a scale from 0 to 1, then multiplied by 65535 to match the 16-bit grayscale format. The resulting images were saved as individual `.tiff` slices.
For 3D visualization, the software *Dragonfly 3D World* by Comet [Com24] was used, which is available for non-commercial use. After importing the `.tiff` images and defining the voxel size (0.075 mm in all dimensions), the object was visualized in three orthogonal planes and as a 3D volume. The software allows easy adjustment of windowing parameters to highlight specific attenuation ranges, making even low-contrast regions visible.
A representative rendering of the reconstructed volume is shown in Figure 4.11, displaying four perspectives of the object, each rotated by 90° around the vertical axis. The gummy bear's head, limbs, and facial features are clearly visible. In particular, the facial structure, including eyes and mouth, can be distinguished with appropriate windowing. In the rear view (bottom-left), the curved metal chip behind the bear's right ear is prominently visible and spatially well separated from

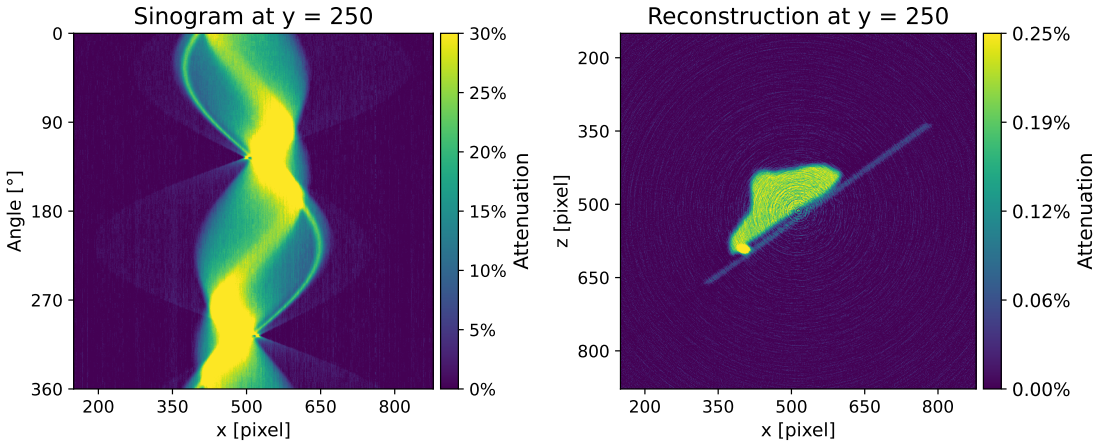

Figure 4.10: Left: Sinogram of detector row 250 across all 720 projection angles. The sinusoidal trace of the curved metal chip is clearly visible as a bright, narrow feature. Right: Corresponding reconstructed slice using filtered backprojection with a Ram-Lak filter. The metal chip appears as a localized high-attenuation region near the head of the gummy bear, clearly distinguishable from the surrounding soft material.

the surrounding material. Additionally, with careful inspection and fine-tuned windowing, the wooden chip behind the right foot becomes faintly discernible. This highlights the ability of the 3D rendering to recover subtle details that are less prominent in individual 2D projections.

Summary and Conclusion

The results demonstrate the successful reconstruction of a volumetric dataset based on attenuation CT. While the metal chip is clearly detected both in 2D projections and 3D volume, the wooden chip proves more challenging due to its low X-ray attenuation. This highlights the limitations of conventional attenuation-based CT in detecting weakly attenuating materials such as wood - an ideal case for complementary imaging via dark-field contrast. In the following chapter, the interferometric setup will be introduced, enabling the acquisition of both attenuation and dark-field signals.

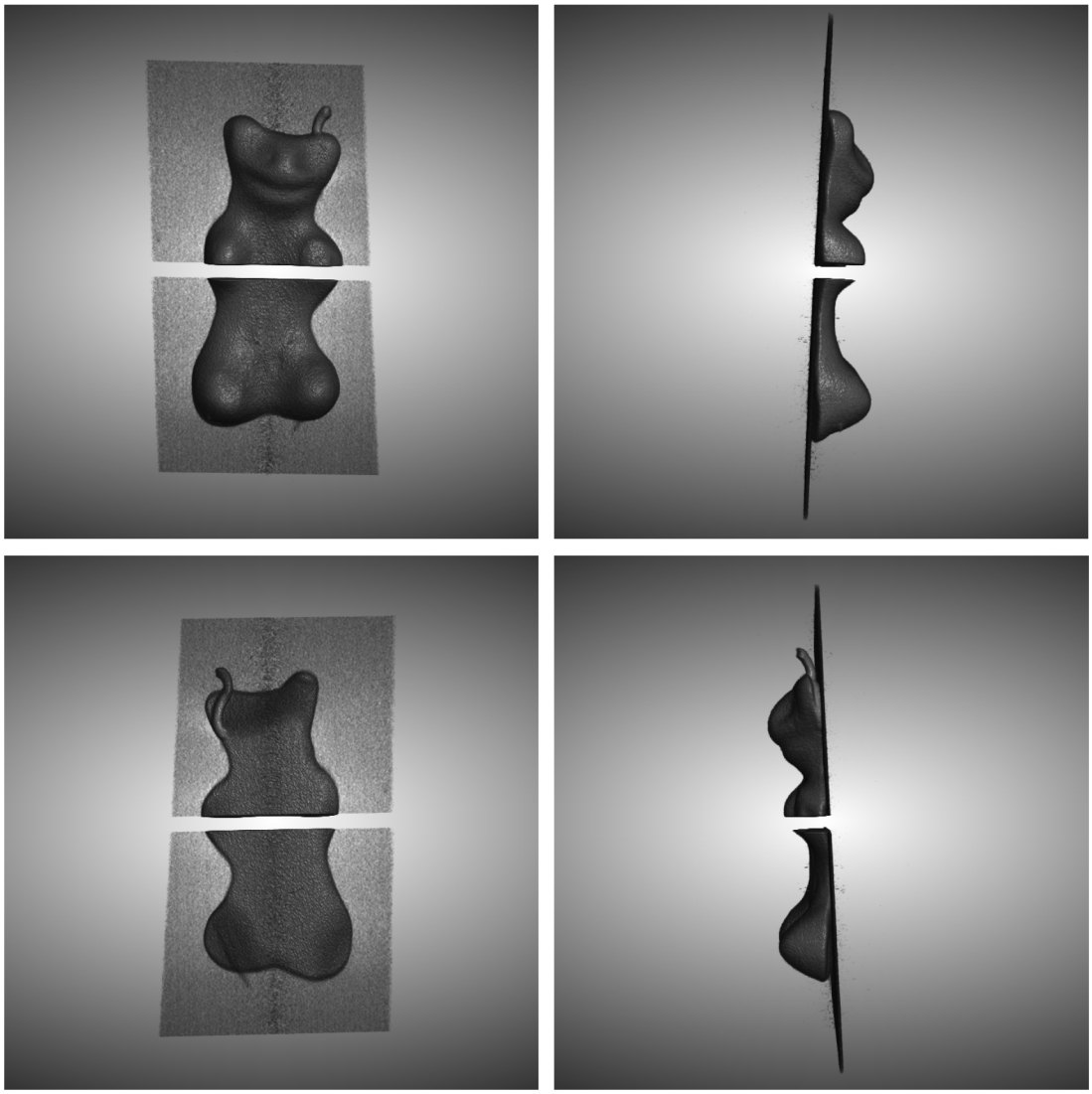

Figure 4.11: 3D rendering of the reconstructed gummy bear volume using Dragonfly. The four views are rotated by 90° around the vertical axis and show the object from different perspectives. The head, limbs, and facial features of the gummy bear are clearly visible, particularly the eyes and mouth with appropriate windowing. From the rear view (bottom-left), the curved metal chip behind the right ear appears prominently. The wooden chip behind the right foot is faintly visible with careful windowing and indicates low attenuation, making it difficult to distinguish in both 2D projections and volume rendering.

5 Grating-Based Dark-Field CT

The previous chapter established a reliable pipeline for conventional attenuation-based CT imaging. Building on this foundation, the present chapter introduces the full grating-based dark-field computed tomography (DFCT) setup. Using a Talbot-Lau interferometer integrated into the CT system, dark-field contrast can now be acquired in addition to conventional attenuation.
Section 5.1 describes the alignment, geometric configuration, and integration of the interferometric gratings into the rotating CT setup. In the subsequent sections, tomographic reconstructions from various sample materials are presented and discussed, highlighting the system's ability to reveal sub-resolution features and illustrating the complementary nature of dark-field contrast.
The aim of this chapter is to demonstrate the feasibility of grating-based DFCT under realistic conditions and to assess its performance on heterogeneous samples. While no actual microcalcifications were imaged, materials such as porcine lung, kidney, and aluminum spheres were selected to emulate relevant scattering features. This work aims to lay the foundation for future DFCT applications, particularly in the detection of microcalcifications in early-stage breast cancer like DCIS.

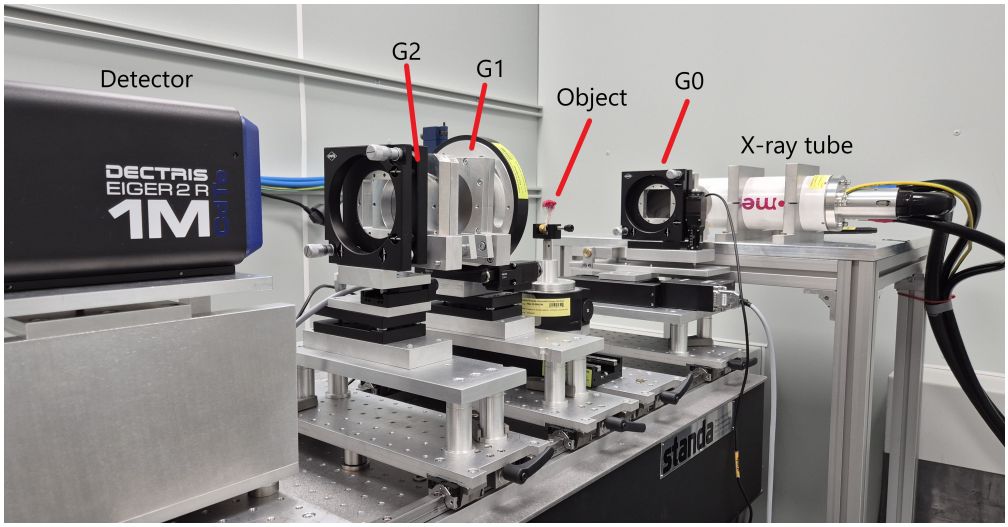

Figure 5.1: Photograph of the Talbot-Lau interferometer setup including X-ray tube, gratings G0, G1, and G2, sample stage, and the detector.

5.1 Grating Alignment and Integration

The system used for subsequent CT acquisitions via phase-stepping technique, enabling both attenuation and dark-field imaging, is depicted in Figure 5.1. It consists of a Talbot-Lau interferometer setup with a microfocus X-ray source (Comet), a photon-counting detector (Dectris Eiger2 R 1M CdTe), and three gratings (G0, G1, G2) mounted on a rail-based optical table. The mechanical components of this setup were designed by Dr. Veronika Ludwig and manufactured by the mechanical workshop of the physics department. The system was assembled by myself in collaboration with my supervisors.
The grating arrangement follows the conventional Talbot-Lau geometry. G0, the source grating, is positioned as close as possible to the X-ray tube. Downstream, the sample is placed between G0 and G1, followed by the phase grating G1, and finally the analyzer grating G2, placed directly in front of the detector. The grating distances were adapted from the Bachelor's thesis of Markus Schneider [Sch20a], maintaining the ratio between G0–G1 and G1–G2 distances while scaling them to match the physical size of the current setup. The resulting distances are approximately 600 mm between G0 and G1, and 59 mm between G1 and G2, giving a total interferometer length of 659 mm.
Each grating is mounted on a dedicated holder that allows for manual tilting via two adjustment screws. The gratings have the following specifications:

- G0: pitch of 24.39 μm
- G1: pitch of 4.37 μm (with π phase shift)
- G2: pitch of 2.4 μm

All gratings have a duty cycle of 0.5. G0 and G2 are large and square-shaped, whereas G1 is a narrow horizontal stripe approximately 2 cm in height. This limited height of G1 defines the vertical field of view of the system, resulting in an effective image region of about 350 pixels in height and 750 pixels in width on the detector.
The initial alignment goal was to achieve a visible and well-formed Moiré pattern at the detector, which is a prerequisite for successful phase-stepping acquisitions. As a first step, G1 was removed and G0 and G2 were aligned for maximum intensity at the detector, ensuring their grating lines were parallel and optimally oriented toward the source and detector, respectively. Due to the cone-beam nature of the setup, G2, being farther from the source, was particularly affected by beam divergence. To compensate for this, G2 was mounted in a slightly curved holder, allowing the X-rays to pass through the grating lines more perpendicularly across the field of view. This design modification significantly increased the overall intensity, turning a narrow vertical intensity band into a more uniform illumination.

Once G0 and G2 were aligned, G1 was inserted at the designated position. A visible Moiré pattern was already observable after the initial placement. Fine-tuning was then performed iteratively, adjusting both tilt and position of G1 in 20–30 iterations until an optimal Moiré pattern was achieved, maximizing fringe period and visibility. The visibility V was roughly estimated after each iteration and optimized accordingly.
Although small variations in setup alignment led to slight differences in the Moiré pattern between scans, all patterns resembled the example shown in the top image of Figure 5.2. The resulting fringe visibility ranged between 10 % and 20 %. A representative visibility map, computed from the phase-stepping curves of each individual pixel, is shown in the lower part of Figure 5.2. The map reveals localized defects corresponding to grating imperfections, yet overall demonstrates a high degree of homogeneity across the usable detector area.

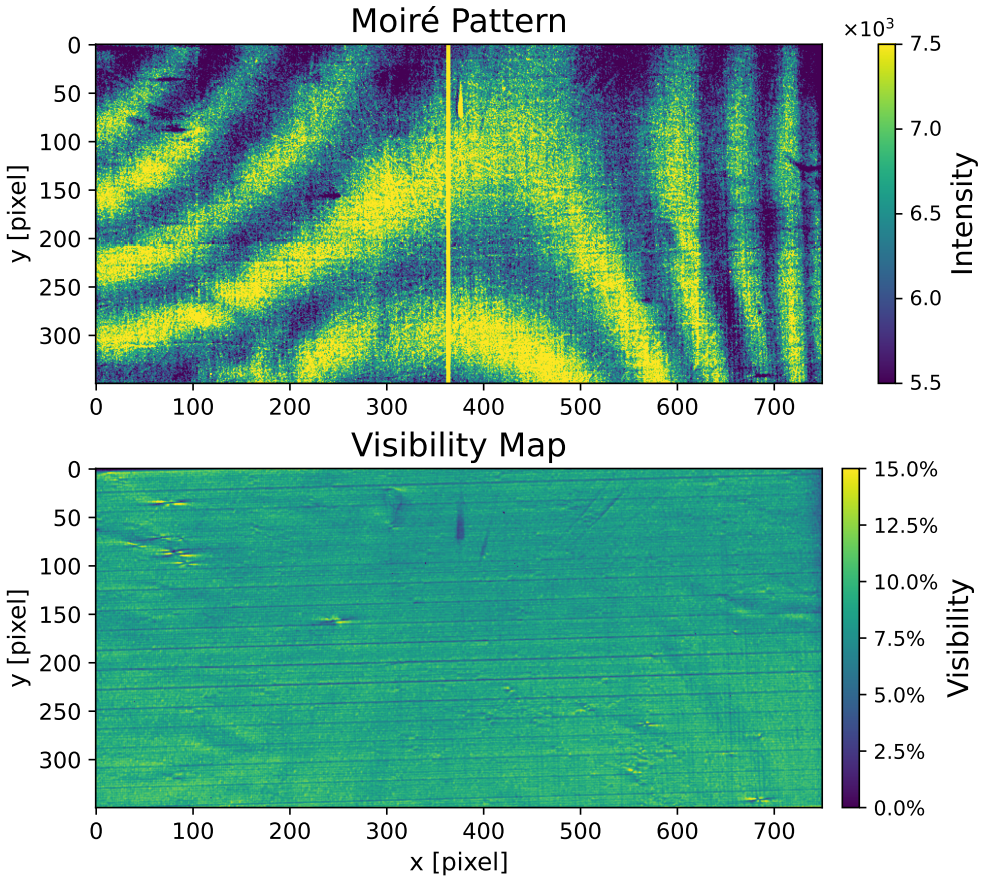

Figure 5.2: Top: Example of a recorded Moiré pattern after successful alignment. Bottom: Pixel-wise visibility map derived from flat-field phase-stepping.

5.2 Acquisition Workflow and Signal Extraction

Compared to the attenuation-only CT measurements described in section 4.3, the integration of the Talbot-Lau interferometer introduces several key modifications to the acquisition workflow. Most notably, the phase-stepping technique is employed to enable the extraction of dark-field and attenuation contrast from each projection. For each CT scan, the source grating G0 was shifted laterally in discrete steps over at least one full grating period (24.39 μm). Two phase-stepping protocols were used: (1) 8 steps with 6 sub-periods (8/6 sampling) and (2) 7 steps with 5 sub-periods (7/5 sampling), the latter offering reduced acquisition time. In both cases, one exposure was acquired per step with an exposure time of 1 s. Consequently, instead of recording a single projection per angle, the system acquired multiple phase steps per angle before rotating to the next position.
All scans were performed over a total angular range of 185°, sampled in steps of 0.5°, resulting in 330 projection angles per scan. The tube voltage was kept constant at 45 kV, while the tube current was initially set to 10 mA and increased to 14 mA in later scans to maximize the photon flux.
Flat-field images were acquired using the time-resolved method described in section 4.1, with one flat-field scan (including full phase-stepping) taken every 30° during the CT acquisition. Each of these flat-fields was processed using the same stepping protocol as the corresponding object scan.

Prior to signal extraction, the vertical intra-module gap in the detector images was interpolated, and all images were cropped to the 350 px × 750 px region covered by the G1 grating, where a well-formed moiré pattern was visible.
For each phase-stepping series, a pixel-wise sinusoidal fit was performed using the custom algorithm developed by Constantin Rauch and Markus Schneider. The fit extracts the mean intensity $\bar{I}$ (offset) and the visibility $V = A/\bar{I}$ for every pixel and for every projection step, separately for object and reference images. Using these values, the attenuation signal Γ and dark-field signal Σ were computed according to the following definitions:

$$\Gamma = -\ln\left(\frac{\bar{I}_{\text{obj}}}{\bar{I}_{\text{ref}}}\right), \qquad \Sigma = -\ln\left(\frac{V_{\text{obj}}}{V_{\text{ref}}}\right). \tag{5.1}$$

This results in one 2D projection image per angle for each signal modality. These projections were subsequently processed using the same filtered backprojection algorithm as described in section 4.3, utilizing the ASTRA Toolbox.
For each sample, both the attenuation and the dark-field datasets were reconstructed slice by slice and exported as 16-bit `.tiff` images. The resulting volumes were visualized and analyzed using Dragonfly, following the same procedure as in the attenuation-only workflow.

5.3 Reconstructed CT Volumes

This final section presents the reconstructed tomographic volumes of various sample materials acquired with the grating-based dark-field CT setup. Each of the following subsections focuses on a specific sample and follows a consistent structure to facilitate comparability and reproducibility.

At the beginning of each subsection, the acquisition process is described, including relevant information about the sample preparation, scanning protocol, and any particular challenges or adjustments required for the measurement. This includes exposure and threshold settings, tube parameters, and details on the phase-stepping configuration used.

Each sample is then visualized in two ways. First, a representative attenuation and dark-field projection is shown as a 2D image, each windowed individually to enhance visual contrast. The colorbar limits were manually selected to optimize contrast across the relevant signal range: minimal and maximal Γ values for attenuation and Σ values for dark-field, respectively.

Second, a volume rendering from four different angles is provided, created in Dragonfly from the reconstructed 3D dataset. To ensure a consistent visual language throughout this section, cyan was used for attenuation and magenta for dark-field renderings across all samples.

Finally, each subsection includes a brief discussion highlighting key observations and structural insights gained from both attenuation and dark-field modalities. Special attention is paid to the visibility of fine structures, scattering effects, and the complementary nature of the two contrast mechanisms.

The following subsections are included in this section:

- **5.3.1 Gummy Bear**:
  A halved gummy bear fixed in frontal plane, containing a small wooden chip near the foot and a metal chip behind the ear.

- **5.3.2 Bacon Stripe**:
  A small piece of supermarket bacon skewered on a toothpick.

- **5.3.3 Pork's lung**:
  A sample of porcine lung tissue mounted on toothpicks for stabilization.

- **5.3.4 Pork's kidney with Aluminum**:
  Two layers of porcine kidney tissue with a thin layer of aluminum powder in between mounted on toothpicks for stabilization.

5.3.1 Gummy Bear

The first sample investigated was a gummy bear, a well-established standard object at our institute due to its soft texture and pronounced attenuation contrast. For this measurement, the gummy bear was horizontally skewered on a toothpick to ensure complete coverage within the grating interferometer's field-of-view, specifically the G1 grating area. A small wooden and a small metallic chip were affixed at its back. The acquisition was carried out using six phase steps within one grating period and a total of eight steps overall. A lower threshold of 10+ keV was selected to suppress low-energy noise while maintaining a reasonable signal level across both contrast channels.

Figure 5.3 shows the attenuation and dark-field projections of the sample. The upper image represents the attenuation signal and clearly outlines the full gummy bear, with the toothpick and body structure well visualized. A careful inspection reveals a subtle structure at about $x = 375$, $y = 225$, which likely corresponds to the metallic chip, although this is difficult to verify solely based on the 2D projection.

In contrast, the lower image shows the corresponding dark-field signal. The toothpick is strongly emphasized, as expected due to its fibrous microstructure causing pronounced small-angle scattering. The gummy bear's contour is faintly visible in the dark-field projection as well: A result of edge scattering phenomena, where interfaces between materials of differing refractive indices (in this case, gummy matrix and air) lead to enhanced scattering. However, neither the wooden nor the metallic chip is distinctly visible in this projection.

A much clearer differentiation is provided by the 3D reconstruction shown in Figure 5.4. The rendering displays four views of the reconstructed volume. The attenuation signal is visualized in cyan and provides a full volumetric representation of the gummy bear. Overlayed in magenta is the dark-field contribution, emphasizing structural contours.

Particularly informative is the lower left view, showing the back of the gummy bear. Here, both the metallic and the wooden chips are distinctly visible: the metallic chip appears as a bright, denser region within the cyan volume (highlighted by the yellow box), while the wooden chip (dark magenta inside the orange box) can also be clearly identified.

This result demonstrates the advantage of full 3D acquisition over 2D projections, especially for small or low-contrast inclusions. It also confirms the expected contrast behavior of the materials: the gummy matrix primarily contributes to the attenuation channel, while the wooden toothpick and structural interfaces generate dark-field signal.

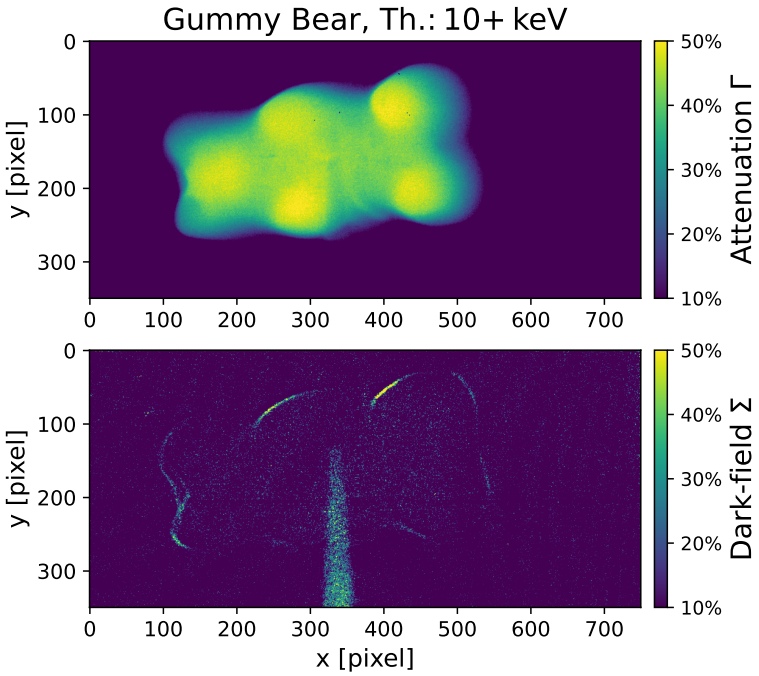

Figure 5.3: Attenuation (top) and dark-field (bottom) projection of the gummy bear sample. The attenuation image shows the full body, while the dark-field highlights the toothpick and contour scattering.

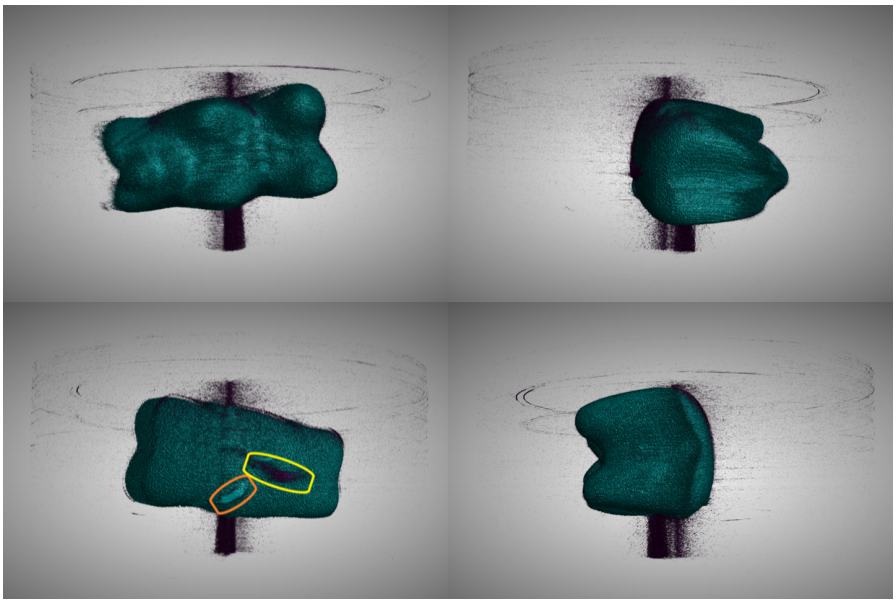

Figure 5.4: 3D rendering of the reconstructed gummy bear. The metal (orange) and wooden (yellow) chips are clearly visible from the back view.

5.3.2 Bacon Stripe

As a second sample, a supermarket bacon stripe of approximately $1 \times 1 \times 2\,\mathrm{cm}^3$ was selected. The sample was skewered lengthwise onto a toothpick. This configuration was chosen to investigate a tissue-like object with layered fat and muscle structures. High attenuation contrast was expected due to the dense composition, and it was hoped that one of the internal layers might generate a measurable dark-field signal. Figure 5.5 presents the attenuation and dark-field projections. The top image displays a well-resolved attenuation profile, with signal values reaching up to $\Gamma = 70\%$, confirming the expected strong absorption. In the lower dark-field image, the toothpick appears prominently, and weak contours of the bacon slice are faintly visible, similar to the edge scattering observed in the gummy bear sample.
This impression is confirmed by the 3D reconstruction shown in Figure 5.6. Four different viewing angles are presented, showing a strong attenuation signal throughout the bacon volume. A narrow magenta streak running along the toothpick corresponds to the dark-field signal, caused by the fibrous wooden structure.
Overall, the results match expectations: the bacon provides a high-quality attenuation signal but lacks strong intrinsic scattering features. Unfortunately, no internal bacon layer was able to generate a significant dark-field response, limiting the modality's ability to resolve internal substructure in this specific sample.

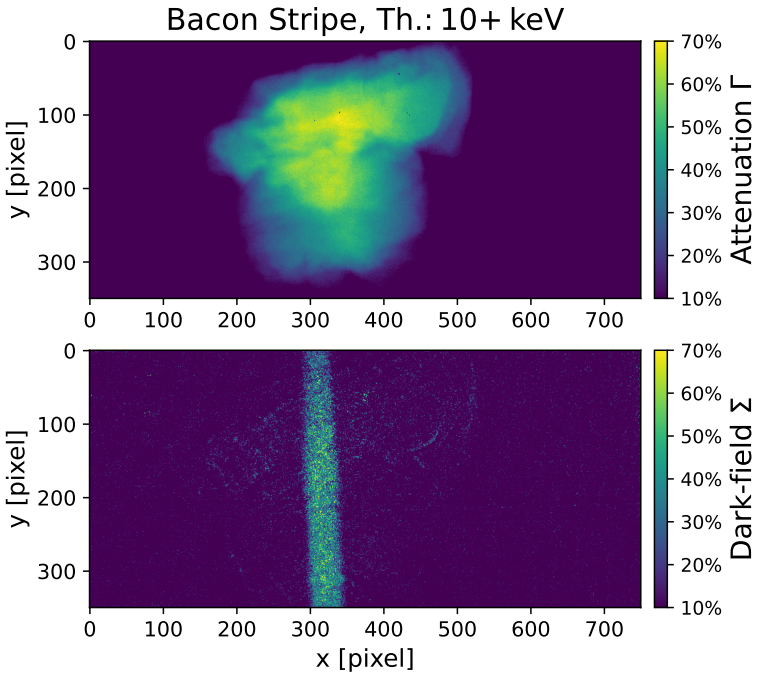

Figure 5.5: Attenuation (top) and dark-field (bottom) projection of the bacon sample. High absorption contrast is visible, with only faint dark-field contour signals.

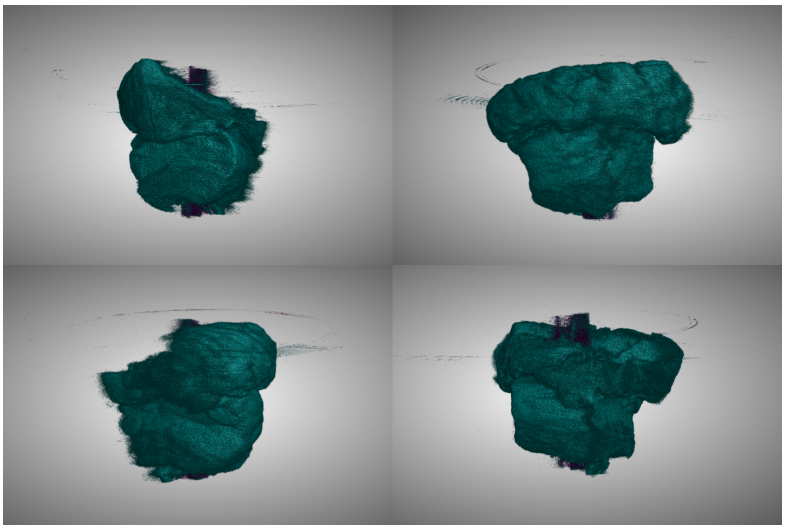

Figure 5.6: 3D rendering of the bacon stripe. The attenuation channel dominates, while the dark-field signal is limited to the toothpick structure.

5.3.3 Pork's lung

A small piece of porcine lung, approximately $1 \times 2 \times 1\,\mathrm{cm}^3$ in size, was extracted from a butcher's specimen and mounted on a toothpick (Figure 5.7, left picture). To slow down dehydration, the sample was wrapped in cling film. Due to the densely packed alveoli in lung tissue, a strong dark-field signal was expected. However, it was unclear whether the signal would still be detectable in non-ventilated, post-mortem tissue.
Figure 5.8 shows the attenuation and dark-field projections. Both contrast mechanisms yield high signal levels of up to Γ and $\Sigma = 70\%$, indicating a well-preserved alveolar structure. A notable feature appears in the attenuation image: two circular regions of increased attenuation - one on the left, one on the right - are mirrored by corresponding reductions in the dark-field image. This suggests localized structural changes, possibly due to compression or cutting artifacts. When compressing the sample manually, small air bubbles were felt escaping, supporting the hypothesis of localized alveolar collapse.
The 3D volume rendering in Figure 5.9 confirms these findings. The cyan attenuation volume is rendered semi-transparent to reveal internal structures. A homogeneous magenta dark-field signal fills the entire lung volume, while the attenuation signal appears more heterogeneous. This contrast between the uniformity of scattering and variability of absorption highlights the complementary nature of both modalities.
Overall, the lung sample fulfilled expectations excellently. It serves as a prime example of biological soft tissue generating a strong dark-field signal. The heterogeneity of the attenuation signal might reflect physiological or pathological variations, which would require medical expertise for further interpretation.

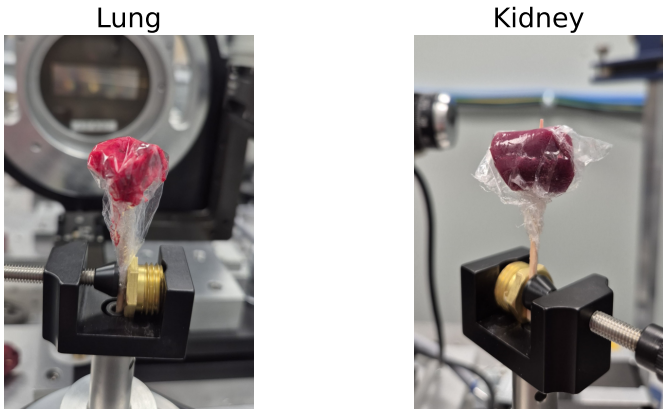

Figure 5.7: Left: porcine lung sample as used in subsection 5.3.3.
Right: porcine kidney sample as used in subsection 5.3.4.

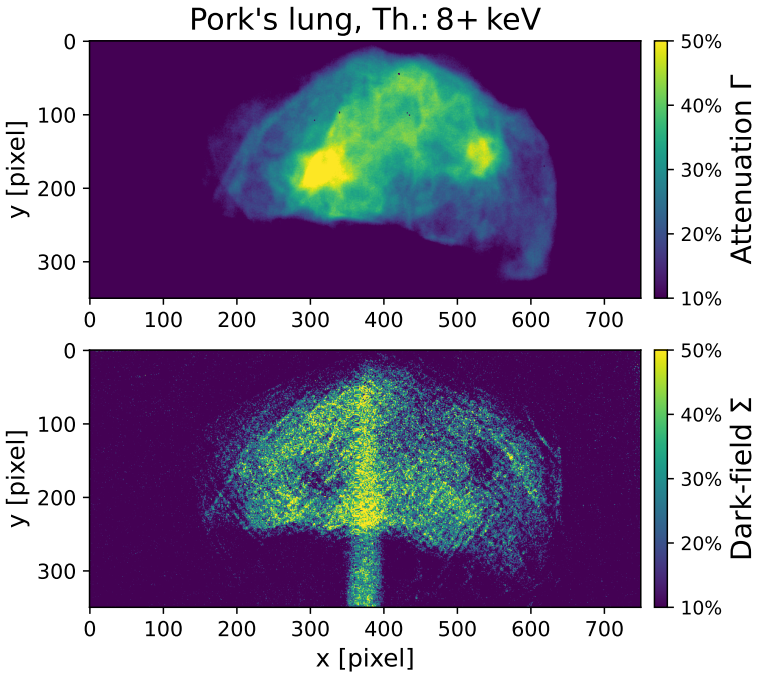

Figure 5.8: Attenuation (top) and dark-field (bottom) projection of the lung sample. Both signals are strong; localized differences indicate potential structural collapse.

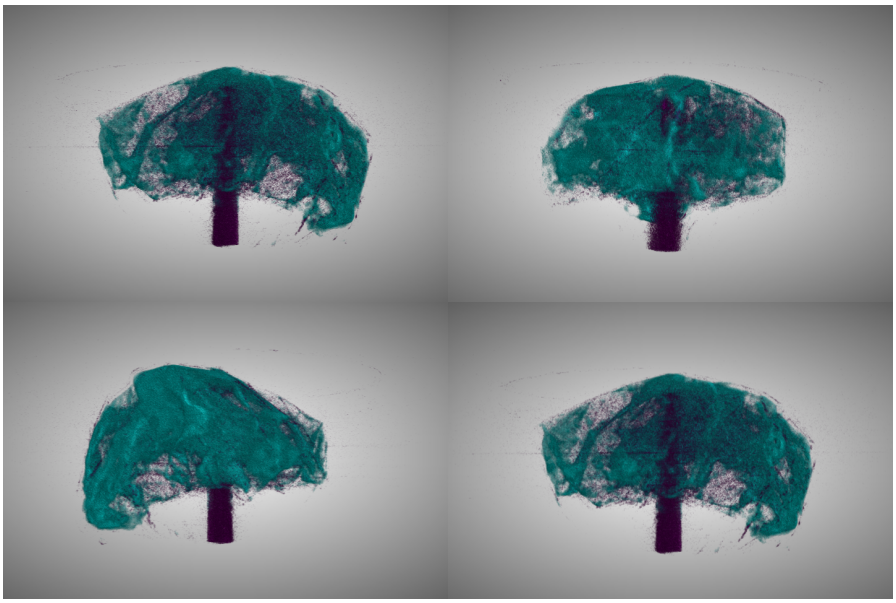

Figure 5.9: 3D rendering of the porcine lung. The attenuation is semi-transparent; the dark-field signal is strong and homogeneously distributed.

5.3.4 Pork's kidney with Aluminum

Based on recommendations from medical professionals at the university hospital's gynecology department, porcine kidney tissue was selected due to its structural similarity to breast tissue. The kidney was found to be highly homogeneous and dense, suggesting strong attenuation but little dark-field signal. To simulate microcalcifications, two flat layers ($\sim 1 \times 1 \times 0.5\,\mathrm{cm}^3$) were prepared with aluminum powder (sub-millimeter spherical particles) placed in between (Figure 5.7, right picture). To reduce acquisition time, only five steps per period and seven total steps were used for this scan.
Figure 5.10 shows the 2D projections. The attenuation image reveals a strong signal with values exceeding $\Gamma = 80\%$, as expected. In the dark-field projection, a highly pronounced band with $\Sigma \approx 80\%$ appears at the location of the aluminum layer - distinctly separating itself from the homogeneous surrounding tissue. While the aluminum can also be faintly seen in the attenuation image, it is much more apparent in the dark-field image without needing intensity window adjustments.
The 3D volume rendering in Figure 5.11 includes three standard views from the sides plus one top-down view (lower right). For this dataset, the attenuation volume (cyan) was windowed to isolate the high-density aluminum regions. The dark-field signal (magenta), however, extends further and reveals more of the aluminum distribution. This is attributed to the fact that dark-field is sensitive to microstructural scattering across the entire powder volume, while attenuation highlights only the densest clumps.
In conclusion, the prepared kidney sample with aluminum powder met all expectations and convincingly demonstrates the advantages of dark-field CT. Future studies could further optimize particle distribution to reduce clumping and maximize the relative contribution of the dark-field signal. Still, the clear separation of aluminum powder from surrounding tissue is an excellent example of dark-field's potential in identifying microcalcifications in soft tissue.

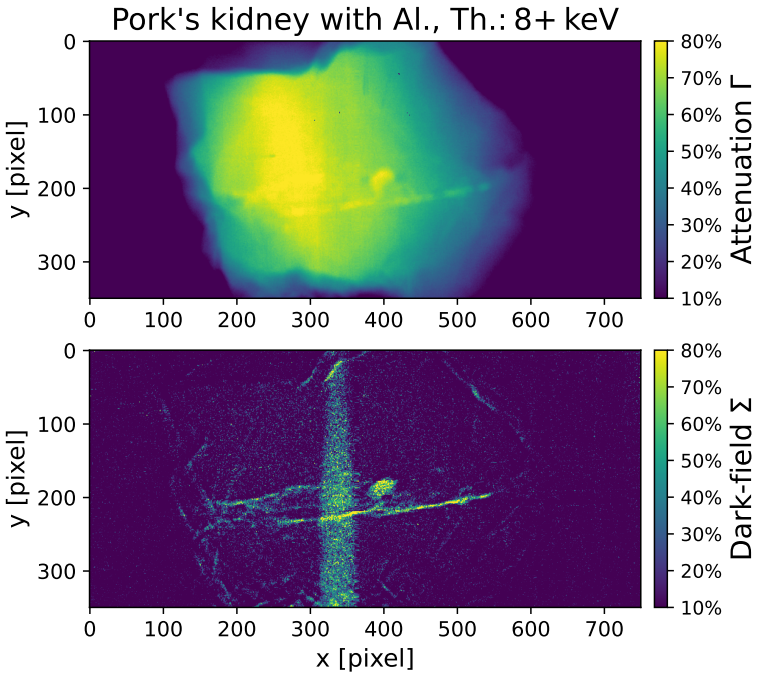

Figure 5.10: Attenuation (top) and dark-field (bottom) projection of the porcine kidney with aluminum powder. The dark-field image reveals the powder layer more clearly.

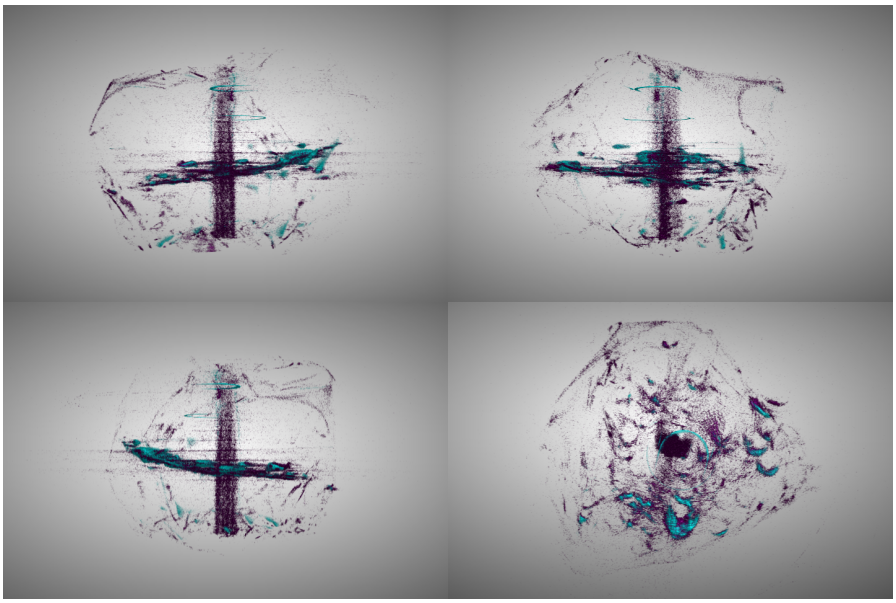

Figure 5.11: 3D rendering of the kidney sample. The dark-field signal covers a larger portion of the aluminum layer compared to attenuation.

6 Conclusion and Outlook

This thesis presents a comprehensive experimental study towards the implementation of grating-based dark-field computed tomography (DFCT), with a particular focus on the characterization of a new photon-counting detector, system integration, and early imaging results on biological samples. The motivation was driven by the limitations of conventional attenuation-based imaging in detecting microstructures such as breast microcalcifications, and the potential of dark-field imaging to overcome these challenges.

Chapter 3 provided an in-depth characterization of the photon-counting detector used in this work. Key findings include a high degree of linearity with respect to tube current, a strong spatial resolution in the horizontal direction, and notable temporal signal drifts over several hours, which could be described and visualized quantitatively. Additional effects such as charge trapping and sharing, especially in CdTe-based sensors, led to the development of customized flat-field correction methods and quality maps. These investigations laid the foundation for accurate signal extraction in later CT acquisitions and highlighted the need for time-resolved calibration to ensure consistent image quality.

Chapter 4, a stable imaging workflow for attenuation-based CT was established and validated using simplified samples without gratings. Several flat-field correction techniques were evaluated, with time-resolved reference acquisition yielding the most robust results. First 3D reconstructions demonstrated good spatial resolution and soft tissue contrast. However, the attenuation-based modality showed clear limitations in resolving low-contrast structures, such as the wooden chip in the gummy bear experiment, confirming the need for complementary imaging signals like the dark-field channel.

Chapter 5 introduced the complete Talbot-Lau interferometric setup and demonstrated the successful acquisition of both attenuation and dark-field signals using a grating-based CT system. The setup was carefully aligned, and visibility maps confirmed the functionality of the interferometer. Reconstructed volumes of porcine lung and kidney samples revealed distinct signal patterns in both modalities: while attenuation provided structural context, the dark-field channel highlighted sub-resolution scattering features. Particularly noteworthy was the aluminum-powder layer embedded in kidney tissue, which appeared much more distinctly in the dark-field volume - illustrating the core benefit of DFCT in detecting microstructural contrast beyond absorption differences.

Outlook

In terms of system performance, the total scan time per DFCT acquisition was successfully reduced to approximately 75 minutes, roughly half the duration of initial experiments. Further reduction appears feasible, for example by acquiring flat-field references every 60° instead of every 30°, as current results show high stability even with fewer calibration frames. This would significantly reduce scan time without compromising image quality, thereby enhancing the system's practicality.
Although DFCT shows promising capabilities, its application as a diagnostic tool for breast cancer remains limited due to the setup dimensions and radiation dose. However, a more realistic clinical vision could be its use during tumor resection procedures in the operating room. Here, dark-field CT could provide immediate feedback on whether the tumor was fully removed or if resection margins remain. This would avoid the need for a second surgery, which currently often occurs about one week after the pathological assessment. For such intraoperative use, scan and reconstruction times below 5 minutes would be essential - still a significant challenge at present. Future research could explore reduced-angle acquisitions, using only 3–5 projections combined with manual or algorithmic triangulation to localize microcalcifications. According to expert feedback from the university hospital, such sparse imaging might already provide sufficient guidance in clinical workflows.
In conclusion, this thesis lays the experimental and technical groundwork for grating-based DFCT with photon-counting detectors. The system achieves both attenuation and dark-field imaging in 3D and demonstrates strong contrast sensitivity for microstructures. While clinical implementation still requires major advances in speed and system integration, the results illustrate DFCT's potential to provide new diagnostic insights beyond conventional CT.

Bibliography

[Aar+15] W. van Aarle, W. J. Palenstijn, J. De Beenhouwer, T. Altantzis, et al. "The ASTRA Toolbox: A platform for advanced algorithm development in electron tomography". In: *Ultramicroscopy* 157 (2015), pp. 35–47. DOI: 10.1016/j.ultramic.2015.05.002.

[Aar+16] W. van Aarle, W. J. Palenstijn, J. Cant, E. Janssens, et al. "Fast and Flexible X-ray Tomography Using the ASTRA Toolbox". In: *Optics Express* 24.22 (2016), pp. 25129–25147. DOI: 10.1364/OE.24.025129.

[AME17] Boudjelal Abdelwahhab, Z. Messali, and Abderrahim Elmoataz. "A Novel Kernel-Based RegularizationTechnique for PET Image Reconstruction". In: *Technologies* 5 (June 2017), p. 37. DOI: 10.3390/technologies5020037.

[Ami09] Isaac Amidror. *The Theory of the Moiré Phenomenon*. Berlin, Heidelberg: Springer-Verlag, 2009. ISBN: 9781848821811.

[Ant+13] Gisela Anton, Florian Bayer, Matthias W. Beckmann, Jürgen Durst, et al. "Grating-based darkfield imaging of human breast tissue". In: *Zeitschrift für Medizinische Physik* 23.4 (2013), pp. 228–235. DOI: 10.1016/j.zemedi.2013.01.001.

[Auw+14] Sigrid Auweter, Julia Herzen, Marian Willner, Susanne Grandl, et al. "X-ray phase-contrast imaging of the breast - Advances towards clinical implementation". In: *The British journal of radiology* 87 (Feb. 2014). DOI: 10.1259/bjr.20130606.

[Bar+20] Stephen G. R. Barnard, Elizabeth A. Ainsbury, Tim Daniels, Jonathan Eakins, et al. *Alternatives to Caesium Irradiators for Biological Sciences Research and Blood Transfusion Services*. Technical Report CRCE-RED-001-2020. Prepared for the UK Home Office. Public Health England, Centre for Radiation, Chemical and Environmental Hazards, Sept. 2020. URL: https://www.ukhsa-protectionservices.org.uk/cms/assets/gfx/content/resource_4633cs96c974552b.pdf (visited on 04/07/2025).

[Bec+10] M Bech, O Bunk, T Donath, R Feidenhans'l, et al. "Quantitative x-ray dark-field computed tomography". In: *Physics in Medicine and Biology* 55.18 (Sept. 21, 2010), pp. 5529–5539. ISSN: 0031-9155, 1361-6560. DOI: 10.1088/0031-9155/55/18/017.

[BS22] Julien Bert and David Sarrut. "Monte Carlo simulations for medical and biomedical applications". In: *Biomedical Image Synthesis and Simulation*. Elsevier, 2022, pp. 23–53. ISBN: 978-0-12-824349-7. DOI: 10.1016/B978-0-12-824349-7.00010-4.

[Com24] Comet Technologies. *Dragonfly 3D World*. 2024. URL: https://dragonfly.comet.tech/en/products/dragonfly-3d-world (visited on 04/07/2025).

[DEC24a] DECTRIS Ltd. *DECTRIS EIGER2 User Manual*. Document version v1.8.2. 2024. URL: https://media.dectris.com/filer_public/30/14/3014704e-5f3b-43ba-8ccf-8ef720e60d2a/240202_usermanual_eiger2.pdf.

[DEC24b] DECTRIS Ltd. *Technical Specifications: EIGER2 R CdTe 1M*. Document version v1.8.3. 2024. URL: https://media.dectris.com/filer_public/12/b6/12b61f47-fd77-40d0-a0ab-50ecbbfdd14d/technicalspecifications_eiger2_r_cdte_1m_v183.pdf.

[DEC25] DECTRIS Ltd. *EIGER2 R CdTe 1M Hybrid Photon Counting Detector*. Accessed: 2025-04-21. 2025. URL: https://www.dectris.com/products/eiger2-r/eiger2-r-cdte-1m/.

[Del+09] S. Del Sordo, L. Abbene, E. Caroli, A. M. Mancini, et al. "Progress in the Development of CdTe and CdZnTe Semiconductor Detectors for X-ray and Gamma Ray Imaging and Spectroscopy". In: *Sensors* 9.5 (2009), pp. 3491–3526. DOI: 10.3390/s90503491.

[Dem16] Wolfgang Demtröder. *Experimentalphysik 3*. Springer-Lehrbuch. Berlin, Heidelberg: Springer Berlin Heidelberg, 2016. DOI: 10.1007/978-3-662-49094-5.

[EM04] Magali Estribeau and Pierre Magnan. "Fast MTF measurement of CMOS imagers using ISO 12233 slanted-edge methodology". In: *Detectors and Associated Signal Processing*. Ed. by Jean-Pierre Chatard and Peter N. J. Dennis. Vol. 5251. Proceedings of SPIE Vol. 5251. Society of Photo-Optical Instrumentation Engineers (SPIE). Bellingham, WA: SPIE, 2004, pp. 243–252. DOI: 10.1117/12.513320.

[Emo+20] Julius Emons, Peter A. Fasching, Marius Wunderle, Felix Heindl, et al. "Assessment of the additional clinical potential of X-ray dark-field imaging for breast cancer in a preclinical setup". In: *Therapeutic Advances in Medical Oncology* 12 (2020), p. 1758835920957932. DOI: 10.1177/1758835920957932.

[Eva55] Robley D. Evans. *The Atomic Nucleus*. In collab. with Osmania University and Digital Library Of India. Tata McGraw Hill Publishing Company Limited., 1955. 1002 pp. URL: http://archive.org/details/atomicnucleus032805mbp (visited on 03/06/2025).

[Fre+10] Erik Fredenberg, Magnus Hemmendorff, Björn Cederström, Magnus Åslund, and Mats Danielsson. "Contrast-enhanced spectral mammography with a photon-counting detector". In: *Medical Physics* 37.5 (2010), pp. 2017–2029. ISSN: 2473-4209. DOI: 10.1118/1.3371689.

[Gra+20] J Graetz, A Balles, R Hanke, and S Zabler. "Review and experimental verification of x-ray dark-field signal interpretations with respect to quantitative isotropic and anisotropic dark-field computed tomography". In: *Physics in Medicine & Biology* 65.23 (Nov. 27, 2020), p. 235017. ISSN: 1361-6560. DOI: 10.1088/1361-6560/abb7c6.

[Gur+09] Tim Gureyev, Sheridan Mayo, Damian Myers, Ya Nesterets, et al. "Refracting Röntgen's rays: Propagation-based x-ray phase contrast for biomedical imaging". In: *Journal of Applied Physics* 105 (June 2009), pp. 102005–102005. DOI: 10.1063/1.3115402.

[HGD93] B. L. Henke, E. M. Gullikson, and J. C. Davis. "X-Ray Interactions: Photoabsorption, Scattering, Transmission, and Reflection at E = 50-30,000 eV, Z = 1-92". In: *Atomic Data and Nuclear Data Tables* 54.2 (1993), pp. 181–342. ISSN: 0092-640X. DOI: https://doi.org/10.1006/adnd.1993.1013.

[Hou73] G. N. Hounsfield. "Computerized transverse axial scanning (tomography): Part I. Description of system". In: *British Journal of Radiology* 46 (1973), pp. 1016–1022.

[Kal+90] W A Kalender, W Seissler, E Klotz, and P Vock. "Spiral volumetric CT with single-breath-hold technique, continuous transport, and continuous scanner rotation." In: *Radiology* 176.1 (1990). PMID: 2353088, pp. 181–183. DOI: 10.1148/radiology.176.1.2353088.

[Kho+19] Hamidreza Khodajou-Chokami, Seyed Abolfazl Hosseini, Mohammad Reza Ay, Ali Safarzadehamiri, et al. "A Novel Method for Measur-

ing the MTF of CT Scanners: A Phantom Study". In: *2019 IEEE International Symposium on Medical Measurements and Applications (MeMeA)*. 2019 IEEE International Symposium on Medical Measurements and Applications (MeMeA). Istanbul, Turkey: IEEE, June 2019, pp. 1–6. ISBN: 978-1-5386-8428-3. DOI: 10.1109/MeMeA.2019.8802129.

[KHP11] Rüdiger Kramme, Klaus-Peter Hoffmann, and Robert S. Pozos, eds. *Springer Handbook of Medical Technology*. Berlin, Heidelberg: Springer Berlin Heidelberg, 2011. ISBN: 978-3-540-74657-7 978-3-540-74658-4. DOI: 10.1007/978-3-540-74658-4.

[Kri12] Hanno Krieger. *Grundlagen der Strahlungsphysik und des Strahlenschutzes*. Wiesbaden: Vieweg+Teubner Verlag, 2012. DOI: 10.1007/978-3-8348-2238-3.

[KT07] Tom Kimpe and Tom Tuytschaever. "Increasing the Number of Gray Shades in Medical Display Systems—How Much is Enough?" In: *Journal of Digital Imaging* 20.4 (Dec. 2007), pp. 422–432. ISSN: 0897-1889, 1618-727X. DOI: 10.1007/s10278-006-1052-3.

[Lau48] E. Lau. "Beugungserscheinungen an Doppelrastern". In: *Annalen der Physik* 437.7-8 (1948), pp. 417–423. DOI: https://doi.org/10.1002/andp.19484370709.

[Lud20] Veronika Ludwig. "Development of image acquisition and alignment methods for X-ray dark-field and phase-contrast imaging". PhD Thesis. Erlangen, Germany: Erlangen Centre for Astroparticle Physics, Department of Physics, 2020.

[Mic+13] Thilo Michel, Jens Rieger, Gisela Anton, and et al. "On a dark-field signal generated by micrometer-sized calcifications in phase-contrast mammography". In: *Physics in Medicine and Biology* 58.8 (2013), pp. 2713–2732. DOI: 10.1088/0031-9155/58/8/2713.

[OM18] S. O'Grady and M. P. Morgan. "Microcalcifications in breast cancer: From pathophysiology to diagnosis and prognosis". In: *BBA - Reviews on Cancer* 1869.2 (2018), pp. 310–320. DOI: 10.1016/j.bbcan.2018.04.006.

[Pag06] David Paganin. *Coherent X-ray Optics*. Oxford, New York: Oxford University Press, 2006. ISBN: 9780198567288.

[PBS11] W. J. Palenstijn, K. J. Batenburg, and J. Sijbers. "Performance improvements for iterative electron tomography reconstruction using

graphics processing units (GPUs)". In: *Journal of Structural Biology* 176.2 (2011), pp. 250–253. DOI: 10.1016/j.jsb.2011.07.017.

[Pel+16] Georg Pelzer, Gisela Anton, Florian Horn, Jens Rieger, et al. "A beam hardening and dispersion correction for x-ray dark-field radiography". In: *Medical Physics* 43.6 (2016), pp. 2774–2779. ISSN: 2473-4209. DOI: 10.1118/1.4948671.

[Pfe+06] Franz Pfeiffer, Timm Weitkamp, Oliver Bunk, and Christian David. "Phase retrieval and differential phase-contrast imaging with low-brilliance X-ray sources". In: *Nature Physics* 2.4 (Apr. 2006), pp. 258–261. ISSN: 1745-2473, 1745-2481. DOI: 10.1038/nphys265.

[Rad17] Johann Radon. "Über die Bestimmung von Funktionen durch ihre Integralwerte längs gewisser Mannigfaltigkeiten". In: *Berichte der Sächsischen Akademie der Wissenschaften zu Leipzig, Mathematisch-Physikalische Klasse* 69 (1917), pp. 262–277.

[Rau+20] Thomas Rauch, Jens Rieger, Georg Pelzer, Florian Horn, et al. "Discrimination analysis of breast calcifications using x-ray dark-field radiography". In: *Medical Physics* 47.4 (2020), pp. 1813–1826. DOI: 10.1002/mp.14043.

[Rau22] Constantin Rauch. "Quality improvement measurements for grating-based X-ray phase-contrast imaging". Master's Thesis in Physics. Erlangen, Germany: Erlangen Centre for Astroparticle Physics, Department of Physics, Apr. 2022.

[Ray81] L. Rayleigh. "XXV. On copying diffraction-gratings, and on some phenomena connected therewith". In: *The London, Edinburgh, and Dublin Philosophical Magazine and Journal of Science* 11.67 (1881), pp. 196–205. DOI: 10.1080/14786448108626995.

[Rei91] Stephen E. Reichenbach. "Characterizing digital image acquisition devices". In: *Optical Engineering* 30.2 (1991), p. 170. ISSN: 00913286. DOI: 10.1117/12.55783.

[Rig+08] Luigi Rigon, Alberto Astolfo, Fulvia Arfelli, and Ralf-Hendrik Menk. "Generalized diffraction enhanced imaging: Application to tomography". In: *European Journal of Radiology* 68.3 (Dec. 1, 2008). Publisher: Elsevier, S3–S7. ISSN: 0720-048X, 1872-7727. DOI: 10.1016/j.ejrad.2008.04.026.

[Rit+14] André Ritter, Peter Bartl, Florian Bayer, Karl C. Gödel, et al. "Simulation framework for coherent and incoherent X-ray imaging and its

application in Talbot-Lau dark-field imaging". In: *Optics Express* 22.19 (Sept. 22, 2014), p. 23276. ISSN: 1094-4087. DOI: 10.1364/OE.22.023276.

[Rut13] Simon Rutishauser. "X-ray grating interferometry for imaging and metrology". PhD Thesis. Zurich, Switzerland: ETH Zurich, 2013. URL: https://www.research-collection.ethz.ch/bitstream/handle/20.500.11850/65481/eth-6750-02.pdf (visited on 03/25/2025).

[Sch20a] Markus Schneider. "Untersuchung des Absorptionsverhaltens eines Talbot-Lau-Interferometers und Analyse der Richtungsabhängigkeit des Dunkelfelds in Abhängigkeit der Korrelationslänge". Bachelor's Thesis in Physics. Erlangen, Germany: Erlangen Centre for Astroparticle Physics, Department of Physics, May 2020.

[Sch20b] Stephan Schreiner. "Design and characterization of a portable Talbot interferometer for imaging high energy density experiments". Master's Thesis in Physics. Erlangen, Germany: Erlangen Centre for Astroparticle Physics, Department of Physics, Nov. 2020.

[SKJ18] Wolfgang Schlegel, Christian P. Karger, and Oliver Jäkel, eds. *Medizinische Physik: Grundlagen – Bildgebung – Therapie – Technik*. Berlin, Heidelberg: Springer Berlin Heidelberg, 2018. DOI: 10.1007/978-3-662-54801-1.

[Sta] International Organization for Standardization. *ISO 12233:2024*. Accessed on: 03/20/2025. URL: https://www.iso.org/standard/88626.html.

[Tak+15] Tomomi Takenaga, Shigehiko Katsuragawa, Makoto Goto, Masahiro Hatemura, et al. "Modulation transfer function measurement of CT images by use of a circular edge method with a logistic curve-fitting technique". In: *Radiological Physics and Technology* 8.1 (Jan. 2015), pp. 53–59. ISSN: 1865-0333, 1865-0341. DOI: 10.1007/s12194-014-0286-x.

[Tal36] Henry Fox Talbot. "LXXVI. Facts relating to optical science. No. IV". In: *The London, Edinburgh, and Dublin Philosophical Magazine and Journal of Science* 9.56 (1836), pp. 401–407.

[TI13] Katsuyuki Taguchi and Jan S. Iwanczyk. "Vision 20/20: Single photon counting x-ray detectors in medical imaging". In: *Medical Physics* 40.10 (2013), p. 100901. DOI: 10.1118/1.4820371.

[Vie+22] Manuel Viermetz, Nikolai Gustschin, Clemens Schmid, Jakob Haeusele, et al. “Dark-field computed tomography reaches the human scale”. In: *Proceedings of the National Academy of Sciences* 119.8 (Feb. 22, 2022), e2118799119. ISSN: 0027-8424, 1091-6490. DOI: 10.1073/pnas.2118799119.

[Wei+05] Timm Weitkamp, Ana Diaz, Christian David, Franz Pfeiffer, et al. “X-ray phase imaging with a grating interferometer”. In: *Optics Express* 13.16 (Aug. 8, 2005), p. 6296. ISSN: 1094-4087. DOI: 10.1364/OPEX.13.006296.

[Wig+21] Kristina T. Wigati, Nicholas W. Marshall, Kim Lemmens, Joke Binst, et al. “On the relevance of modulation transfer function measurements in digital mammography quality control”. In: *Journal of Medical Imaging* 8.2 (Mar. 2021), p. 023505. ISSN: 2329-4302. DOI: 10.1117/1.JMI.8.2.023505.

[Wol16] Andreas Wolf. “Untersuchungen zu einer iterativen CT-Rekonstruktion in der gitterbasierten Röntgenbildgebung”. Master’s Thesis in Physics. Erlangen, Germany: Erlangen Centre for Astroparticle Physics, Department of Physics, Apr. 2016.

[Wor24] World Health Organization. *Breast cancer*. Accessed: 2025-04-21. 2024. URL: https://www.who.int/news-room/fact-sheets/detail/breast-cancer.

[WW86] H. Q. Woodard and D. R. White. “The composition of body tissues”. In: *The British Journal of Radiology* 59.708 (Dec. 1986), pp. 1209–1218. ISSN: 0007-1285. DOI: 10.1259/0007-1285-59-708-1209.

[YWL15] Aimin Yan, Xizeng Wu, and Hong Liu. “A general theory of interference fringes in x-ray phase grating imaging”. In: *Medical Physics* 42.6 (2015), pp. 3036–3047. ISSN: 2473-4209. DOI: 10.1118/1.4921124.

Acknowledgements

Last but not least, I would like to thank all those who supported me during the course of this thesis. My sincere thanks go to:

- Prof. Dr. Stefan Funk for providing the topic, for his helpful feedback during the weekly meetings, and for his enthusiasm and interest in new results, which consistently motivated me throughout the work.
- Prof. Dr. Gisela Anton for her valuable suggestions and, in particular, for the inspiring in-depth discussions after the weekly meetings, as well as for the idea of implementing quality maps.
- My supervisors and colleagues from the Phase-Contrast Imaging Research Group – Dr. Veronika Ludwig, Dr. Stephan Schreiner, Constantin Rauch, and Markus Schneider – who were always approachable, supportive, and full of fresh ideas and perspectives.
- The Dosimetry Research Group – Florian Beißer, Leonie Ullmann, and Nico Kiessl – for the enjoyable atmosphere at the institute and especially during our lunch breaks.
- My mother Heike Nadler and My father Helmut Fritsch, who supported and motivated me not only during my Master's studies but throughout my entire academic journey.

Declaration of Authorship

I hereby declare that I, Luca Fritsch (student ID 22530964), have written this thesis independently and without using any sources or aids other than those stated. All passages taken from published or unpublished works have been clearly marked as such. This thesis has not been submitted to any other examination authority and has not yet been used as a thesis.

Place, Date

Signature